DEVELOPMENT OF METAL OXIDE NANOSTRUCTURES INCORPORATED WITH CARBON MATRIX FOR ELECTROCHEMICAL APPLICATIONS

NUMAN ARSHID

FACULTY OF SCIENCE
UNIVERSITY OF MALAYA
KUALA LUMPUR

2018

DEVELOPMENT OF METAL OXIDE NANOSTRUCTURES INCORPORATED WITH CARBON MATRIX FOR ELECTROCHEMICAL APPLICATIONS

NUMAN ARSHID

THESIS SUBMITTED IN FULFILMENT OF THE
REQUIREMENTS FOR THE DEGREE OF
DOCTOR OF PHILOSOPHY

DEPARTMENT OF PHYSICS
FACULTY OF SCIENCE
UNIVERSITY OF MALAYA
KUALA LUMPUR

2018

UNIVERSITY OF MALAYA

ORIGINAL LITERARY WORK DECLARATION

Name of Candidate: **Numan Arshid**

Registration/Matric No: **SHC 140087**

Name of Degree: **Doctor of Philosophy**

Title of Thesis: **Development of Metal Oxide Nanostructures Incorporated with Carbon Matrix for Electrochemical Applications**

Field of Study: **Experimental Physics**

I do solemnly and sincerely declare that:

(1) I am the sole author/writer of this Work;
(2) This Work is original;
(3) Any use of any work in which copyright exists was done by way of fair dealing and for permitted purposes and any excerpt or extract from, or reference to or reproduction of any copyright work has been disclosed expressly and sufficiently and the title of the Work and its authorship have been acknowledged in this Work;
(4) I do not have any actual knowledge nor do I ought reasonably to know that the making of this work constitutes an infringement of any copyright work;
(5) I hereby assign all and every rights in the copyright to this Work to the University of Malaya ("UM"), who henceforth shall be owner of the copyright in this Work and that any reproduction or use in any form or by any means whatsoever is prohibited without the written consent of UM having been first had and obtained;
(6) I am fully aware that if in the course of making this Work I have infringed any copyright whether intentionally or otherwise, I may be subject to legal action or any other action as may be determined by UM.

Candidate's Signature Date:

Subscribed and solemnly declared before,

Witness's Signature Date:

Name:

Designation:

DEVELOPMENT OF METAL OXIDE NANOSTRUCTURES INCORPORATED WITH CARBON MATRIX FOR ELECTROCHEMICAL APPLICATIONS

ABSTRACT

Over the last few decades, nanomaterials have found prodigious potential in various applications of different research fields. Although the metal oxide frame work is not a new class of nanomaterials yet its potential is not explored extensively, especially for electrochemical applications. One of the most significant research motivations for metal oxide frame works come from their tunable morphology, porosity, rigidity/flexibility, variety and facile design which make them capable of using in variety of advanced energy conversion, energy storage and electrochemical sensing devices. However, unsupported metal oxide nanostructures suffers from particle aggregations which lead to decrease their electrochemical surface area. In this work, one step hydrothermal route was used to develop binary nanocomposite of metal oxide (Co_3O_4) and carbonaceous matrix such as graphene, multiwall carbon nanotubes (MCNTs). The first system, binary composite of reduced graphene intercalated with cobalt oxide (Co_3O_4) nanocubes was synthesized and the contents of Co_3O_4 precursor were optimized with respect to fixed amount of reduced graphene oxide (rGO). The rGO−Co_3O_4 nanocubes was used for supercapacitor application. It was found that with 0.5 mmol of cobalt precursor (A2) gave the highest specific capacity (125 Cg^{-1}) in three electrode cell system. Same nanocomposite was used to fabricate rGO−Co_3O_4 nanocubes//activated carbon hybrid supercapacitor and the maximum energy and power density was found to be 7.75 $Wh.k^{-1}$ and 996.42 $W.kg^{-1}$, respectively. In second system, composite of rGO−Co_3O_4 nanograins was optimized by varying the contents of rGO with respect to the fixed concentration of Co_3O_4 precursor. The performance of rGO−Co_3O_4 nanograins was evaluated for electrochemical sensing of dopamine. The nanocomposite rGO−Co_3O_4 (B3) with 9.1 wt. % of rGO was optimized on the basis of oxidation current of dopamine. The B3 modified glassy carbon electrode gave 0.277 μL (S/N=3) limit of detection for dopamine in the linear range of 1−30 μL. The performance of B3 modified GCE was also satisfactory in real time urine sample and in the presence of physiological interfering analytes. In the last system, Co_3O_4 nanocubes were fabricated with MWCNT and the contents of MWCNT with respect to the fixed amount of cobalt precursor were optimized. The MWCNT−Co_3O_4 nanocube was used for supercapacitor and electrochemical sensing of dopamine application. In both applications, MWCNT−Co_3O_4 nanocubes (C4) with 16 wt. % of MWCNT demonstrated excellent electrochemical performance compared to its counterparts. The maximum specific capacity was 142 Cg^{-1} using three electrode cell system. The highest energy density was found to be 19.28 $Wh.kg^{-1}$ at power density of 309.85 $W.kg^{-1}$. The optimized nanocomposite (C4) also showed excellent electrochemical performance for dopamine detection. The limit of detection is found to be 0.176 μL in the linear range of 1−30 μL. However, MWCNT−Co_3O_4 nanocube showed poor selectivity towards dopamine detection. Overall, MWCNT−Co_3O_4 nanocubes gave better performance for hybrid supercapacitor compared to rGO−Co_3O_4 nanocubes in terms of specific capacity and energy density. However, rGO−Co_3O_4 nanograins endowed good sensing capability for dopamine detection in terms of selectivity compared to MWCNT−Co_3O_4 nanocubes. This work embark the frontiers of carbonaceous materials for electrochemical applications.

Keywords: supercapacitor, electrochemcial sensors, cobalt oxide, graphene oxide, multiwall carbon nanotubes

PENGHASILAN LOGAM OKSIDA STRUKTUR NANO CAMPURAN DENGAN MATRIKS KARBON UNTUK APLIKASI ELEKTROKIMIA

ABSTRAK

Sejak beberapa dekad yang lalu, bahan nano telah mempunyai potensi yang besar dalam pelbagai aplikasi dan bidang penyelidikan yang berbeza. Walaupun kerangka logam oksida bukan bahan nano yang baharu tetapi potensinya belum diterokai secara meluas, terutamanya untuk aplikasi elektrokimia. Salah satu motivasi penyelidikan kerangka logam oksida yang paling penting datang dari morfologi, keliangan, ketegaran / fleksibiliti, kepelbagaian dan reka bentuk mudah yang menbolehkan mereka digunakan dalam pelbagai penukaran tenaga maju, penyimpanan tenaga dan peranti penderiaan elektrokimia. Walau bagaimanapun, struktur nano logam oksida tanpa sokongan mengalami pengagregatan zarah yang membawa kepada pengurangan luas permukaan elektrokimia mereka. Dalam kerja ini, satu langkah laluan hidrothermal telah digunakan untuk membina komposit nano binari logam oksida (Co_3O_4) dan matriks karbon seperti grafin, tiub nano karbon berbilang dinding. Dalam sistem pertama, komposit binari pengurangan grafin yang diinterkalasi dengan kiub nano kobalt oksida (kiub nano rGO−Co_3O_4) telah disintesis dan kandungan prekursor Co_3O_4 dioptimumkan selaras dengan jumlah tetap rGO. Kiub nano rGO−Co_3O_4 telah digunakan untuk aplikasi superkapasitor. Didapati bahawa, 0.5 mmol prekursor kobalt (A2) memberikan kapasiti khusus tertinggi (123 Cg^{-1}) dalam sistem tiga sel elektrod. Komposit nano yang sama telah digunakan untuk membina kiub nano/ karbon aktif rGO−Co_3O_4. Ketumpatan tenaga dan ketumpatan kuasa maksimum yang didapati masing-masing adalah 7.71 $Wh.kg^{-1}$ dan 996.42 $W.kg^{-1}$. Dalam sistem kedua, komposit nano rGO−Co_3O_4 butir nano telah dioptimumkan dengan mempelbagaikan kandungan rGO berkenaan dengan kepekatan tetap prekursor Co_3O_4. Prestasi butir nano rGO−Co_3O_4 telah dinilai untuk penderiaan elektrokimia dopamin. Komposit nano rGO−Co_3O_4 (B3) dengan 9.1 wt. % telah dioptimumkan berdasarkan pengoksidaan arus dopamin. Elektrod karbon kaca (GCE) yang telah diubahsuai (B3) menunjukkan 0.277 μL (S/N=3) had pengesanan dalam julat linear 1−30 μL. Prestasi GCE diubahsuai dengan B3 juga memuaskan dalam sampel air kencing yang sebenar dan dengan kehadiran fisiologi gangguan analit. Dalam system yang terakhir, Co_3O_4 kiub nano digabungkan dengan tiub nano karbon dinding berbilang (MWCNT) dan kandungan MWCNT telah dioptimumkan. Kiub nano MWCNT−Co_3O_4 telah digunakan di dalam aplikasi superkapasitor dan penderiaan elektrokimia dopamin. Di dalam kedua-dua aplikasi, kiub nano MWCNT−Co_3O_4 (C4) dengan 16 wt. % of MWCNT telah menunjukkan prestasi elektrokimia yang cemerlang. Keupayaan khusus yang maksimum adalah a 142 Cg^{-1} menggunakan sistem tiga sel electrod. Ketumpatan tenga yang paling tinggi adalah 19.28 Wh.kg^{-1} pada ketumpatan kuasa 309.85 W.kg^{-1}. Komposit nano yang optimum (C3) telah menunjukkan prestasi elektrokimia yang cemerlang untuk pengesanan dopamin. Had pengesanan adalah 0. 176 μL pada julat linear 1−30 μL. Walau bagaimanapun, kiub nano MWCNT−Co_3O_4 menunjukkan selektif lemah terhadap pengesanan dopamin. Pada keseluruhan, kiub nano MWCNT−Co_3O_4 telah menunjukkan prestasi yang baik untuk superkapasitor hibrid betbanding dengan kiub nano rGO−Co_3O_4 dari segi keupayaan tertentu dan ketumpatan tenaga. Walau bagaimanapun, rGO−Co_3O_4 butiran nano memberi keupayaan penderiaan yang baik untuk pengesanan dopamin dari segi selektif dibandingkan dengan kiub nano MWCNT−Co_3O_4. Kejian ini memulakan saluran baru bagi bahan-bahan karbon untuk aplikasi elektrokimia.

Kata kunci: superkapasitor, Pengesan Elektrokimia, kobalt oksida, grafin oksida, karbon tiub nano dinding berbilang

ACKNOWLEDGEMENTS

"All glory be to Almighty Allah, Who is the lord of all mankind, jinn and all that exist, the most merciful and the most beneficent." I thank to Allah (Subhanahu Wa Taalaa) for the strength and His blessing for granting me the capability to complete this thesis. I humbly offer salutations upon **Prophet Muhammad (peace be upon him)** and all Prophets, the source of guidance and knowledge to all mankind. Firstly, I would like to express my sincere gratitude to my advisors Prof. Dr. Ramesh Subramaniam and Associate Prof. Dr. Ramesh Kasi for the continuous support of my PhD study and related research, for their patience with me, their critical review which allowed me to enhance the quality of my research writings, motivation and immense knowledge. I could not have imagined having better advisors and mentors for my PhD study. I likewise express my earnest gratitude to Dr. Navaneethan, Mr. Shahid Mehmood and Miss Fatin Saiha for their intellectual help during my research and provided me support in preparation of various manuscripts for publications. They are greatly acknowledged for comments on my reports, dissertation and manuscripts. I would like to extend my gratitude to Dr. Yugal, Dr. Sohail Ahmad, Dr. Siamik, Syed Tawab Shah, Dr. Shahabuddin, Dr. Ramesh Kumar, Prof. Rahman Wali Khattak and Engineer Nazir Muhammad for their valuable scientific discussions, advices and always willingly to helping me out with any scientific problem. I would especially like to thank my lab fellows/colleagues/seniors members, Center for Ionics and department of Physics for providing me space and equipped me with latest technological instruments. Finally, a deepest gratitude goes my parents and my brothers for all of the sacrifices that you've made on my behalf. Your prayer for me was what sustained me this far. **I would like to dedicate this work to my beloved mother (Ammi Jan),** who's prayers always back me at every difficult situation.

NUMAN ARSHID

January, 2018

TABLE OF CONTENTS

LIST OF FIGURES

LIST OF TABLES

LIST OF SYMBOLS AND ABBREVIATIONS

AA	Ascorbic acid
AC	Activated carbon
CV	Cyclic voltammetry
CVC	Chemical vapor condensation
DAQ	Dopamine quinone
DPV	Differential pulse voltammetry
EDL	Electric double-layer
EDLC	Electric double layer capacitors
EDX	Energy dispersive X-ray
EIS	Electrochemical impedance spectroscopy
ESR	Equivalent series resistance
FESEM	Field emission scattering electron microscopy
FET	Field effect transistors
GCD	Galvanostatic charge discharge
GCE	Glassy carbon electrode
GO	Graphene oxide
HIV	Human immunodeficiency virus
HRTEM	High resolution transmission electron microscopy
IHP	Inner Helmholtz plane
ISI	Institute of Scientific Information
IUPAC	International union of pure and applied chemistry

LOD	Limit of detection
LOQ	Limit of quantification
MOF	Metal oxide frame
MRI	Magnetic resonance imaging
OHP	Outer Helmholtz plane
PB	Phosphate buffer
PLA	Pulse laser ablation
QCD	Quantum carbon dots
SAED	Selected area electron diffraction
SD	Standard deviation
SERRS	Surface enhanced resonance Raman scattering
SWV	Square wave voltammetry
UA	Uric acid
UM	University of Malaya
XPS	X-ray photoelectron spectroscopy
XRD	X-ray diffractometer

CHAPTER 1: INTRODUCTION

1.1 Background of Research

Nanotechnology is arguably the most revolutionary field of the 20th century, as it exposed new frontiers of technology. The application of nanomaterials have dominated almost all of the field of applications. Transition metal oxide nanostructure is a unique class of nanomaterials which emerged on the horizon of nanotechnology as a shining star. Due to extraordinary physical, chemical, optical and magnetic properties of metal oxide nanostructures, they have a wide range of applications in industry, pharmacy and optoelectronics. In the past few decades, metal oxide nano-frameworks are extensively employed in electrochemical devices to store and convert energy. Recent reports unveiled their great potentials for energy storage (supercapacitors, batteries and fuel cells), energy conversion (solar cells) and electrochemical sensing applications.

Beside metal oxide nanostructures, carbon is naturally occurring element which bears a number of auspicious characteristic properties that make it an ideal building block in various electrochemical applications. Carbonaceous materials are stable over a wide temperature range (sublimating at about 3900 K under atmospheric conditions and a melting point of 4800 K, with low density compared to metals and alloys, which make them suitable for compact and lightweight applications (Savvatimskiy, 2005)). The latest addition in the family of carbonaceous materials is graphene. Graphene is a 2D hexagonal lattice structured material which is discovered a decade ago and it sparked substantial interest in the scientific community owing to its outstanding properties (Shahid *et al.*, 2014). Currently, graphene is the most studied material in the scientific community especially by electrochemist for electrochemical applications. According to the database of Institute of Scientific Information (ISI), the research articles based on graphene are increasing exponentially since its discovery (shown in Figure 1.1). Also the number of citations (per year) of graphene based research articles are increased by 9 fold with reference to its year of discovery. These facts reveal the applicability and great potential of graphene in various fields.

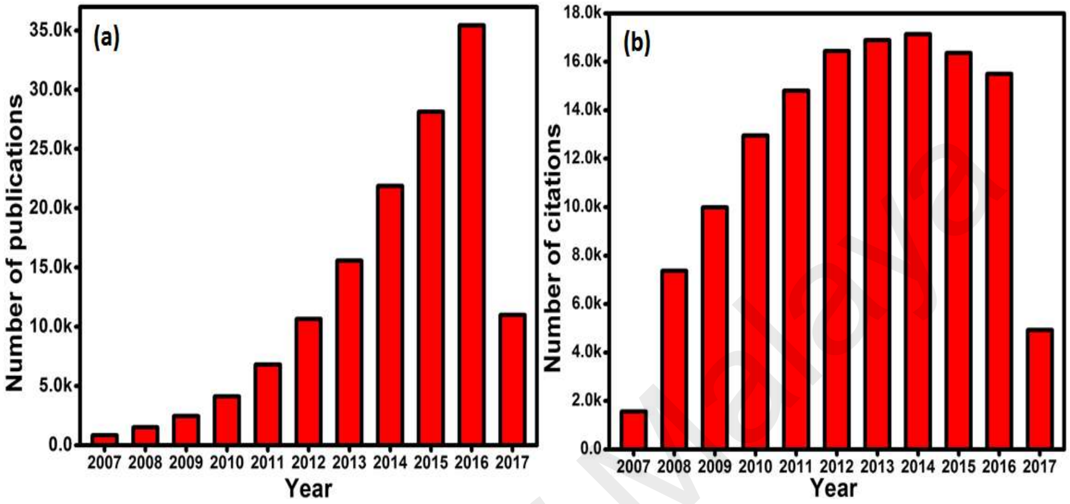

Figure 1.1: (a) Number of research articles per year on graphene and (b) Number of citations per year on graphene. The data was collected from the data base of the ISI using graphene as a keyword that appeared in topic.

Now-a-days, graphene has been flaunted as superior material for energy storage applications compared to classical electrode materials such as metal oxide, graphite, or glassy carbon. A single sheet of graphene is sufficient in size to cover an entire American football field would weigh just a fraction of a gram. The huge surface area associated with the small amount of graphene can be squeezed inside an electrochemical device, enabling the design of new energy-storage devices with the ability to store massive amounts of charge (El-Kady *et al.*, 2016). On the other hand, CNTs are the graphene sheets which are rolled in cylindrical form. They offer exceptional mechanical, thermal and electronic properties with hollow structure.

The incorporation of carbon matrix (graphene and CNT) with other materials such as noble metals, metal oxides and conducting polymers can produce synergistic effect resulting high electrochemical performance nanocomposite. Due to this reason, the development, characterization of carbon matrix based nanocomposite for electrochemical applications continues to be the focus of research in electrochemistry. The development and characterization of carbon matrix supported noble metal and transition metal oxide nanoparticles continues to be the focus of research in electrochemistry. The scientific interest and rational keenness of researchers is to explore new frontiers of applications for the carbon matrix supported metal oxides by understanding the mechanism of the nanocomposites behavior during redox reactions. Recent reports on carbon matrix supported metal oxides unveiled their great potential in electrocatalysis, electrochemical sensing, photocatalaysis, solar cells, adsorption and energy storage applications (Chabot *et al.*, 2014; Choi *et al.*, 2010; Roy-Mayhew *et al.*, 2014). In the nanocomposite of carbon matrix and metal oxide nanoparticles, carbon matrix provide highly conductive platform for metal oxide nanoparticles (which usually bear higher band gap) facilitating fast charge transfer kinetics. Moreover, the electronegative functional groups on the surface of carbon matrix serve as nucleation cites for the growth of metal oxide nanoparticles during synthesis. This helps in uniform growth of metal oxide nanoparticles over carbon matrix, which lead to high electrochemical surface area. On the other hand, metal oxides nanoparticles with a large surface area to volume ratio have excellent biocompatibitly, outstanding electro-catalytic activities and rapid electron transfer kinetics.

1.2 Hypothesis

The motivation behind this research work was based on the following hypothesis:

a) Graphene oxide composed of sp^2 hybridization of carbon atoms, offer extraordinary electrochemical surface area (2630 m^2g^{-1}), ballistic conductivity (106 S cm^{-1}), unique electronic configuration, and wide electrochemical window. These inherent properties of graphene make it suitable for electrochemical applications. The highly electronegative oxygen containing functional groups at the basal plane of graphene can play major role during an electrochemical sensing event by interacting with target molecule and effectively catalyze the redox reaction. Moreover, the structural defects produced chemically are really helpful for electrochemical sensing applications.

The extraordinary high electrochemical surface area of graphene is one of the most important feature which attracted researchers to exploit it for energy storage applications. A single layer of graphene can give intrinsic capacitance of ~ 21 μF cm^{-2} which is equal to the maximum capacitance of an electric double-layer (EDL) capacitance among all carbon based materials (Xia *et al.*, 2009). Therefore, in principle graphene based supercapacitor can achieve an EDL capacitance of ~ 550 Fg^{-1}, if the whole surface of graphene can be fully utilized. In addition to this, application of graphene in the electrode of energy storage device can motivate to introduce a variety of new features such as highly flexible and even foldable energy storage devices, transparent supercapacitors, batteries and high energy density with rapid charging devices.

b) CNTs are one of the allotrope of graphite demonstrate excellent conductivity (106 Sm^{-1} for single walled carbon nanotubes (SWCNTs) and 105 Sm^{-1} for multiwall carbon nanotubes (MWCNTs) with promising mechanical strength (60 GPa) (Ando *et al.*, 1999; Yu *et al.*, 2000). These features makes them suitable for energy storage applications.

One of the unique inherent property of CNTs is large edge plane to basal plan ratio. These edge-like graphite sites are highly active for redox reactions which is favorable feature for electrochemical sensors (Jacobs *et al.*, 2010). Moreover, CNTs also facilitate fast charge transfer kinematics compared to traditional carbon electrodes, which is extremely important for electrochemical sensors. Hence, CNTs can perform well when used for as for electrochemical sensors.

c) Metal oxides with a large surface area to volume ratio have excellent biocompatibility, outstanding electrocatalytic activities and rapid electron transfer kinetics, which make them suitable for electrochemical sensing, heterogeneous catalysts and energy storage devices. Moreover, their low-cost, facile synthesis, durability and diverse morphologies are the motivating features to commercialize them for energy storage and electrochemical sensing applications.

Among the various transition metal oxides, cobalt oxide (Co_3O_4) stand prominent owing to its simple preparation method, excellent chemical durability, promising ratio of to the total surface atoms and diverse morphologies (Jafarian *et al.*, 2003). It is a p-type semiconductor material which has a cubic spinel structure with both direct and indirect band gaps of 2.10 eV and 1.60 eV, respectively (Koumoto *et al.*, 1981). Co_3O_4 is a battery grade material which is expected to have good energy storage capability. At the same time its low band gap, diverse polar sites in Co_3O_4 crystal, surface to volume ratio and excellent catalytic activity makes it suitable candidate for electrochemical sensing applications.

d) Unaided Co_3O_4 nanoparticles suffer from high particle aggregations which lead to low electrochemical surface area. In addition, their conductivity is lower also poor which renders sluggish charge transfer. However, the combination of Co_3O_4 nanoparticles with carbon matrix can produce synergistic effect, where Co_3O_4 nanoparticles contribute in the catalytic activity, while CNTs and graphene help in boosting the charge transfer kinetics. Additionally, the functional groups on the basal plane of graphene or CNTs can provide nucleation cites for the uniform growth Co_3O_4 nanoparticles. This can significantly eliminate particle aggregations.

1.3 Aims and Objectives of Research

As mentioned earlier, the high electrochemical surface area, porosity, ballistic conductivity, excellent thermal and mechanical stability make graphene and CNTs are promising candidates for energy storage applications. The 2D honey comb lattice structure, oxygen containing functional groups and heterogeneous electronic transfer of graphene can play a vital role in electrochemical sensing applications. The edge graphite sites in CNTs can serve as active sites in electrochemical sensing applications. Also it is well established that making composite of carbon matrix with metal oxide nanostructures can result a material with enhance electrochemical properties. The supported metal oxide nanostructures can perform redox reactions for energy storage or recognition of physiological molecule while highly carbon matrix can serve as highly conductive platform that can boost charge transportation. Moreover, the oxygen containing moieties can serve as nucleation site for the uniform growth of metal oxide nanostructures.

The challenging task in this research was to design a facile, economical, short and low temperature synthesis route for the preparation of metal oxides and binary composite of metal oxide nanostructures supported on carbon matrix. Additionally, the prepared nanocomposite should be versatile that can have good energy storage ability as well as excellent sensing capability with comparatively low detection limit.

In order to achieve the aforementioned targets, following objectives were supposed to design and completed:

1) To functionalize graphene and CNTs.

2) To optimize the parameters for the synthesis of metal oxide nanostructures by using one pot hydrothermal route.

3) To synthesis binary nanocomposite of metal oxide nanoparticles supported on graphene and CNT.

4) To characterize the as synthesized binary nanocomposites.

5) To investigate the performance of the synthesized binary nanocomposite for supercapacitor application and electrochemical sensing applications.

Graphene is usually synthesized by Hummer's method or modified Hummer's method which involves long and complicated reaction times. However, in this research simplified Hummer's method was used, which is facile, comparatively short in duration and uses room temperature for the synthesis of graphene.

Pristine CNTs were commercially bought and then functionalized with oxygen containing functional groups by acid treatment. Functionalization was done to increase the conductivity, porosity, hydrophilicity and removal of amorphous carbon as well as metal residue.

Hydrothermal route was preferred to synthesis the metal oxide nanostructure as it allows to fabricate diverse morphologies and particle sizes of metal oxides by tuning the synthetic para meters such as; pH, reaction time, temperature, precursor contents and solvent system used.

In order to synthesize binary nanocomposite, a single step of hydrothermal reaction was used. The metal oxide nanoparticles were successfully incorporated with graphene and CNTs, while their particle size and morphology was kept constant. Both types of nanocomposites i.e. graphene supported metal oxide nanoparticles and CNTs supported metal oxide nanoparticles were synthesized. The synthesized nanocomposites were fully characterized in order to investigate their crystallinity, composition, morphology and binding energies.

In order to investigate the electrochemical performance of the prepared nanocomposites, three electrode and two electrode cell system were used. The optimization of nanocomposites was done on the basis results obtained by three electrode cell system while performance parameters like specific capacity, energy density and power density were obtained using two electrode cell system (hybrid electrode assembly). The electrochemical performance of the synthesized nanocomposites was also evaluated for electrochemical sensing of physiological analytes. In this research dopamine (DA) was chosen as physiological analyte as it is highly electroactive electrochemical sensing techniques.

1.4 Outline of Thesis

This thesis consists of five chapters. Chapter one is about the introduction of the research, background, motivation and hypothesis of this work and research objectives. Chapter two presents the detailed literature survey on carbonaceous materials, metal oxide nanoparticles, the composites of cobalt oxide with graphene and carbon nanotubes and their electrochemical applications as well as background of supercapacitors and electrochemical sensors. Chapter three elaborates the detailed methods for the synthesis characterization and application study of the materials. In chapter four, the results are discussed comprehensively while in chapter five conclusions of the thesis and the future work are provided.

CHAPTER 2: LITRATURE REVIEW

2.1 Architecture of Literature Review

This chapter gives an insight to the carbonaceous materials and detailed understanding of their chemical structure. The types of carbon based materials, especially CNTs and graphene are explained. The synthesis procedures and physiochemical properties of carbonaceous materials which play significant role in electrochemical applications are also discussed. A comprehensive literature survey on the synthesize techniques for the preparation of metal oxide nanostructures and their characteristic properties are presented. In addition to this, the background, complete understanding of working principle and the featured advantages of supercapacitors as well electrochemical sensors are explained.

This chapter is broadly subdivided into three parts. In first part carbonaceous materials their types and applications are explained in detail. In the family of carbon based materials, graphene and CNTs are the materials which have inherent features due to their structure and physiochemical properties. Therefore, the synthesis of graphene oxide its chemical composition at molecular level is explained which play vital role in energy storage and electrochemical sensing applications. In the last section of first part, the methods to transform graphene oxide in reduced graphene oxide and their structural differences are explained. The second part of this chapter is about metal oxides. The complete literature survey on the synthesis of metal oxide and their physiochemical properties is presented in this part. The last part of the chapter describes the background, understanding of working principle, applications and advantages of supercapacitors as well as electrochemical sensors.

2.2 Carbonaceous Materials

Carbon is an element which is abundant in nature and bears very important position in the periodic table. It possesses some unique intrinsic properties which makes it a basic building block element in various operating environment. The inherent inert structure, excellent stability over the wide temperature window (melting point at 4800 K while sublimation at 3900 K at standard atmospheric conditions), low mass to volume ratio and anti-corrosive nature against various reagents makes it suitable for light weight and compact applications (Savvatimskiy, 2005).

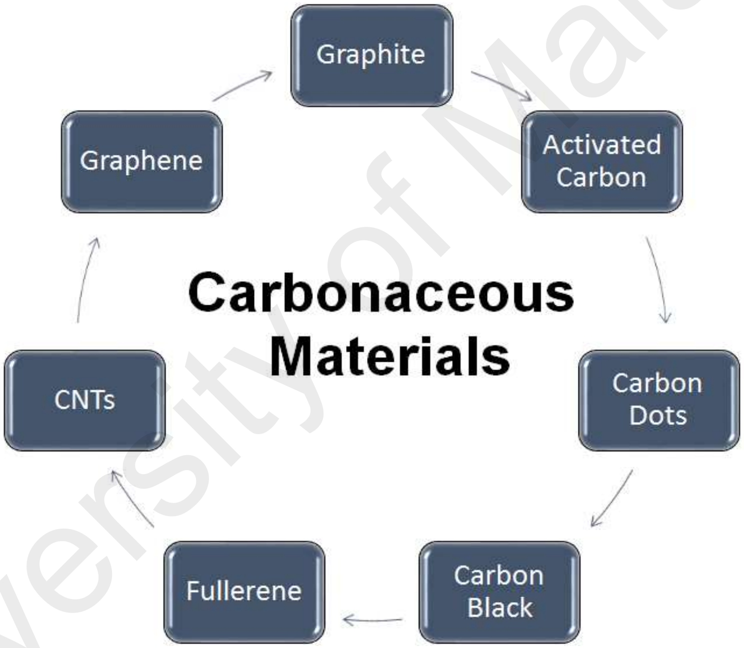

Figure 2.1: Some of the carbonaceous materials used for electrochemical applications.

The facile processing, economical and abundance in nature are the welcoming features of carbon for the preparation and commercialization of carbonaceous materials for numerous applications. The carbonaceous materials are usually graphitic crystallite structures at molecular level. One is basal plane composed of two dimensional *sp*^{2}-hyberdized carbon atoms while other is edge plane having defective graphitic lines of carbon atoms. The basal plane of carbonaceous material offer wide surface area while edge plane provides defect sites which are highly favorable for catalytic applications (Smith, 1983). In addition, carbonaceous materials offer more electrochemical surface area due to high porous structure or rough morphology, higher conductivity and excellent thermal as well as mechanical stability that makes it ideal candidate for electrochemical applications (Kouhnavard *et al.*, 2015; Wang *et al.*, 2012). Recent progress in the development of carbonaceous materials unveiled their great potential in electrochemical application involving, catalysis, energy conversion, and storage (Meregalli *et al.*, 2001; Zhang *et al.*, 2009). Some of important carbonaceous materials used for electrochemical applications are given below.

2.2.1 Natural Graphite

Graphite is a crystalline form of carbon which naturally occurs in the metamorphic and igneous rocks. It is composed of planer structure graphene layers stacked parallel to each other. The inter layer distance between the adjacent layers of graphene is ~ 0.335 nm which are bonded together by van der Waals forces. Figure 2 illustrates the stacked graphene layers in graphite. The hexagonal arrangement of the atoms in graphite structure strengthens its properties such as mechanical stability, corrosion, temperature and oxidation resistant. Additionally, the delocalization of π bonding in hexagonal layers of graphite offers excellent conductivity. Since it has low neutron and X-ray absorption so it is widely used in nuclear and radioactive applications.

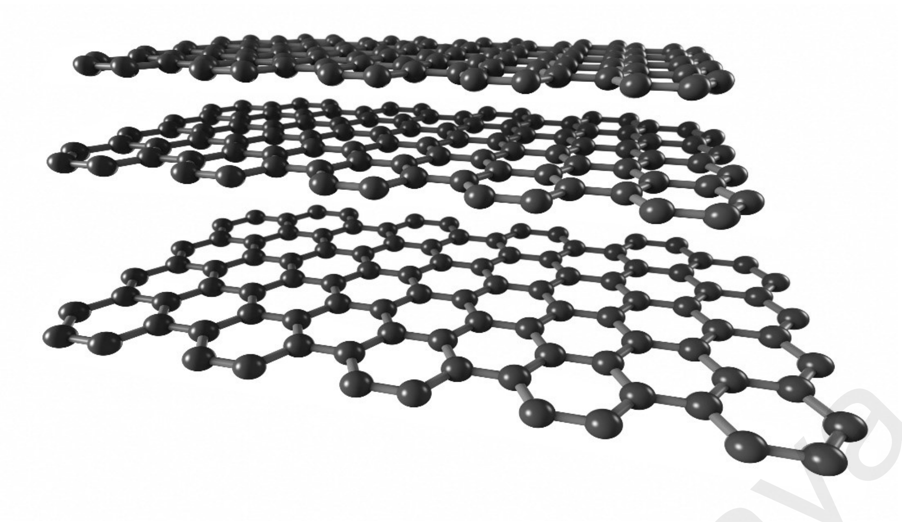

Figure 2.2: Stacked graphene sheets in graphite.

2.2.2 Activated Carbon

Activated carbon (also known activated charcoal) is a carbon material that has very small pores (in nm range) which elevate its surface area. Approximately one gram of activated carbon (AC) has a surface area of 32,000 ft^2 (Dillon *et al.*, 1989). The high mass to volume ratio with extraordinary electrochemical surface area are the promising features due to which it is extensively investigated in adsorption and electrochemical applications (Paul, 2009). Carbon power is generally extracted from natural sources such as wood, nut shells, peat, coconut and coal and then activated physically or chemically. In physical activation, the precursor of carbon is heated at elevated temperatures (ranging from 700 to 1200 °C) in the presence of activating/oxidizing gases like CO_2, air, and steam. However, chemical activation of carbon involves chemical reaction with potassium hydroxide (KOH), sodium hydroxide (NaOH), phosphoric acid (H_3PO_4) and zinc chloride ($ZnCl_2$) (Zhang & Zhao, 2009). The activation of carbon significantly improve its surface area (up to 300 m^{2}g^{-1}) and porosity (microspores form 2 to 50 nm and macropores up to 450 nm) depending upon the activation route and carbon precursor used (Raymundo-Pinero *et al.*, 2006). AC have wide range of applications in medicine, agriculture, analytical chemistry applications, liquid and gas purification and energy storage applications. From the past few decades, the potential of AC is being investigated for energy storage applications.

2.2.3 Quantum Carbon Dots

Quantum carbon dots (QCDs) are the recent addition in the family of carbonaceous material which were discovered a decade ago accidently by Xu et. al. during the purification of CNTs (Xu *et al.*, 2004). Like quantum dots, QCDs are the carbon nanoparticles with dimension less than 10 nm having excellent properties such as high stability and conductivity, low toxicity, good biocompatibility, environment friendliness, facile synthesis techniques and good optical properties (Chan *et al.*, 2002). Due to the surface passivation, QCDs possess unique optical tunable optical properties that are being investigated extensively in field of optoelectronics, bio imaging catalysis and sensing (Lim *et al.*, 2015).

2.2.4 Carbon Black

Carbon black is a polycrystalline carbon that is usually prepared by incomplete heavy combustion of petroleum products like coal tar, cracking tar, fluid catalytic cracking tar and vegetables. Carbon black have lot of subtypes named as acetylene black, Ketjen Black, Black Pearl, or Vulcan XC-72 which are used for various applications in the fields of food industry, electronics, coloring, coatings, electrochemical devices and catalysis (Sanders *et al.*, 2011). These materials have different properties such as surface area, conductivity, porosity and surface functional groups. Therefore their applications also depend upon their properties.

The Vulcan XC-72 and acetylene black are the two carbon black materials which are widely investigated in electrochemical devices for catalysis and energy storage applications. Vulcan XC-72 is extensively exploited as catalysts support for fuel cell application due to its wide specific surface area of 250 $m^2.g^{-1}$ and good conductivity compared to acetylene black (Shao *et al.*, 2006).

Acetylene black is synthesized by the partial oxidation of acetylene gas at elevated temperature. It is composed of highly aggregated and crystalline structures. Due to this it have ability to absorb electrolyte ions and bears excellent conductivity. These two characteristics makes it ideal for energy storage applications. Therefore, acetylene black is commercially used as electrode materials for energy storage applications especially for supercapacitor and batteries (Wissler, 2006).

2.2.5 Fullerene

Fullerene (C60) is hollow spherical carbon molecule (with a diameter of 7.1 Å) that consists of a truncated icosahedron with 12 pentagons and 20 hexagons connected by sp^2-hyberdized carbon atoms. It is also known as Bucky balls due to its resemblance with ball used by football association (Babu *et al.*, 2010). Fullerene was first discovered in 1985 by Richard Smalley, Robert Curl, James Heath, Sean O'Brien, and Harold Kroto. However, its structure was identified few years after by Sumio Iijima under electron microscope (Iijima, 1980). Fullerene shows excellent redox, optical and optoelectronic properties due to which it is extensively investigated in various fields. The high carrier kinetics, low re-organization energy as well as accelerated forward and backward transfer makes it ideal for next generation electronic devices such as transistors, field effect transistors (FETs), and organic solar cells (Hasobe, 2010). Figure 2.3 depicts structural feature of fullerene.

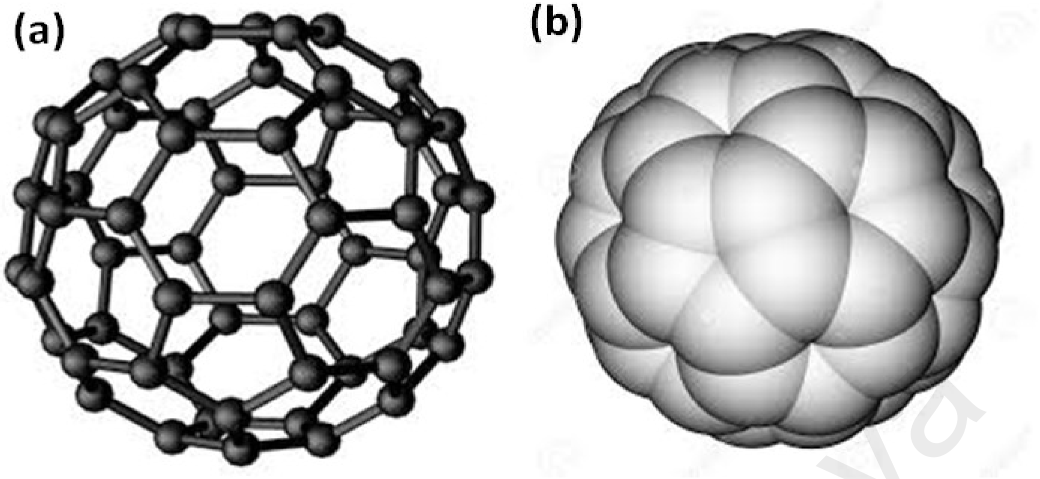

Figure 2.3: (a) Lattice structure of fullerene, (b) Solid filling of fullerene lattice structure.

Except this, fullerene is extensively exploited for medical applications in diagnostic instruments like in magnetic resonance imaging (MRI) as contrast agent, in X-ray as imaging contrast agent, photodynamic therapy and drug and gene delivery.

2.2.6 Carbon Nanotubes (CNTs)

CNTs are one of the allotropes of carbon which are in cylindrical in shape have diameter about 10,000 times smaller than human hair (Wang *et al.*, 2009). CNTs are in fact from fullerene structure family and possess good mechanical, physical, chemical, electrical and thermal properties. The structure of the CNTs is built by the rolled one atom thick sheets of carbon atom named as graphene. The major types of CNTs are single wall, doubled and multiwall carbon nanotubes. Single wall CNTs consist of single wall of graphene sheet wrapped in a seamless cylindrical form while double and multi wall CNTs consist of double and multi layers of graphene, respectively. Figure 2.4 illustrates these structures. The physicochemical properties highly dependent upon the diameter as well as the number of layers of graphene in CNTs.

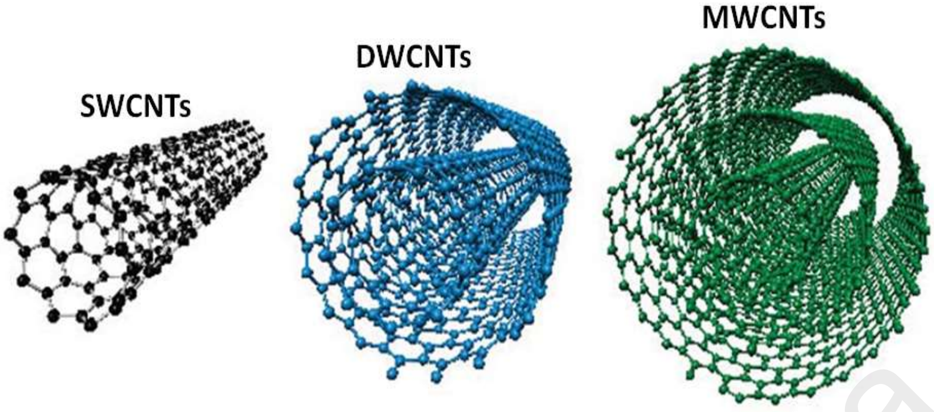

Figure 2.4: Structure of SWCNTs, DWCNTs and MWCNTs.

2.2.6.1 Synthesis of CNTs

CNTs can be prepared by various synthetic techniques. Some of the major techniques for the preparation of CNTs are: Chemical vapor deposition, Laser ablation, Plasma torch, Arc discharge.

(a) Chemical Vapor Deposition (CVD) Method

The first report on the deposition of carbon was in 1959 but CNTs were not prepared by this method until 1993 (Walker Jr *et al.*, 1959). The aligned CNTs with an average diameter of 18 mm were grown first time by the researchers from University of Cincinnati in 2007 over ET3000 carbon nanotube growth system.

In the CVD growth of CNTs, first, the substrate is coated with metal catalyst particles such as Ni, Co, Fe or combination of them (Inami *et al.*, 2007). Then substrate is heated to 700 °C and gases like ammonia, nitrogen or hydrogen and other from carbon containing gas such as methane, ethanol, acetylene or ethylene are blown into the reactor. The carbon containing gases break up at the active sites of catalyst metal nanoparticles while at the same time carbon deposit in tubular form on metal nanoparticles. The diameter of nanotubes are govern by particle size of catalyst particles. The catalyst particles usually remain at the tip of CNTs which need to remove after preparation

(Banerjee *et al.*, 2008). For commercial synthesis fluidized bed reactor is used to obtain high yield of CNTs.

(b) Laser Ablation Method

This process was developed by Richard Smalley and co-researchers at Rice University. In laser ablation method, laser is used to vaporize the graphite source in a high temperature reaction chamber and an inert gas is bled simultaneously in to the chamber (Guo *et al.*, 1995). The vaporized carbon from graphite condense at the cooler surfaces of reactor in tubular form. The main advantage of this method is precise and 70 % yield of single wall CNTs.

(c) Plasma Torch Method

This method was invented in 2000 by the Institut national de la recherché scientifique in Canada to effectively produce single wall CNTs. The process starts by the following mixture of gases consist of argon, ethylene and ferrocene into the microwave plasma torch and here it is atomized by the atmospheric pressure plasma, which has the form of an intense flame. The flame creates fumes which consist of CNTs, amorphous carbon, metallic and carbon nanoparticles (Smiljanic *et al.*, 2002). This method is efficient compared to laser ablation as energy required to decompose the gas is 10 times lesser then vaporization of graphite. Additionally, the yielding rate of CNTs in this method is very high (2 g.min^{-1}) compared to other methods.

(d) Arc Discharge Method

This is the classic method for the synthesis of CNTs. In fact, CNTs were produced in 1991 accidently, fullerene was intended to produces by using a current of 100 A to graphite electrode. The carbon suite was produced during an arc discharge containing CNTs. But the proper production of CNTs was made in 1992 by using same method but with slight modifications. This time, carbon containing electrode was kept at negative potential which was sublimated at high discharge temperatures.

Nanotubes were observed in 1991 in the carbon soot of graphite electrodes during an arc discharge, by using a current of 100 amps, which was intended to produce fullerenes. However the first macroscopic production of carbon nanotubes was made in 1992 by two researchers at NEC's Fundamental Research Laboratory. The method used was the same as in 1991. During this process, the carbon contained in the negative electrode sublimates because of the high-discharge temperatures. This method produces yields up to 30 % containing both multiwall and single wall CNTs. However, the major disadvantage of this method is use of high temperature (1700 °C or above).

2.2.6.2 Functionalization of CNTs

Raw or pristine CNTs (P-CNTs) are highly hydrophobic due to their metallic nature. Moreover, P-CNTs persist metallic residue and amorphous carbon on their tips and cylindrical structures, respectively (as mentioned above). Therefore, the surface modification of P-CNTs is required in order to remove the amorphous carbon, metallic residue and to functionalize them with suitable functional groups so that they become hydrophilic (Sadegh *et al.*, 2015). There are two major strategies for the functionalization of CNTs, one is non-covalent while other is covalent. The covalent functionalization can be further categorized by defect and side wall functionalization. By using strong oxidizing agents such as HNO_3, H_2SO_4, $KMnO_4$, $K_2Cr_2O_7$ and their combination can significantly produce defects around CNTs, where oxygen containing functional groups (carboxylic acid, ketone, alcohol and ester groups) are generated during treatment (Banerjee *et al.*, 2005). This treatment also removes the metallic impurities and amorphous carbon from the surface CNTs. The oxygen containing function groups are very important for the anchoring of metal oxide nanostructures on CNTs. These functional groups can serve as nucleation sits for the group of metal oxide nanostructures. The methods of functionalization of CNTs based on non-covalent interaction can be performed without destroying the intrinsic sp^2-hybridized structure of the nanotube sidewall, so that the original electronic structure and properties of CNTs can be preserved. Figure 2.5 depicts the pristine CNTs and functionalized CNTs.

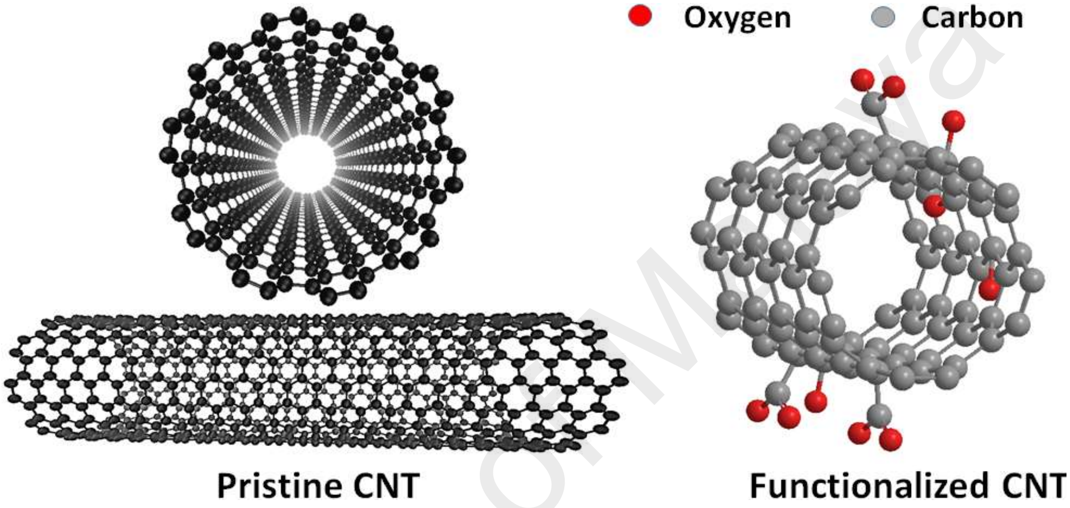

Figure 2.5: Schematic illustration of Pristine and functionalized CNTs.

2.2.6.3 Properties of CNTs

The unique hollow structure with sp^2 hybridized carbon atom strengthen the physiochemical properties of CNTs. The conductivity of CNTs is very high, that is due to the asymmetric twist in the graphene sheets. Due to the chiral indices, CNTs exhibit the properties of both metals and semiconductors. The phenomenon of electronic conductivity of multiwall carbon nanotubes (MWNTs) is very complex due to their inter-wall interactions which non-uniformly distribute the current over individual tubes. However, for single wall carbon nanotubes (SWCNTs), there is a uniform distribution of current over each part.

Since each of carbon atom in graphene sheet at the walls of CNTs is strongly bonded with its neighboring three atoms, which renders the high basal plane elastic modulus. This leads to the excellent strength of CNTs. The mechanical strength of

SWCNTs is reported to 1 TPa, which is much higher than steel. The strength of MWCNTs is not dependent on the diameter rather than the degree of disorder in nanotubes (O'connell, 2006). CNT have ability to regain its position when an applied pressure is removed from its tip. Due to this property CNTs are used in high resolution probe microscopy.

CNTs are thermally conductive. The high thermal expansion between the interlayers of walls of CNTs and zero expansion give rise to high flexibility against non-axial strains. On the other hand, the strong association among in plan carbon atoms offers outstanding stiffness and strength against axial strains (O'connell, 2006). The composite of CNTs with other materials such as polymers and metal oxides can improve the thermal and mechanical properties of composite materials.

2.2.7 Graphene

Graphene is a basic building block of graphite, which is 2D sheet of carbon atoms consist of honey comb lattice structure. The monolayer atoms in the hexagonal lattice structure of graphene sheet are sp^2 hybridized with the bond length of ~ 0.142 nm (Figure 2.6). It has basic building block of several graphitic materials such as CNTs, fullerene and graphite.

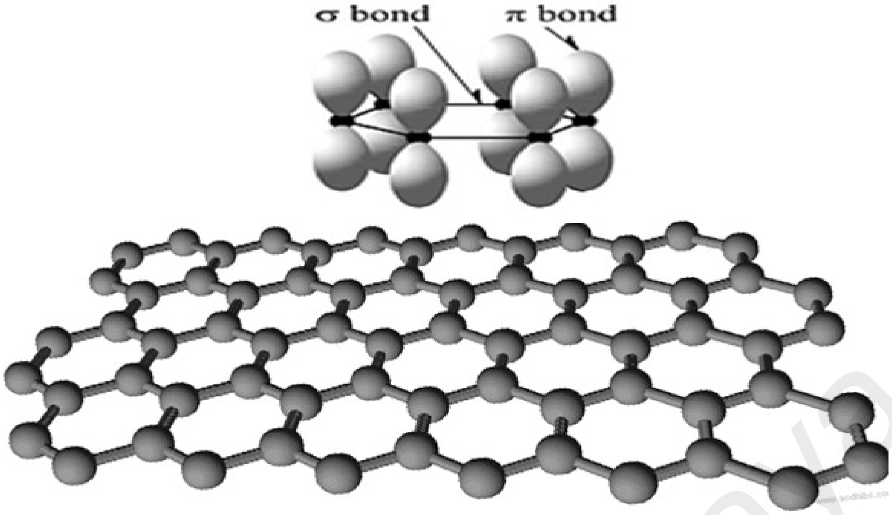

Figure 2.6: Honey comb lattice structure of graphene (inset: σ-bonds and π-bonds formed from sp^2 hybrid orbitals between the carbon atoms).

Due to the unique structure, graphene demonstrated fascinating physical, mechanical, electrical and chemical properties. It presents ballistic conductivity due to the high electron mobility at ambient temperature, outstanding mechanical strength of 1 TPa and good thermal conductivity. The sheets of graphene are stacked together due to the π-π interaction. Therefore, only top layer of graphene can be exploited for electrochemical applications. In order to de-stack the sheets of graphene, its basal plan is functionalized with oxygen containing functional groups. The electronegative functional groups un-bundled the sheets of graphene and expose more electrochemical surface area.

2.2.7.1 Graphene Oxide

Graphene oxide (also known as graphitic acid or graphitic oxide) is in fact graphene which is functionalized chemically with oxygen containing functional groups (Figure 2.7). The oxidation of graphene oxide (GO) is done by using strong oxidizing agents to produce yellowish solid or gel with graphene layers separated irregularly with large spacing. GO was prepared in 1859 by Benjamin by oxidizing graphite in the mixture of potassium chlorate and nitric acid (Banerjee *et al.*, 2005). Later on, in 1957 Hummers and

Offeman reported an easier, safer and more efficient route for the synthesis of GO. The used the mixture of H_2SO_4, $NaNO_3$, and $KMnO_4$ for the oxidation of graphite (Hummers Jr *et al.*, 1958).

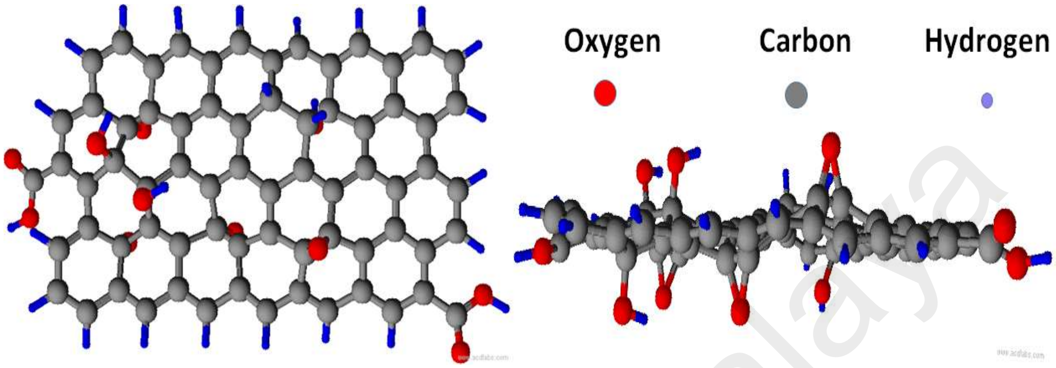

Figure 2.7: Oxygen containing functional groups on GO.

Unlike to graphite, GO is decorated with electronegative oxygen functional groups (hydroxyl and epoxy groups) on its basal plane as well as its edges. These functional groups make GO hydrophilic which facilitates the dispersion and exfoliation of GO in water under sonication. This can yield a stable single layered GO dispersion. The structural properties of GO are different than graphene even their chemical properties are similar. The graphene is electrically conductive due to its sp^2 hybridization of carbon atoms while the conductivity of GO is much lesser than graphene due to the introduction of defects or functional groups in the chain of sp^2 bonding. The removal of oxygen containing functional groups from GO can restore the conductivity but the complete removal of functional moieties has not been achieved.

(a) Synthesis

For the first time, GO was prepared in 1859 by an Oxford researcher named Benjamin C. Brodie. He used mixture of potassium chlorate and fuming nitric acid to oxidize graphite to produce paper like foils of GO with 0.05 mm thickness. However, the process was very long tedious and hazardous. In 1958, Hummers and his co-worker

Offeman developed new synthetic method to prepare GO. Their method uses low temperature during synthesis which avoids the risk of explosion. They used graphite flakes as graphene source and oxidized them in a very simple and fast way (Hummers Jr & Offeman, 1958) .

The Hummer's synthetic method for the preparation of GO can be explained in the following two steps:

(i) In the first step, graphite flakes are oxidized by strong acids to produce GO. This GO bears hydroxyl and epoxide functional groups on its basal plane and edges. These functional groups facilitate GO for easy dispersion in water.

(ii) In the second step, bulk GO is exfoliated by its dilution in water under sonication in order to produce GO mono, bi and few layers sheets.

In the typical procedure, 100 g graphite flaks and 50 g of $NaNO_3$ were mixed in to the concentrated acid of H_2SO_4 at 66 °C and then cooled down to 0 °C. Afterward, 300 g of $KMnO_4$ was added under constant stirring followed by diluting the solution mixture by adding water. The final colloidal mixture was consisted of 0.5 % of solid which was then purified to remove the impurities and dehydrated with P_2O_5 (Li *et al.*, 2014).

(b) Properties

Due to the insertion of functional groups in the honey comb lattice structure of graphene, GO comes up with improved physiochemical properties. The most important feature of GO is its high hydrophilicity. This high dispersion nature of GO is owing to the functional moieties at its basal plane and edge. These functional groups are also very important for the integration of metal oxide nanoparticles on GO sheets. The functional group can serve as nucleation site for the effective growth of metal oxide nanostructures during chemical synthesis techniques. One of distinct advantage of functional groups on

GO is its role for adsorption of different molecules. This adsorption of certain molecules at functional groups cites especially helps in electrochemical sensing applications. Once target molecule adsorbed on the surface of GO, then it can be easily oxidized or reduced under certain electrical potential. In addition, the presence of these functional groups makes an effective functionalization with various biomolecules and polymers for applications (Pandikumar *et al.*, 2014). However, all above features of GO are because of its conductivity. Since the *sp*^{2} hybridization of carbon atom in graphene is interrupted by the insertion of functional groups, therefore the conductivity of the GO is very less compared to pristine graphene.

2.2.7.2 Reduced Graphene Oxide

Reduced graphene oxide (rGO) is produced by removal of oxygen containing functional groups or simply reducing the GO. Upon reduction of GO, most of the functional groups are removed (not all) from the basal plane and edge sites. This results in restoring of *sp*^{2} hybridization of carbon atom chain which significantly improves the conductivity. At the same time the repulsion of electronegative functional groups reduces which causes the restacking of graphene sheets. The complete reduction of GO to rGO cannot be achieved, therefore, rGO holds the advantages of GO and pristine graphene. The conductivity of rGO is higher than GO while less than pristine graphene, while interspace distance of graphene sheets in rGO is less than GO and higher than graphite.

The method for the reduction GO is vitally important and has great effect on the quality of rGO produced. GO can be reduced by various methods which involve physical and chemical treatment. However, the quality of produced rGO is governed by the method used to reduce GO. In some of the treatments the rGO produced bears the properties similar to pristine graphene. Following are some of the treatment to convert GO into rGO.

(a) Chemical Methods

Hydrazine hydrate (H_6N_2O) is a strong reducing agent which can effectively reduce GO. Treating GO with H_6N_2O can produced high quality rGO. But this method is not green. Some of mild reducing agents like urea and ammonia can also reduce GO. However, in this case, the degree of reduction is less compared to H_6N_2O. Except this, natural plant and vegetable extracts (form ginger, garlic, and capsicum etc.) are also used to convert GO into partially rGO.

(b) Physical Methods

In physical treatments, GO is exposed to radiations or heated to for long durations to produce rGO. GO can be converted into rGO by exposing it to high intensity or strong pulse lite such as laser or xenon flashtubes. Heating GO to high temperatures (1000 °C or more) can also remove most of the functional groups from its basal planes. The produce rGO in this method have a very high surface area, close to that of pristine graphene even. But elevated temperature causes structural defects in the honey comb lattice of rGO.

(c) Electrochemical Methods

Electrochemical reduction of GO is a method that has been shown to produce very high quality reduced GO, almost identical in terms of structure to pristine graphene. This process involves coating various substrates such as indium tin oxide or glass with a very thin layer of GO. Then, electrodes were placed at each end of the substrate, creating a circuit through the GO. Finally, linear sweep voltammetry was carried out on the GO in a sodium phosphate buffer at various voltages; at 0.6 V reduction began, and maximum reduction was observed at 0.87 V. In recent experiments the resulting electrochemically reduced GO showed a very high carbon to oxygen ratio and also electronic conductivity readings higher than that of silver (8500 Sm^{-1}, compared to roughly 6300 Sm^{-1} for silver). Other benefits of this technique are that there are no hazardous chemicals used, meaning no toxic waste to dispose. Unfortunately, the scalability of this technique has come into question due to the difficulty in depositing GO onto the electrodes in bulk form. These are just a sample of the numerous methods that have been attempted so far. Reducing GO by using chemical reduction is a very scalable method, but unfortunately the rGO produced has often resulted in relatively poor yields in terms of surface area and electrical conductibility.

2.3 Transition Metal Oxides

In modern era of chemistry, physics, material science, biotechnology and so on, metal oxides play a significant role and have been the center of attraction by scientific world (Henrich *et al.*, 1994; Noguera, 1996; Rodriguez *et al.*, 2007). Elemental metal has the tendency to form diverse varieties of oxide compounds. These compounds may exhibit a diverse range of structural geometries along with unique electronic properties. They might demonstrate metallic, semiconducting or insulating properties. Metals oxides have been applied in wide varieties of application including, catalysis, sensors, coating materials, fuel cells, piezoelectric devices, microelectronic circuits, photocatalysis and so on (Fernández-García *et al.*, 2011). In the emergent arena of nanotechnology, an objective is to synthesis nanoarrays and nanostructures having distinctive properties as compared to the bulk or single particle species. Metal oxide nanoparticles reveals exclusive physical and chemical properties owing to their restricted size and a higher density of corner or edge surface sites. The particle size in any material usually affects structural, characteristics such as symmetry of lattice and cell parameters. The decrease in particle size is associated with the decrease in the surface free energy of the material which changes its thermodynamic stability drastically as compared to the bulk material. As a result, nanomaterials exhibit enhanced mechanical and structural stability as compared to the bulk material (Cao *et al.*, 2004).

Recently, scientific investigations comprising nanoparticles and nanoscale materials have created an excessive amount of curiosity from researchers and engineers of almost all disciplines. This attention has been caused due to the investigations that a large number of physical properties are size dependent, comprising surface reactivity, optical and magnetic properties, melting points, specific heats and so on. These properties, which are considered to be size-dependent, are extensively said to be the outcome of the higher ratio of surface area as compared to bulk atoms along with the associating state they epitomize between atomic and bulk materials. Materials in nanoscale range, mainly metal oxides, might be considered as they neither belong to atomic size species which are characterized by distinct molecular orbitals, nor as bulk materials which possess electronic band structures, but relatively by size-reliant widened energy states. Since metal oxides own prominent significance industrially, therefore, it is necessary to have an extensive understanding of their properties as small clusters to bulk materials. Even though, these nanoscale metal oxides are of great importance to researchers of various disciplines, approaches for their synthesis and applications are largely the focus of chemists (Interrante *et al.*, 1997).

2.3.1 Synthesis

The synthetic protocol for the preparation of metal oxide nanostructures is vitally important as it governs the physiochemical properties of the metal oxides nanostructures. To design simple, cost effective and innovative synthetic method that can be industrialized is a challenge. Currently, several methods are being used for the production of high yield of metal oxide nanostructures. The details of these methods are given below.

2.3.1.1 Chemical methods

The chemical synthesis techniques (also known as bottom up methods) are extensively used for the synthesis of metal oxide at industrial scale. The synthesis of nanoparticles in these approaches is primarily done by the chemical reduction of metallic salts or the decomposition of organometallic compounds in a controlled fashion. Variety of reducing agents for reduction of metallic salts, donor ligands, templates and surfactants are used to control the particle size, morphology and porosity of metal oxide nanostructures. In order to achieve the uniform growth and to eliminate the agglomerations, carbon supports (graphene, CNTs, carbon black etc.) and polymeric compounds are used. The most commonly used chemical methods for the synthesis of metal oxide nanostructures are described as follow:

(a) Co-precipitation Method

It is quite old and common synthetic technique for the preparation of nanostructured materials. In co-precipitation method a suitable amount of metal oxide precursors such as metal acetates, nitrates, chlorides phosphates etc. are dissolved in a solvent (mostly water). The metal hydroxide is formed by adding base which undergoes complexation with metal ions. The metal hydroxide can be converted to metal oxide by heating the same solution mixture or by calcination the prepared metal hydroxide power. This method is facile and can be used at industrial scale. However, to achieve the chemical homogeneity and to tune uniform particles size, surfactants can be used (Fernández-García & Rodriguez, 2011).

(b) Hydrothermal Method

Hydrothermal method is a wet chemical method which uses elevated temperature, pressure and time to produce metal oxide nanostructures. In this route, metal salts are dissolved in solvent and then heated at temperature under high pressure using stainless steel autoclaves. The metal salts decompose in metal oxide in high pH solvent. The particle size and morphology can be controlled by tuning the reaction parameters such as pH, time, temperature and amount of precursor salt. Hydrothermal route also allows to use surfactant as solvent for the uniform growth of metal oxides (Shahid *et al.*, 2014) . This method is able to produce variety of morphologies of metal oxides such as nanowires, nanobelts, nanosheets, nanocubes, nanoplatelets, nanoflowers etc. with very uniform very fine particle size (Shahid *et al.*, 2015).

(c) Microemulsion Method

Microemulsion method is mainly based on formation of micelles or reverse micelles structures which act as nano-cavities for the preparation of metal oxides during the synthesis. The direct micelles or reverse micelles serve as micro or nano-containers for metal oxide salt solution in the presence of surfactants such as oil and water in the reaction mixture. Metal oxides precursors solution in water will undergoes precipitation as oxo-hydroxides which is monodispersed in nature due to the presence of surfactant molecules. Metal oxides nanoparticles with controlled particle size can be synthesized using this technique (Malik *et al.*, 2012; Uskoković *et al.*, 2005).

(d) Sol-gel Method

Sol-gel method is economical and simpler for the production of metal oxides compared to other chemical methods. This method uses hydrolysis of metallic salts in alcoholic solutions producing metal hydroxide gels which are further dried and calcined to obtain metal oxide nanoparticles. The metal salts are usually dissolved in alcoholic solvents to produces metal alkoxide. The hydrolysis results in the formation of oxo-hydroxides. Water is removed through oxo-hydroxide by condensation to produce gel. During condensation the hydroxyl moieties polymerize and produce porous as well dense hydroxide network. Finally, the gel is dried and calcined at high temperature to produce porous metal oxide nanostructures (Interrante & Hampden-Smith, 1997; Livage *et al.*, 1988).

(e) Template Method

Template method is efficient route to produce controlled particle size and morphology of metal oxide nanoparticles. Very fine with uniform pore size and diverse morphologies can be produced in a very controlled fashion. In this method host template material with uniform voids are used to trap the nanoparticle precursor. Metal oxide nanoparticles can grow over the host template and the template is then removed in the final stage by using solvents that can dissolve template resulting in very fine and with uniform pore size nanostructured metal oxide. Template methods are commonly used in some of the prior stated approaches and specifically applies two types of templates, soft-templates (surfactants) and hard-templates (porous solid materials such as silica or carbon) (Ciesla *et al.*, 1999; Wang *et al.*, 2006).

2.3.1.2 Physical Methods

Physical synthetic methods are also known as top-down techniques for the preparation of nanomaterials. In these approaches, physical treatments are employed to convert bulk materials into nanomaterials. The physical treatments used to prepare nano scale materials involve physical forces such as grinding, milling, vapor phase deposition etc. The important physical synthetic methods are explained below:

(a) Mechanical Attrition

Mechanical attrition is one of the most important and commonly used methods to transform bulk material in to micro or nanomaterials using mechanical milling or attrition. The milling can be categorized in to two types that is high energy milling and low energy milling. The type of milling can be employed depends upon the size of the nanoparticles required. The main objectives of milling is to convert large scale material into nanoscale material and to merge particles in new phases. Unlike to other synthetic techniques described above, mechanical attrition produces nanostructures through structural decomposition of cruder grained structures instead of cluster assembly (Koch, 2003).

The ball milling and rod milling systems have attained ample consideration as a potent tool for the production of numerous advanced materials. Mechanical attrition is a distinctive technique which can be carried out at room temperature. The procedure of mechanical attrition has been performed on both, high energy mills, vibratory type mill, centrifugal type mill, and low energy tumbling mill (Suryanarayana, 2001).

(b) Mechanochemical Synthesis

In this synthetic technique chemical transformation of materials in to nanoscale is done by mechanical mean such as compression, shear, milling or friction (Xu *et al.*, 2015). In fact, the energy required to activate the chemical reaction is provided by the mechanical treatment. The combination of mechanical and chemical process on molecular level have paved way to a unique methodology for facile synthesis of nanoparticles (Rajput, 2015). In mechanochemical process, a standard solid state displacement reaction takes place by using mechanical force which leads to nanostructured material with minimum particle size up to 5 nm with in the bigger by-product phase particles (Lue, 2007). This technique is extensively employed since very long ago for the preparation of variety of metal/metal oxide nanoparticles such as Ag, Co, Cr, Cu etc., (Rajput, 2015). Mechanochemical synthetic process offers tuning of various such as volume fraction of the by-product phase made through milling, time duration of milling, energy of milling collision, ball-to-powder mass ratio, ball size, temperature, and the usage of method control agents.

(c) Chemical Vapor Deposition

This technique is used to produce solid state nanomaterials with high performance. Chemical vapor deposition (CVD) is widely used in semiconductor industry to produce thin films. In this method solid material usually in the form of thin film is deposited on pre-heated substrate by the help of vapors of gas phase. In order to initiate CVD, activation energy is required to start synthesis of nanoparticles. This action energy may be in the form of heat, laser, ultraviolet radiations etc., therefore CVD can be categorized in different types on the basis of source of activation energy (Sherman, 1987). In thermal CVD, activation energy to initiate the reaction is provided by elevated temperature (up to 900 °C). In case of plasma CVD, the reaction is triggered by plasma at temperatures range of 300 and 700 °C. In laser equipped CVD technique, pyrolysis of bulk solid takes place upon the adsorption of heat from laser thermal energy which eventually leads to nanoscale material synthesis. In photo-laser equipped CVD, the ultra violet radiation induces the chemical reaction which has adequate amount of photon energy to breakdown the chemical bond in the reactant molecules. Alternative method termed as chemical vapor condensation (CVC) was established in Germany in 1994. It comprises pyrolysis, under the reduced pressure atmosphere, of the vapors of metal-organic precursors. Nanoparticles of metal oxides such as ZrO_2, Y_2O_3 and nano-whiskers have been synthesized by exploiting CVC method (Chang *et al.*, 1994; Rajput, 2015).

(d) Laser Ablation

In laser ablation synthesis method high energy laser pulses are used to produce nanoparticles. This technique is efficient compared to other synthesis methods due to its ability to produce uniform particle size of nanostructured materials. The process of laser ablation can be divided in to two steps: (1) evaporation of target solid material and (2) hydrodynamic expansion of the ablated product in the ambient gas (Amoruso *et al.*, 2005). The formation of metal oxide nanoparticles via pulse laser ablation (PLA) can be done in two stages. In first stage, the atomic vapors of the aimed solid material are produced by the PLA. In final and second stage, growth of nanoparticles starts by capturing the atoms produced by PLA (Han *et al.*, 2002).

2.3.2 Properties of Metal Oxides

2.3.2.1 Surface Properties

The physical and chemical properties on any material mainly depends upon its surface properties regardless of its bulk or nanoscale nature. Surfaces execute various purposes such as they maintain things in or out; they permit the movement of energy or a material through an interface; they can either initiate or terminate a chemical reaction, like in the case of catalysts. When a bulk solid or material is further segmented into the nano-regime materials, the total collective surface area is significantly enhanced although the total volume remains the same. As a consequence, the surface-to-volume ratio of the material is increased manifolds as compared with the bulk parent material.

In any material, the properties are usually determined by the chemical groups present on the surface of that substance. Important material properties such as reactivity, adhesion, catalytic behavior, electrical resistivity and gas adsorption or storage exclusively rest on the nature of the interface of material. Nano-scale metal oxides possess substantial amount of atoms present at their surfaces, which have a significant affects on surface related properties such as physical adsorption of various compounds, catalysis reaction including photocatalysis, sensor detection reactions and so on. The presence of large number of atoms at the surface of the nanoparticles of metal oxides effects physical properties such as melting point, boiling point, morphology and chemical nature. For instance, the melting point of nano-metal oxides will be lower as compared to the bulk metal oxides since the surface atoms are easier to remove as compared to bulk atoms, thereby decreasing the amount of energy required to overcome the intermolecular forces of attraction holding the atoms, thus decreasing the melting point. Thus surface properties of metal oxides are changed drastically upon converting them into nano-sized materials which can exploited in various areas of scientific research.

2.3.2.2 Electrical Properties

Electrical property of metal oxides is one of the important parameter which can be explored in numerous applications including photocatalysis studies, sensors applications and so on. Metal oxides can exhibit ionic or mixed ionic conductivity and has been proved experimentally that this property is significantly size dependent which can be tailored by controlling nanostructures of metal oxides (Fiiipponi *et al.*, 2012). As per the Boltzmann statistics, the number of electronic charge carriers in metal oxide depend upon the fundamental band energy gap. The electronic conduction in metal oxides, based upon charge carrier, is stated to as *n*- or *p*-type, respectively, for electrons or holes. The number of charge carriers, that is, free electrons or holes, can be significantly enhanced by introducing non-stoichiometry which can easily be balanced by less mobile oxygen/cation vacancies present in metal oxides. Similar to the hopping-type conduction due to the electrons and holes, ionic conduction can also takes place in the metal oxides where the respective ions can move from site to site by hopping within the crystal lattice due to thermal activation in accordance with the modified Fick´s second law (Fiiipponi & Sutherland, 2012).

The behavior of the charge carriers in polycrystalline oxides is greatly influenced by the size since conductivity runs parallel to the surface properties of materials. The strain at the particle boundaries and total surface energy, which contributes in electrostatic potential of metal oxides, are significantly altered at nano-scale as compared with bulk material. The distribution of the charge carriers or defects within the crystal lattice of metal oxide also undergoes momentous modifications from bulk materials to nanomaterials, since nanoparticles contains charge carries over the entire material as a result of the shielded electrostatic potential reduction at surface layers of nanosized materials (Rodriguez & Fernández-García, 2007). As an outcome of these nanoscale derived effects, it is a renowned fact that metal oxides in nano-scale displays enhanced conductivity which could be many order of magnitude larger than the analogous bulk or micro-crystalline metal oxides, and is attributed to a noteworthy augmentation of the electronic contribution.

2.3.2.3 Optical Properties

The optical properties of a material are due to the interaction between the light and the matter. One of the important fundamental properties of metal oxides is the optical conductivity which can be calculated experimentally via reflectivity and absorption analysis. It is a well-known fact that reflectivity is, undoubtedly, a size-dependent property as scattering phenomenon can be considerably changed when the size of metal oxides particles fall within or out of the wavelength range of photon (Scott *et al.*, 2001). Owing to quantum-size internment, light absorption usually becomes both discrete-like and size-dependent. For nano-metal oxides, the transitions between discrete or quantized electron and hole results in the development of both linear (one exciton per particle) and non-linear optical (multiple excitons) properties. Thus, nano-sized metal oxides proved to be promising materials for novel optical properties which can be applied in diverse scientific areas of research.

2.3.2.4 Other Properties

Besides the above discussed properties, metal oxides exhibit distinctive chemical, mechanical, catalytic and adsorption properties. Metal oxide nanoparticles have been extensively employed for industrial applications in the field of catalysis as active compositions or as supports materials. Metal oxides possess photocatalytic abilities which can be exploited to solve present day energy crises. In 1972, Fujishima and Honda first reported the photocatalytic splitting of water using TiO_2, which was the initial photocatalyst appropriate for water splitting and the commencement of a new field of modern heterogeneous photocatalysis. Currently, metal oxide nanoparticles owing to large surface to volume ratio and enhanced surface binding properties have been employed as adsorbent to remove environmental pollutants. Metal oxide nanoparticles exhibit stability towards radioactive radiations, thermal and mechanical changes and are exploited for the irreversible, selective and efficient removal of large amounts of pollutants from contaminated water. Thus metal oxide in nanoscale have demonstrated unique and distinctive properties and have been applied extensively in the field of chemical, nuclear-energy, pharmaceutical, food, bioengineering, dairy, water treatment, and electronic industries.

2.3.3 Cobalt Oxide (Co_3O_4)

In the family of various transition metal oxides, cobalt oxide (Co_3O_4) breathed new life in the field of nanomaterials as a promising catalyst (Moro *et al.*, 2013). It is spinal shaped *p*-type semiconductor with spinal structure bearing both direct and indirect band gap. Moreover, Co_3O_4 crystal consists of unique structure having magnetic Co^{2+} and non-magnetic Co^{3+} occupying tetrahedral and octahedral sites respectively, in the crystal (Xie *et al.*, 2009). These polar sites of Co_3O_4 crystal can play vital role in the catalytic activity, especially facilitating rapid charge transfer kinetics on the surface of the electrode. The high aspect ratio, unique crystal structure together with diverse morphologies make it as an ideal candidate for electrocatalytic applications. Due to these distinct characteristics, unaided Co_3O_4 nanostructures have been reported for electrocatalytic applications (Mu *et al.*, 2013) . But the hybridizing the Co_3O_4 nanoparticles with conducting polymer and carbon based materials can significantly enhance the performance by improving the effective electrochemical surface area and reducing the charge transfer resistance. Recent reports unveil the potential of Co_3O_4 nanostructures supported on carbon based materials for energy conversion (Shahid *et al.*, 2014), energy storage (Numan *et al.*, 2016) and electrochemical sensing applications (Numan *et al.*, 2017).

2.4 Supercapacitors

2.4.1 Overview

The phenomenon of charging a surface or a body storage is quite old, when particular surfaces are charged by rubbing with amber. However, the proper device for the charge storage named Leyden jar was invented first time in 18th century by Pieter van Musschenbroek of Kamin and Dean Kliest at Leydenb (Conway, 1999).

The Leyden jar was consists of a glass jar which contains acidic electrolyte as conducting medium. A metal foil is cemented to the inside and the outside surfaces, and a metal terminal is projecting vertically through the jar lid to make contact with the inner foil. The glass medium is used as a dielectric between the conducting metal coating on the inner and outer surfaces. The outer and inner surfaces store equal but opposite charge and this double layer charging occurs due to the presence of the acidic electrolyte. Charging of the Leyden jars were usually carried out using electrostatic generators such as the Hawkesbee machine. This device was initially named as condenser.

In the start of 20th century, Alessandro Volta modified the Leyden jar into electrophoresis which was operated manually and was able to produce charge by the phenomenon of electrostatic induction (Brusso *et al.*, 2014). In this device, glass was replaced with hard plastic (ebonite) serving as dielectric material which was sandwiched between two metallic electrode plates. However, first proper electrochemical capacitor was patented by Becker and his employer General Electric in 1957 which comprises of carbon electrodes with aqueous electrolyte using interfacial double layer effect to store electrical energy (Becker, 1957). The commercial supercapacitors was made available in

1966 by SOHIO Corporation. This supercapacitor was based on carbon electrodes and alkyl ammonium salt as solid electrolyte. It was able to provide high energy density with extended operating potential window (3.4 ─ 4.0 V) (Boos, 1970). In 1975, Conway and co-workers developed a supercapacitor which used similar charge storage mechanism like batteries. They fabricated pseudocapacitor which was based on electrodes having transition metal oxide such as RuO_2. Pseudocapacitors undergo chemical reaction for energy storage instead of electric double layer effect which was found in supercapacitors based on carbon electrodes. Although, their charge storage mechanism was similar to batteries but they were able to mimic the response like traditional supercapacitor with high reversibility (Conway, 1999). Therefore, supercapacitors are characterized in two major types based on their charge storage mechanism. The types and the charge storage mechanism of supercapacitor are described below.

2.4.2 Working Principle

As mentioned earlier, that supercapacitor can store charge in two ways, either by chemical reaction or by electric double layer effect. So, based on charge storage mechanism, supercapacitor is characterized as electric double layer capacitors (EDLC) and pseudocapacitor. EDLCs are commonly based on carbonaceous electrodes which stores charge by non-faradaic reaction forming the double layer of charges at electrode/electrolyte interface (Chong *et al.*, 2017). On the other hand, pseudocapacitor undergoes fast and reversible faradaic reactions to store the charge on its electrodes (Omar *et al.*, 2017). In pseudocapacitors, electrode material is usually metal oxide, conducting polymers or their composites. Depending on the nature of the electrode material, supercapacitors can sometimes store energy using both mechanisms, simultaneously (Omar *et al.*, 2017). The charge storage mechanism in EDLC and pseudocapacitor is explained here, in detail to provide better understanding.

2.4.2.1 Charge Storage in Electric Double Layer Capacitor

The principal charge storage mechanism of EDLC is by electrostatic way, where both positive and negative charges accumulate at the electrode surfaces which are separated by some dielectric or vacuum. This phenomenon of charge storage is also known as non-faradaic electrical storage. The process of formation of electric double layers at the interface of electrode and electrolyte is explained by various models.

Helmholtz was the first who explained the concept of electric double layer. He gave comprehensive description of the distribution of charges at the interface of colloidal particles. According to his model, double layer of charges consist of two layers of opposite charges which are separated by a distance equal to atomic dimension (shown in Figure 2.8(a)). The two layers of opposite charges behave like two oppositely charged plates of conventional capacitor. Later on, Helmholtz double layer model was improvised for the solid electrode interface. Here, the charge density of positive and negative charges is balanced by the counter ions at the electrode/electrolyte interface by a distance of one atomic dimension from the solid electrode surface. But after the Helmholtz double layer model, it was realized that the ions of electrolyte in double layer are not static like how they were shown as compact array in the model. Instead, they are subjected to the effects of thermal fluctuations.

To cover this loophole, Gouy and Chapman modified Helmholtz model and proposed new model named as diffuse double layer model. They accommodated the effects of thermal fluctuations on continuous distribution of electrolyte ions. According to this model, the counter ions conjugated to the electrode imagined were considered as 3D diffusely distributed population of anions and cations of the electrolyte (Figure 2.8(b)). The ions were assumed as point charges with electrolyte having total charge density equal to the opposite charge density on the electrode surface. However, the Gouy-Chapman model leads to overestimation of the double layer capacitance since the capacitance of two separated arrays of charges increases inversely with their separation distance (Zhang & Zhao, 2009).

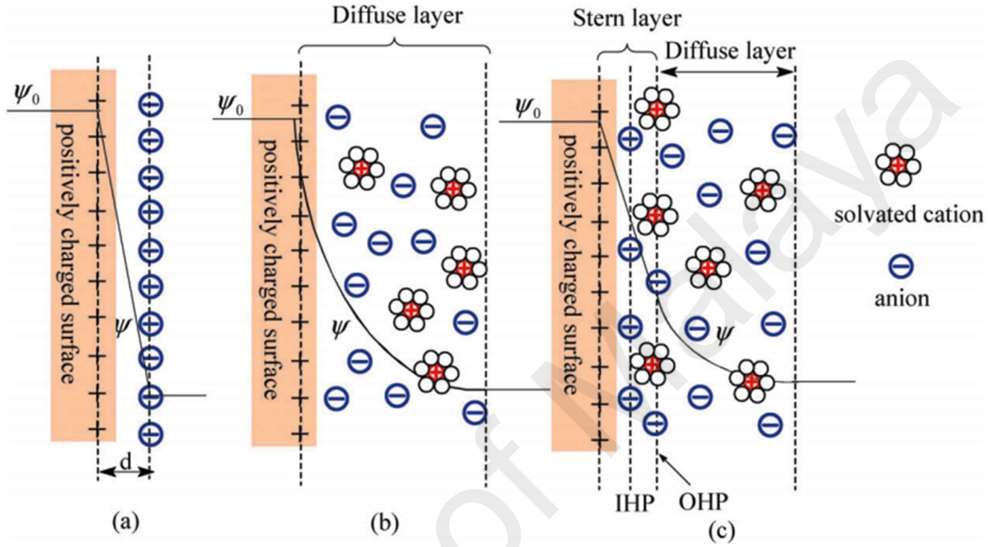

Figure 2.8: Models of electrical double layer at a positively charged surface: (a) the Helmholtz model, (b) the Gouy-Chapman model, and (c) the Stern model showing the IHP and OHP. *d* is the double layer distance described by Helmholtz model. ψ_0 and ψ are the potentials at the electrode surface and the electrode /electrolyte interface, respectively (Zhang & Zhao, 2009).

In the start of 20th century (1924), Stern rectified the discrepancy of over estimation of double layer capacitance. He combined the models of Helmholtz and Gouy-Chapman which he applied for two regions of ions distribution. The inner layer is called the Stern layer or compact layer and beyond the inner layer diffuse layer (Conway, 1999). The Stern layer corresponds to the adsorption of ions (according to Langmuir's adsorption isotherm), where the ions are firmly adsorbed on the electrode surface due to which it is also referred as compact layer. The inner Helmholtz plane (IHP) located in the stern layer refers to the distance of the closest approach of specifically adsorbed ions (ions that are in direct contact to the electrode). The outer Helmholtz plane (OHP) marks the end of the inner region and beginning of the diffuse layer as shown in Figure 2.8(c). The OHP refers to the non-specifically adsorbed ions is also what the Gouy and Chapman model defines.

In this model, the ions were recognized as having finite sizes, including the annular thickness of the hydration shell. Hence, the geometrical limit to the compact region of the adsorption layer at the electrode can be determined easily. The overall capacitance in the electric double layer (C_{dl}) can be represented as the combination of the capacitances from the two regions, the inner region resembles to a Helmholtz type of compact double layer capacitance (C_H) and the diffuse region capacitance (C_{diff}). Thus C_{dl} can be expressed by the following equation:

$$\frac{1}{C_{dl}} = \frac{1}{C_H} + \frac{1}{C_{diff}} \tag{2.1}$$

The capacitance of two separated layers of charges increases inversely as their separation distance as presented by the Gouy-Chapman model. This leads to large capacitance values since the limit of infinitesimally small ions closely approaches the electrode surface. This overestimation of the double layer capacitance is automatically avoided by the introduction of a distance of closest approach of finite-sized ions and thus geometrically defining a compact Helmholtz inner region. The Stern model of double layer remained as a good basis for general interpretation of the electrode/electrolyte interface phenomena until the detailed work of Grahame in the 1947 on the double layer capacitance (Grahame, 1947).

2.4.2.2 Charge Storage in Pseudocapacitor

Apart from the EDL capacitance in which the charges are stored electrostatically (i.e., non-Faradaically), complement to this type of capacitance is the so-called "pseudocapacitance". The term "pseudocapacitance" is used to describe the behavior of electrode materials that have the electrochemical signature of a capacitive electrode but in which the charge storage originates from a completely different reaction mechanism (Brousse *et al.*, 2015).

Pseudocapacitance involves the passage of charge across the double layer that is Faradaic in origin whilst capacitance of EDL comes from the charge separation in the double layer formed at the interface between the solid electrode material and the liquid electrolyte. Pseudocapacitance arises for thermodynamic reasons between the extent of charge acceptance (Δq) and the change of potential (ΔV) (Conway, 1999). The following derivative is equivalent to the capacitance.

$$C = \frac{d(\Delta q)}{d(\Delta V)} \tag{2.2}$$

Generally, there are two types of electrochemical processes that contribute to pseudocapacitance which include the redox reaction at the transition metal oxide's surface with ions from the electrolyte, and the doping and dedoping of active conducting polymer material in the electrode. The former process is based primarily on surface mechanism and hence it is highly dependent on the surface area of the electrode material. The latter process involving the conducting polymer material is more of a bulk process and much less dependent on its surface area although a relatively high surface area is useful in the distribution of electrolyte ions to and from the electrodes in a cell (Burke, 2000). In all cases, the electrodes must have high electronic conductivity to distribute and collect the electron current.

It is now known that the about 1-5 % of the capacitance of carbon-based double layer capacitors is contributed by pseudocapacitance due to the Faradaic reactions of the oxygen-functionalities on the surface (depending on the conditions of preparation of the carbon material). On the other hand, pseudocapacitors will always exhibit some electrostatic double layer capacitance component of about 5-10 %, in some case even higher, depending on the surface area of the pseudocapacitor electrode. This non-Faradaic contribution is proportional to their electrochemically accessible interfacial surface area (Conway, 1999).

2.4.3 Hybrid Supercapacitor

Energy storage and power management are very crucial to satisfy the increasing demands of uninterrupted portable power sources. However, the development of energy storage system is lagging behind the quick advancement in electrical powered industries. Batteries can store high amount of energy through electrochemical reactions (called faradaic reaction), but suffer from poor power density which is not suitable for application that require bursts of energy (Ramadoss *et al.*, 2013; Shan *et al.*, 2016). On the other hand, EDLCs are receiving extensive attention due to their efficiency of delivering energy much quicker than batteries.

Currently, carbon based materials are being used as the EDLC electrode materials for commercial applications. Energy is stored in an electric double layer via fast adsorption of electrolyte ions by the EDLC materials (also known as non-faradaic reaction) which enable rapid charge storage recovery. Nonetheless, the major challenge is the energy density of EDLC, which is still lower than batteries in aqueous electrolyte (Salunkhe *et al.*, 2011). Thus, these motivated researchers develop hybrid supercapacitors which combines the EDLC-type materials with battery type materials to gain benefits from both non-faradaic and faradaic reactions. The EDLC-type materials provide high power whereas battery type-materials promise high energy output. Substantial efforts have been devoted on the synthesis and characterization of materials with abundance electroactive sites and robust crystal structure. These characteristics offer a high specific capacity and power density as well as cyclic stability. In this research, hybrid supercapacitor is fabricated in order to harvest the advantages of EDLC and battery in a single device.

2.4.4 Applications of Supercapacitors

One vital application of supercapacitors is in regenerative brake systems that are often used in hybrid electric vehicles. Energy storage in transportation involves not only the propulsion (starting and stopping) of vehicles, but also secondary power requirements such as cruising power requirements of vehicles (Douglas & Pillay, 2005). In conventional brake system, brake pads produce friction with the brake rotor to slow or stop the vehicle, turning kinetic energy to heat. However, with the regenerative brake system, the vehicle's electric motor will enter a reverse mode upon braking, causing it to run backwards, and thus slowing the car's wheel. While running backwards, the motor will act as an electric generator, producing electricity which is transferred to the capacitor for storage. The electric energy stored is used to propel the vehicle or motor assistance mode, increasing the fuel efficiency of vehicles. In real-world driving conditions with frequent acceleration and braking, the 'i-ELOOP' is able to improve fuel economy by approximately 10%.

2.4.4.1 Stationary Electrical Energy Storage

Supercapacitors are useful as energy storage systems in micro-grids and power grids. A power grid is an interconnected network consisting of generating stations that produce electrical power, high-voltage transmission lines and distribution lines to consumers whereas a micro-grid is a small-scale power grid that can operate independently or in conjunction with the area's main power grid. Supercapacitors are useful in ensuring grid stability by absorbing the energy and releasing it at the right time to prevent dropouts, especially when the power generation are from intermittent renewable energy sources. As an increased amount of intermittent renewable energy such as solar and wind penetrates the grid, the output becomes increasingly unstable. It is very important to increase the reliability and efficiency of using these renewable energy sources. By using supercapacitors, the power quality problem in distributed power generation (e.g. voltage fluctuation) can effectively be solved. Maxwell Technologies® provide supercapacitors to address the exact issues that are capable to fill in short-term power intermittencies and provide ramp rate control for longer intermittencies.

2.4.4.2 Portable Power Systems

Supercapacitors have also been used as energy backup supplies in consumer appliances. The supercapacitors are still able to provide energy to the system in the case of power outages, where there is a brief interruption in power supply. The use of supercapacitors is better than batteries because they can deliver much higher voltage in a limited amount of time. Moreover, supercapacitors have longer lifetime as compared to batteries. This means that supercapacitors do not need to be replaced regularly, effectively reducing the cost of appliances. Since then, energy backup systems for consumer electronic products are one of the biggest markets for supercapacitors.

Batteries are generally poor at power delivery whereas supercapacitors suffer from low energy density to sustain peak load for long periods of time. Hence, by combining supercapacitors and batteries, their drawbacks are minimized. The use of supercapacitors in parallel with batteries will smooth out the severe load demand of batteries by meeting the peak power requirements, whilst the batteries supply the average load (Kuperman *et al.*, 2011). The decreased of pulsed current drawn from the battery results in an extended battery lifetime. This combination is particularly useful in portable power tools where peak current demand is high. Applications of supercapacitor can easily be found in satellite TV (TV-channel setting and clock time), car audio systems (radio station memory), coffee machines (programmed functions), programmable pocket calculators, camera flash and toys, etc.

2.5 Electrochemical Sensors

2.5.1 Overview

Since the early 70's electrochemistry has been used as a powerful analytical technique for monitoring electroactive species in living organisms. In particular, after extremely rapid evolution of new micro and nanotechnology it has been established as an invaluable technique ranging from experiments in vivo to measurement of exocytosis during communication between cells under in vitro conditions (Wang *et al.*, 2008). Electrochemical sensors for the measurement of analytes of interest in clinical chemistry are ideally suited for these new applications, due to their high sensitivity and selectivity, portable field-based size, rapid response time and low-cost. The modern concept of using electrochemical sensors to determine the concentration of substances and other parameters of biological interest has represented a rapidly expanding field of instrument design since 1962, when Clark and Lyons invented the first electrochemical biosensor, known as the 'enzyme electrode', using the enzyme glucose oxidase (GOx) to an amperometric electrode for dissolved oxygen (Clark *et al.*, 1962).

Electrochemical sensors can be broadly divided in two classes, biosensors and chemical sensors. According to the international union of pure and applied chemistry (IUPAC) definition (Thévenot *et al.*, 2001): "the electrochemical biosensor is a self-contained integrated device, which is capable of providing specific quantitative or semi quantitative analytical information using a biological recognition element (biochemical receptor) which is retained in direct spatial contact with an electrochemical transduction element". In the literature, however, many authors use a wider definition of biosensors, focused not on the indispensability of a biological recognition element but on the type of analyte. Throughout this review, we will use the term “biosensor” according to the IUPAC convention.

In contrast with biosensors, chemical sensors contain non-biologically active elements, improving their sensitivity and selectivity in analyte detection. In electrochemical sensors, modified electrodes are widely used as sensing elements. These modified electrodes can be formed on the basis of different inorganic or organic materials characterized by good electrical conductivity and catalytic properties.

2.5.2 Working Principle

Electrochemistry implies the transfer of charge from an electrode to another phase, which can be a solid or a liquid sample. During this process, chemical changes take place at the electrodes and the charge is conducted through the bulk of the sample phase. Both the electrode reactions and/or the charge transport can be modulated chemically and serve as the basis of the sensing process (Janata, 2010). Electrochemical sensors are based upon potentiometric, amperometric, or conductivity measurements. The different principles always require a specific design of the electrochemical cell.

The structure of electrochemical sensors is shown in Figure 2.9. Their operating and measurement principles will be summarized in the next sections according to the types listed above.

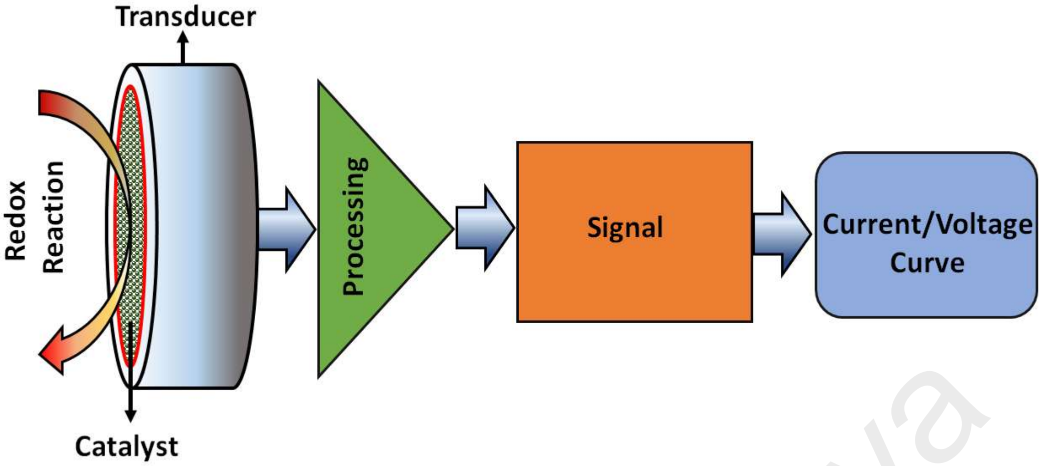

Figure 2.9: Working principle stages of an electrochemical sensor.

2.5.2.1 Potentiometric Sensors

In potentiometric sensors, the potential difference between the reference electrode and the indicator electrode is measured without polarizing the electrochemical cell, that is, very small current is allowed. The reference electrode is required to provide a constant half-cell potential. The indicator electrode develops a variable potential depending on the activity or concentration of a specific analyte in solution. The change in potential is related to concentration in a logarithmic manner. The Nernst equation relates the potential difference at the interface to the activities of species i in sample phases (s) and in the electrode phase (β) (Jackowska *et al.*, 2013).

2.5.2.2 Amperometric Sensor

Amperometry is a method of electrochemical analysis in which the signal of interest is a current that is linearly dependent upon the concentration of the analyte. As certain chemical species are oxidized or reduced (redox reactions) at inert metal electrodes, electrons are transferred from the analyte to the working electrode or to the analyte from the electrode. The direction of flow of electrons depends upon the properties of the analyte and can be controlled by the electric potential applied to the working electrode. Two or three electrodes may comprise an amperometric cell. The working electrode is usually constructed from a metal such as platinum (Pt) or gold (Au). A reference electrode, usually Ag/AgCl, provides a fixed potential against which the potential applied to the working electrode is measured and controlled. A third electrode, the counter (or auxiliary) electrode is sometimes included. Linear current via ion-concentration characteristics can be obtained by amperometry at diffusion controlled processes in the “limiting current operating mode”. The measured cell current (diffusion current) is a quantitative measure of the analyte of interest. Due to the different electron transfer process, there are three so-called “generations” of biosensors: first generation biosensors where the normal product of the reaction diffuses to the transducer and causes the electrical response, second generation biosensors which involve specific “mediators” between the reaction and the transducer in order to generate improved response, and third generation biosensors where the reaction itself causes the response and no product or mediator diffusion is directly involved.

2.5.2.3 Other Electrochemical Sensing Measurements

Conductometric sensors are based on the measurement of electrolyte conductivity, which varies when the cell is exposed to different environments. The sensing effect is based on the change of the number of mobile charge carriers in the electrolyte. If the electrodes are prevented from polarizing, the electrolyte shows ohmic behavior. Conductivity measurements are generally performed with AC supply. The conductivity is a linear function of the ion concentration; therefore, it can be used for sensor applications. However, it is nonspecific for a given ion type. On the other hand, both the polarization and the limiting current operation mode must be avoided. Thus, small amplitude alternating bias is used for the measurements with frequencies where the capacitive coupling is still not determining the impedance measurement.

Coulometry is an electrochemical technique, related to amperometry, where the amount of charge (coulombs) passing between two electrodes is measured. The amount of charge passing between the electrodes is directly proportional to oxidation or reduction of an electroactive substance at one of the electrodes. The number of coulombs transferred in this process is related to the absolute amount of electroactive substance by Faraday's Law.

2.6 Dopamine (DA)

Neurotransmitters are endogenous chemicals that transmit signals across a synapse from one neuron cell to another 'target' cell (Jackowska & Krysinski, 2013). Acting as the chemical messengers of the nervous system, neurotransmitters relay information across synapses via excitation or inhibition of the next neuron or effector tissue (Mele *et al.*, 2010). Neurotransmitters are mainly classified into amino acids, peptides, and monoamines. The amino acids are glutamate, aspartate, D-serine, g-aminobutyric acid, and glycine. The monoamines are histamine, adrenaline, dopamine (DA), noradrenaline, serotonin, and melatonin.

Dopamine [4-(2-aminoethyl) benzene-1, 2-diol] is a monoamine neurotransmitter, which is a key neurotransmitter in neuroscience. It is present in the mammalian central nervous system and participates significantly in the activity of the hormonal, renal, cardiovascular and central nervous systems. In the nervous system, it is responsible for communication of electrical signals between substantia nigra and various brain tissues. Additionally, it also helps to control hormonal balance and emotions. However, the abnormality in dopaminergic neurotransmission system results in various neurological diseases like schizophrenia, (Aurora *et al.*, 2012), Parkinson's disease (Obata, 2002), human immunodeficiency virus (HIV) infection (Ensafi *et al.*, 2009) and Huntington's disease (Watson *et al.*, 2006) . Consequently, quantitative determination of dopamine

(DA) is very important. But various physiological biomolecule coexist with DA in a very high concentration in a biological system. Therefore, quantitative determination with good selectivity of DA is extremely important for the diagnosis and pathological understanding of several neurological diseases. For *ex-vivo* determination of DA, several techniques have been developed including: mass spectrometry (Holdiness *et al.*, 1980), flow injection chemiluminescence fluorescence (Deftereos *et al.*, 1993), surface enhanced Raman scattering (Kaya *et al.*, 2012), chromatography (Zhou *et al.*, 2013) optical absorption spectrophotometry (Mamiński *et al.*, 2005) and micro dialysis . But these analytical techniques suffer from the limitations of expensive instrumentation, large sample volumes, time consuming analysis and use of non-green solvents. On the other hand, electrochemical methods are considered to be the best owing to their superior advantages like low cost, facile operation, high sensitivity with good selectivity, rapid response, reliability and reproducibility (Abdelwahab *et al.*, 2015; Numan *et al.*, 2017). Since DA is a highly electroactive biomolecule, so electrochemical techniques are highly preferred for its quantitative determination.

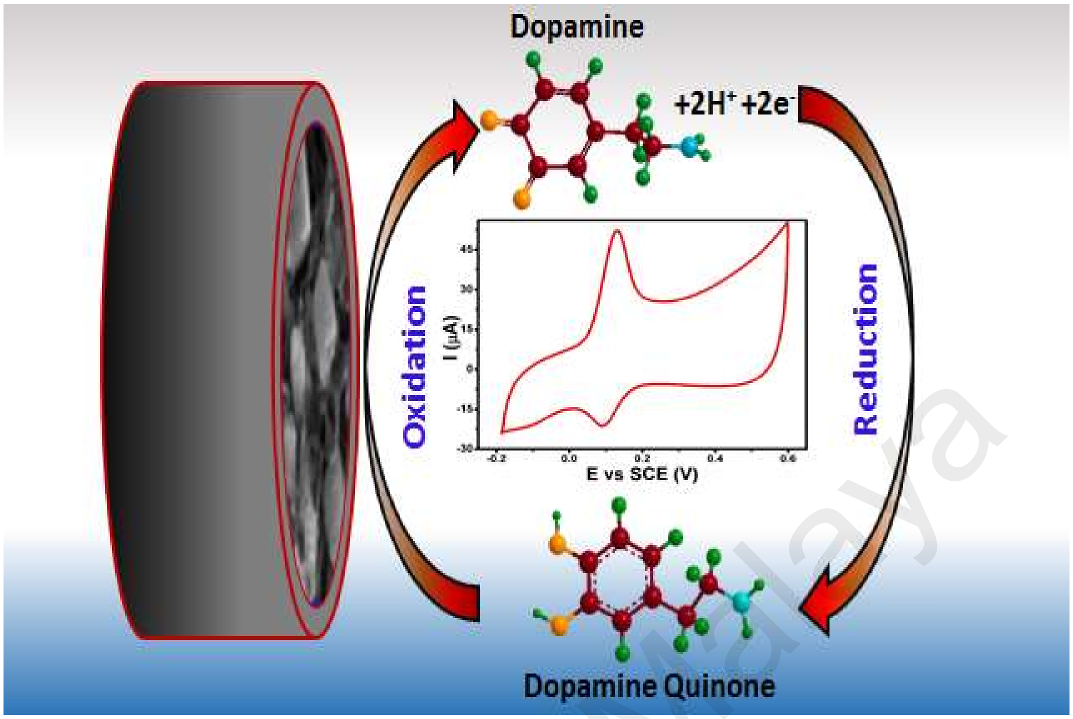

Figure 2.10: Schematic illustration of electroxidation of DA.

The major hindrance in electrochemical methods is the adsorption of oxidation products on the active sites of the electrode during sensing event. Consequently, the reproducibility and reusability of the electrode decreases. Traditional unmodified electrodes are incapable to tackle these problems, which results in a poor performance. However, the surface modification of glassy carbon electrode (GCE) plays significant role in enhancement of the performance of electrode in terms of sensitivity and selectivity (Nazemi *et al.*, 2010). Recently, several materials have been investigated, which include conducting polymer based nanocomposites(Palanisamy *et al.*, 2016) , metal, metal oxide nanoparticles (Liu *et al.*, 2015; Palanisamy *et al.*, 2013) and carbon based nanostructures (Fernandes *et al.*, 2014) for the chemical modification of electrode to enhance the performance of the electrodes.

CHAPTER 3: MATERIALS AND METHODS

3.1 Introduction

This chapter consists of three major parts. In the first part, the description of chemicals used for the synthesis nanocomposites and for the application study are given. The second part is about the detailed explanation of synthesis of GO, rGO−Co_3O_4 nanocube, functionalization of MWCNTs and synthesis of MWCNT−Co_3O_4. The phenomenon of intercalation of Co_3O_4 nanocubes/nanograins in rGO−Co_3O_4 nanocomposite and integration of Co_3O_4 nanocubes with MWCNTs in MWCNT−Co_3O_4 nanocomposite is also discussed in detail. In third and last part, the details of parameters, instrumentation and the analytical methods used for the structural, morphological and electrochemical studies are described.

3.2 Materials

For the synthesis of GO, rGO−Co_3O_4 nanocubes and rGO−Co_3O_4 nanograins, potassium permanganate ($KMnO_4$, > 99 %), sulfuric acid (H_2SO_4 ~ 98 %), hydrochloric acid (HCl ~ 35 %), potassium hydroxide (KOH), N-Methyl-2-pyrrolidone (NMP), phosphoric acid (H_3PO_4 ~ 85 %) and ammonia solution (NH_3, 25 %) were purchased from R & M Chemicals. Graphite flakes and acetylene black were purchased from Asbury Inc. (USA). Cobalt acetate tetrahydrate ($Co(CH_3COO)_2$ $4H_2O$), absolute ethanol (C_2H_6O ~ 99.8 %) and hydrogen peroxide (H_2O_2, 35 %) were obtained from Sigma Aldrich and Merck. The whole experiments were performed using deionized (DI) water.

For the synthesis of MWCNT−Co_3O_4 nanocubes, MWCNTs (outer diameter: 10−15 nm and length: 1 μm) were obtained from Beytube Germany. Uric acid (UA), ascorbic acid (AA), glucose, DA, were purchased from Sigma Aldrich. The chemicals used in the whole investigation were of analytical grade. DI water was used throughout all experiments to prepare the solutions.

3.3 Synthetic Methods

All the nanocomposites were synthesized by one-pot hydrothermal route. The reaction temperature was kept at 150 °C for fixed time of 5 hours. Hydrothermal route was preferred by virtue of its simplicity and choice of tuning various synthesis parameters (pH, temperature, time and concentration of regents or precursors) (Lencka *et al.*, 2000). The appropriate amount of powdered reagents together with solvent can be put in a Teflon-lined autoclave and heated from room to elevated temperature and pressure for a fixed time. The electrolyte thermodynamics allow us to predict optimum reaction conditions (Lencka *et al.*, 2000).

3.3.1 Synthesis of GO

GO was synthesized by simplified Hummer's method (Huang *et al.*, 2011). First, oxidation of graphite was done by adding it in the mixture of H_2SO_4 and H_3PO_4 with volume ratio of 4:1. The entire mixture was kept under constant stirring for 3 days to allow the complete oxidation of graphite. During this period the color of mixture was changed from dark purplish green to dark brown. After this, H_2O_2 was added to stop oxidation reaction. The change of color from dark brown to yellow was indicator of high oxidation degree of oxidation of graphite. This graphite oxide was washed in 12,000 rpm of centrifuge successively with 1 M of HCl and DI water until pH of 4 was achieved. During washing with DI water, the graphite oxide experienced exfoliation which led to the thickening of the graphene solution, forming GO gel.

3.3.2 Synthesis of rGO─Co_3O_4 nanocubes

In a typical synthesis of rGO–Co_3O_4 composite, a freshly prepared 20 mL of exfoliated GO solution (1 mg.mL^{-1}) was added dropwise in 25 mL of ethanol under stirring. A 10 mL of 0.25 mmol $Co(CH_3COO)_2 \cdot 4H_2O$ was added drop by drop into the above solution under vigorous stirring at 60 ºC. Then, 15 mL of ammonia (6 %) solution was added slowly into the above mixture under constant stirring. Subsequently the complete reaction mixture was transferred into a 100 mL Teflon lined stainless steel autoclave and subjected to hydrothermal treatment at 150 °C for 5 hours. Then, the obtained precipitate of rGO–Co_3O_4 nanocomposite was washed with DI water and ethanol several times followed by drying at 90 ºC in a hot air oven. The entire experiment was repeated for the synthesis of rGO–Co_3O_4 composite with other mol ratios (0.5, 0.75 and 1 mmol) of $Co(CH_3COO)_2$ $4H_2O$. These synthesized Co_3O_4 nanocubes/rGO composite with different mol ratios of cobalt precursor 0.25, 0.5, 0.75 and 1 mmol were denoted as A1, A2, A3 and A4, respectively.

3.3.2.1 Formation of rGO─Co_3O_4 nanocubes

A schematic representation of the formation of rGO–Co_3O_4 nanocube was shown in Figure 3.1. The Co_3O_4 intercalated rGO was synthesized via hydrothermal method. In the first step, GO solution (containing functional groups, such as hydroxyl (–OH), epoxy(C–O–C), carboxyl (–COOH) and carbonyl group (C=O)) was sonicated for one hour in order to get exfoliated GO sheets. In the second step, $Co(CH_3COO)_2$ was added in the exfoliated GO solution, which lead to adsorption of Co^{2+} ions on GO due to the electrostatic force of attraction between Co^{2+} ions and oxygen based functional groups resulting in the local creation of bridge as Co–O–C bonding (An *et al.*, 2001; Kumar *et al.*, 2014). In the third step, reaction medium was changed into basic condition with the help of NH_3 solution and followed by hydrothermal process. Upon hydrothermal process, the GO–$Co(OH)_2$ was transformed to rGO–Co_3O_4 nanocubes. Additionally, restacking of rGO sheets was controlled by incorporation of Co_3O_4 nanocube during the reduction of GO to rGO (Wu *et al.*, 2012). Figure 3.1 describes the stepwise formation of rGO-Co_3O_4 nanocubes.

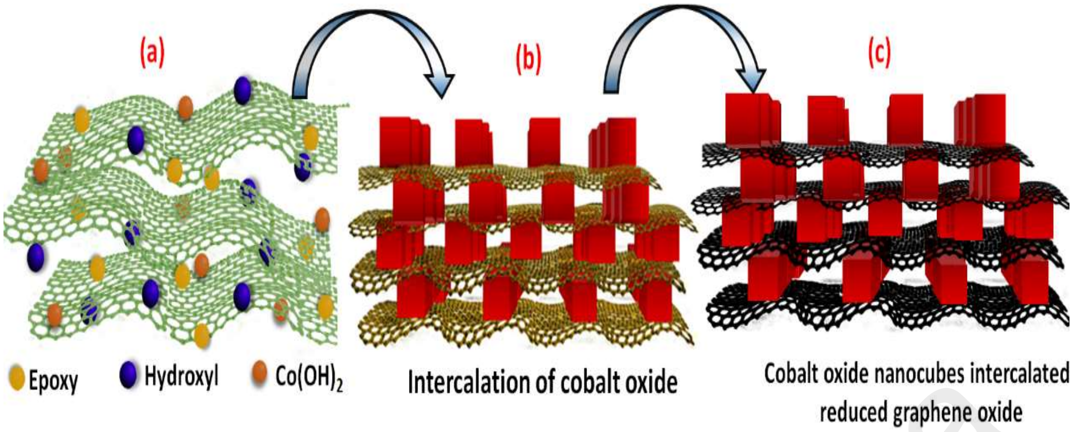

Figure 3.1: Schematic illustration of steps for the formation of rGO–Co_3O_4 nanocubes.

3.3.3 Synthesis of rGO─Co_3O_4 nanograins

The rGO–Co_3O_4 nanograins were synthesized using one-step hydrothermal process. In a typical synthesis of rGO–Co_3O_4 nanograins, the GO was prepared by a simplified Hummer's method. 5.7 wt. % solution of GO (1 mg.mL^{-1}) was sonicated for 15 minutes in order to exfoliate the stacked GO sheets and subsequently added into 15 mL of ethanol under stirring. Subsequently, 10 mL solution of 1 mmol $Co(CH_3COO)_2.4H_2O$ was added dropwise into the mixture and kept under vigorous stirring for 30 minutes until a homogeneous solution was obtained. After that, 15 mL of urea solution (1 mmol) was added drop wise and the mixture was stirred for another 30 minutes. The mixture was then transferred into a 100 mL Teflon-lined stainless steel autoclave and kept in the preheated oven at 150 °C for 5 hours. Finally, the obtained precipitate of rGO–Co_3O_4 nanograins was washed several times with DI water and ethanol by centrifugation and dried at 60 °C in a hot air oven. The entire experiment was repeated in the absence of GO to synthesize pure Co_3O_4 nanograins and with the presence of different contents of GO (7.4, 9.1 and 10.7 wt. %,) to synthesize rGO–Co_3O_4 nanocomposites. The rGO–Co_3O_4 nanocomposites with GO contents of 5.7, 7.4, 9.1 and 10.7 wt. % were denoted as B1, B2, B3 and B4, respectively.

3.3.3.1 Formation of rGO─Co_3O_4 nanograins

The rGO–Co_3O_4 nanograins were synthesized via hydrothermal route which is an effective approach to grow homogeneous and crystalline particles of metal oxides on the graphene sheets (Liang *et al.*, 2011; Wang *et al.*, 2010). The mechanism for the formation of the rGO–Co_3O_4 nanograins (Figure 3.2) can be divided in to three stages. In the first stage, GO solution (1 mg.mL^{-1}) was added dropwise into the mixture of water and ethanol to obtain exfoliated GO solution. In the second stage, $Co(CH_3COO)_2$ solution containing Co^{2+} was added into the exfoliated GO solution. The Co^{2+} initially coordinated with oxygen containing functional groups on GO sheets due to the electrostatic attraction. Later these sites of functional groups served for nucleation. Recent studies reported that for proper nucleation of metal oxide/hydroxide nanoparticles, optimization of the water contents in the reaction solution is important. Low water contents can effectively reduce the independent solution phase growth of nanoparticles by controlling the hydrolyzation process (Park *et al.*, 2009; Wang *et al.*, 2010). Thus low water contents were used in reaction solution in order to decrease the hydrolyzation of Co^{2+}. This has led to an effective increase in the nucleation of cobalt hydroxide on graphene sheets, which helped in selective growth and better dispersion of Co_3O_4 nanograins on graphene sheet (Wang *et al.*, 2010; Wang *et al.*, 2010). In the last stage, reaction medium was transformed into basic condition by the addition of urea solution and transferred in Teflon lined stainless steel autoclave for hydrothermal reaction. During hydrothermal reaction (at high temperature and pressure), GO behaved as an oxidizing agent, oxidized Co^{2+} to Co_3O_4 precipitate, while itself reduced to rGO. This resulted in the uniform growth of Co_3O_4 nanoparticles on the 2D graphene matrix.

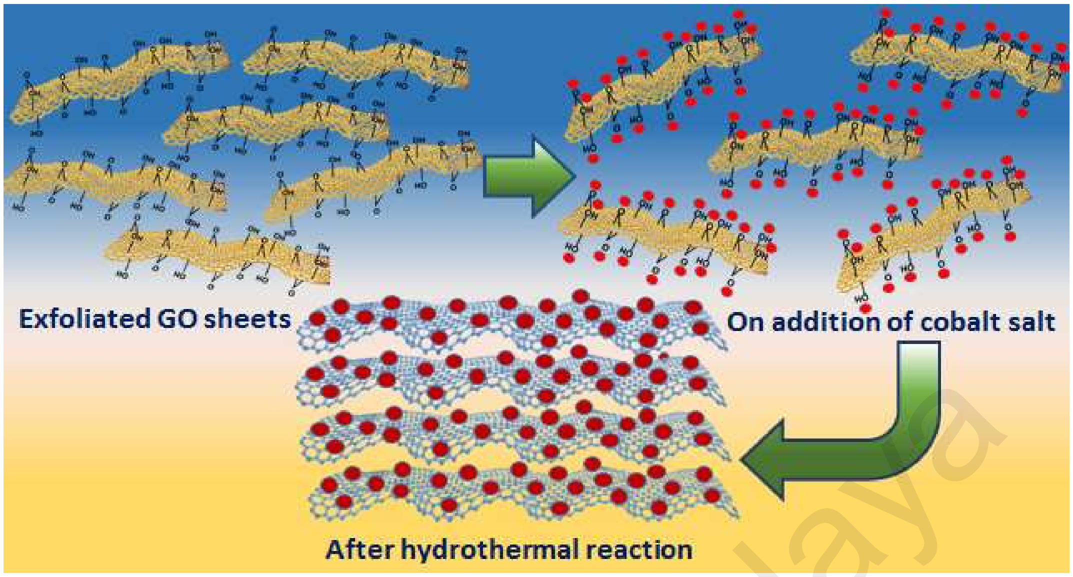

Figure 3.2: Schematic formation mechanism of rGO–Co_3O_4 nanograins.

3.3.4 Functionalization of MWCNTs

Before synthesis, MWCNTs were functionalized by acid treatment. Appropriate amount of MWCNTs powder was added in a mixture of 3:1 sulphuric/nitric acid (V:V) and stirred using magnetic stirrer for 1 hour. Then, the mixture was sonicated for 6 hours at room temperature followed by washing with DI water until pH reached to 7. The treated MWCNTs were dried overnight at 50 °C in a vacuum oven. The acid treatment of MWCNTs was done in order to increase their dispersion in water by functionalizing them with electronegative functional groups and removal of amorphous carbon as well as metal residue (Datsyuk *et al.*, 2008).

3.3.5 Synthesis of MWCNT─Co_3O_4 nanocubes

MWCNT−Co_3O_4 nanocubes were synthesized by single step hydrothermal reaction. In typical synthesis, 1 mmol of Co $(CH_3COO)_2$ $4H_2O$ was dissolved in 45 mL of DI water. Then, 15 mL of ammonia (6 %) was added dropwise with a rate of 1 $mL.min^{-1}$ in the above solution and the mixture was kept under vigorous stirring for 1 hour. Then, a solution containing MWCNTs (4 wt. % (10 mg) in 15 mL) was added in above mixture under bath sonication for 15 min and the resultant mixture was sealed in a stainless steel autoclave followed by hydrothermal reaction for 5 hours at 150 °C. Finally, the precipitate of MWCNT─Co_3O_4 nanocubes was washed several times with DI water and ethanol by centrifugation and dried at 60 °C in a hot air oven. Same experiments were repeated for the synthesis of Co_3O_4 nanocubes, C2, C3, C4 and C5 by using 0, 8 (20 mg), 12 (30 mg), 16 (40 mg), and 20 wt. % (50 mg) of MWCNTs, respectively.

3.3.5.1 Integration of MWCNT─Co_3O_4 nanocubes

For the integration of metal oxide nanoparticles with MWCNTs, it is highly imperative that MWCNTs should be functionalized with electronegative functional groups. These functional groups provide anchoring sites for the uniform growth of nanoparticles over the tabular surface MWCNTs. In present case, the integration of Co_3O_4 nanocubes with MWCNTs can be explained in three stages. In first stage, $Co(CH_3COO)_2.4H_2O$ was dissolved in DI water and NH_3 was added subsequently. The cobalt ions and NH_3 produced cobalt hexammine complex ($[Co(NH_3)_6]^{2+}$) (Sankapal *et al.*, 2015). In second stage, MWCNTs were dispersed in DI water using bath sonicator and the above cationic solution ($[Co(NH_3)_6]^{2+}$) was added in the mixture of dispersed MWCNTs and DI water. The complexed cobalt ions ($[Co(NH_3)_6]^{2+}$) adsorbed on the surface of MWCNTs due to cohesive/van der Waal's/chemical attractive forces between cobalt hexmmine (electropositive) complex and electronegative functional groups on MWCNTs. So the electronegative functional groups initially provided nucleation sites for the uniform growth Co_3O_4 nanocubes. Finally, the mixture was transferred into 100 mL of Teflon lined stainless steel autoclave and kept at 150 °C for 5 hours. During hydrothermal reaction $[Co(NH_3)_6]^{2+}$ was transformed into Co_3O_4 nanocubes. At the same time electronegative functional groups were removed leading to the bundling of MWCNTs, which result in wrapping of Co_3O_4 nanocubes by MWCNTs.

3.4 Characterization Techniques

3.4.1 Structural and Morphological Characterization Techniques

A JEOL JSM-7600F field emission scattering electron microscopy (FESEM) fitted with energy dispersive X-ray (EDX) and elemental mapping was employed to analyze the surface morphology and elemental mapping together with the EDX spectrum. High resolution transmission electron microscopy (HRTEM) micro images were taken by JEOL JEM-2100F in order to determine particle size distributions. Raman spectra were recorded using the Renishaw inVia 2000 system green laser emitting at 514 nm. The structural crystallinity of MWCNT–Co_3O_4 nanocomposites was studied using Philips X'pert X-ray diffractometer (XRD) with copper K_α radiation (λ = 1.5418 nm) at a scan rate of 0.02 degree per second. The surface chemistry and the composition of prepared composite was studied by X-ray photoelectron spectroscopy (XPS) analysis by using PHI 5000 Versa Probe Scanning ESCA Microprobe (PHI 5000 Versa Probe II, USA), fitted with monochromatic Al-K_α ($h\nu$ = 1486.6 eV) X-ray source.

3.4.2 Electrochemical Characterizations

3.4.2.1 Electrochemical Performance Studies for Supercapacitor

(a) Electrode Preparation

The working electrode was fabricated by mixing of electroactive materials, polyvinylidene fluoride (PVDF) and carbon black with mass percentage ratio of 75:15:10 in 1-methyl-2-pyrrolidone (NMP) medium under ultrasonication. The viscous slurry was subsequently drop-casted and compressed on nickel foam (area of 1 cm^2). The loaded mass of active materials (rGO−Co_3O_4 nanocubes and MWCNT−Co_3O_4 nanocubes) on working electrodes without carbon black and PVDF was ~5 mg.

(b) Supercapacitor Cell Fabrication

The working electrodes were immersed in 1 M KOH aqueous solution for 2 hours before taking the electrochemical measurements. All the electrochemical measurements were carried out in a standard three-electrode cell system. The active materials coated Ni foam used as the working electrodes, platinum wire as the counter electrode and silver/silver chloride (Ag/AgCl) as the reference electrode in a 1 M KOH aqueous solution at room temperature. Cyclic voltammetry (CV), electrochemical impedance spectroscopy (EIS) and galvanostatic charge discharge (GCD) were performed with a Gamry (Reference 3000 instrument). The CV measurements in three electrode cell system were performed in the potential range of 0 to 0.55 V at different scan rates of 1, 3, 5, 10, 20, 30, 40 and 50 mVs^{-1}. Electrochemical impedance spectroscopy (EIS) measurements were recorded in a frequency range from 0.01 Hz to 100 kHz under AC amplitude of 5 mV at open circuit voltage.

3.4.2.2 Electrochemical Performance Studies for Sensor

(a) Modification of GCE

The surface of GCE was modified by dissolving catalyst powder in DI water (1 mg.mL^{-1}) and drop coating 5 µL of the catalyst ink on the surface of GCE (diameter = 3 mm) which was subsequently dried at room temperature for 1 hour. Prior to every modification, GCE was cleaned electrochemically by potential cycling in 0.5 M H_2SO_4 using potential window between -1 to +1 V, followed by polishing with 1.0 µM and 0.3 µM alumina slurry. Phosphate buffer with neutral pH (7.2) was used as an electrolyte.

(b) Real Time Urine Sample Preparation

In order to evaluate the performance of the synthesized nanocomposites, analytical determination of DA in two urine samples was performed using the standard addition method. For this, two fresh urine samples from two healthy males were chosen as biological samples. The collected samples were filtered and stored at 4 °C immediately after collection. For further measurements, these samples were diluted 50 folds in 0.1 M phosphate buffer (pH ~ 7.2).

(c) Sensor Studies

Electrochemical measurements were carried out on multi-channel Autolab (PGSTAT30) potentiostat workstation with conventional three electrode configuration. The nanocomposite modified GCE served as a working electrode, Ag/AgCl (3 M KCl) and platinum wire were used as reference and counter electrodes respectively. Phosphate buffer with neutral pH (7.2) was used as an electrolyte. CV was run in a potential range from 0.2 to 0.6 V at different scan rate and different concentration of analyte. Chronoamperometry (CA) was performed to calculate the limit of detection. The CA responses of the nanocomposites modified GCE were recorded on the successive injections of 1 μM of DA in a homogeneously stirred solution of 0.1 M phosphate buffer at a fixed time interval of 60 s.

CHAPTER 4: RESULTS AND DISCUSSION

4.1 Introduction

This chapter is based on complete morphological, structural and compositional characterizations of the prepared systems. The electrochemical performances of all the synthesized nanocomposites for supercapacitor and electrochemical sensor are discussed in detail. This chapter has been divided into three parts. In the first part, the characterizations of rGO–Co_3O_4 nanocubes and their application towards supercapacitor are discussed. In second part, the detailed characterization results of rGO–Co_3O_4 nanograins and their performance towards electrochemical detection of DA are explained. In the third and final part of this chapter, brief structural, morphological and compositional results of MWCNT–Co_3O_4 nanocubes and their electrochemical application towards supercapacitor and sensor are discussed.

4.2 Structural, Morphological and Electrochemical Characterizations of rGO–Co_3O_4 nanocubes[1]

4.2.1 Structural and Morphological Characterizations

4.2.1.1 X-ray Diffraction (XRD)

The crystalline structures of synthesized GO, rGO, Co_3O_4, and rGO–Co_3O_4 were studied by recording the XRD patterns (Figure 4.1). GO (Figure 4.1(a)) showed a sharp intensity peak at 2θ value of 10° corresponding to (001) plane (Shahid *et al.*, 2014). The sharpness of peak indicated that the larger interlayer distance due to the presence of

---

[1] **Section 4.2 of this chapter is published as:** Numan, A., Duriasamy, N., Omar, F. S., Mahipal, Y. K., Ramesh, K., & Ramesh, S. (2016). Enhanced electrochemical performance of cobalt oxide nanocube intercalated reduced graphene oxide for supercapacitor application. *RSC Advances*, 6, 34894–34902.

functional groups on graphene basal plane (Wu *et al.*, 2012). Under the hydrothermal process, the diffraction peak of GO at 2*θ* value of 10° disappeared and two new, broader peaks were generated at 2*θ* values of 26.8° and 42.7° correspond to (002) and (100) planes of rGO (Figure 4.1(b)) respectively (Shahid *et al.*, 2014). The peak at 14° in Figure 4.1(b) came from the sample holder.

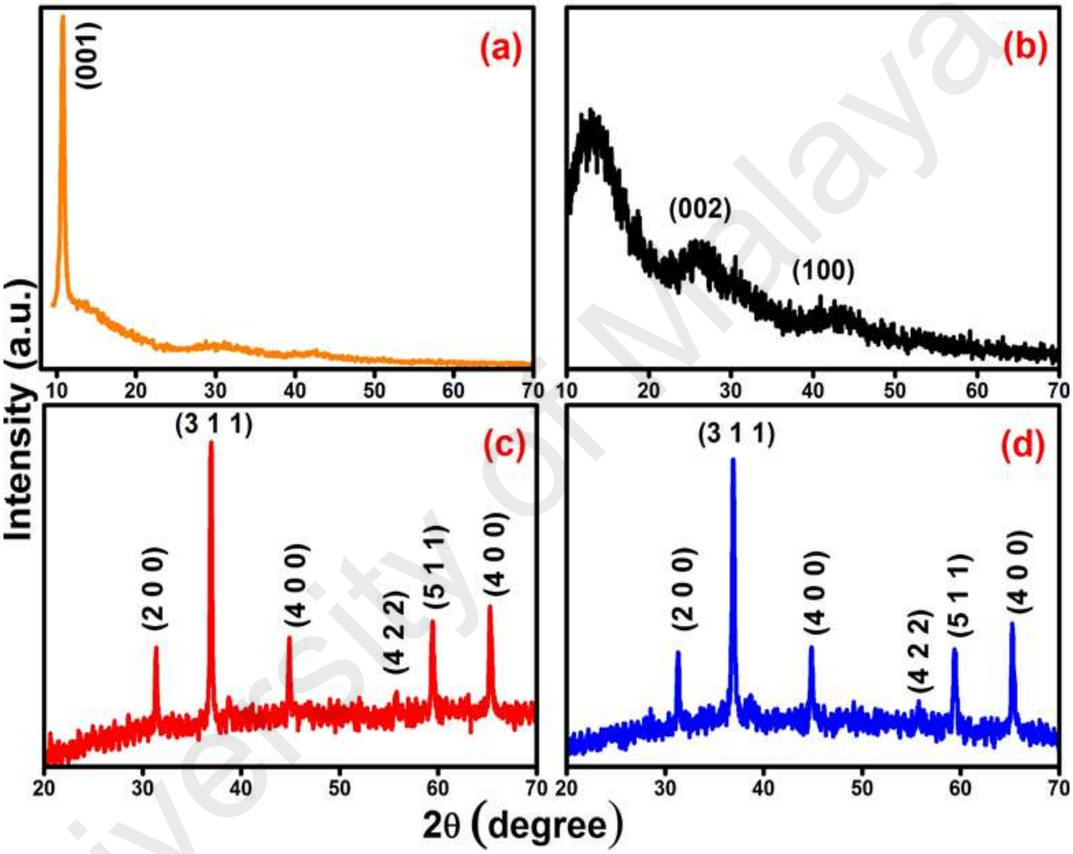

Figure 4.1: XRD patterns (a) GO, (b) rGO, (c) Co_3O_4 and (d) rGO–Co_3O_4 nanocomposite.

The observed two diffraction peaks revealed the disorderedly stacked graphene sheets, which indicate the efficient transformation from GO to rGO (Chen *et al.*, 2012). Figure. 4.1(c-d) exhibited the XRD patterns of pure Co_3O_4 and rGO–Co_3O_4 composite. The diffraction pattern of pure Co_3O_4 exhibited a strong crystalline peaks at 2*θ* = 31.2°, 36.8°, 44.7°, 55.5°, 59.2°, and 65.1° corresponds to (220), (311), (400), (422), (511), and (440) planes of a face cantered cubic structure of Co_3O_4 (JCPDS card No. 42-1467). The rGO–Co_3O_4 nanocube showed the diffraction peaks of Co_3O_4, which was intercalated with rGO matrix. No other characteristic peaks were observed, suggesting the high purity of Co_3O_4 embedded rGO matrix (Wu *et al.*, 2010).

4.2.1.2 Raman Spectroscopy

Raman spectroscopy is highly suitable and non-destructive tool to monitor the functional groups and structural defects in materials especially carbon based materials such as graphene/GO/rGO and CNTs. Figure 4.2 represented the Raman spectra of GO, rGO and Co_3O_4–rGO composite. The spectra of GO and rGO (Figure 4.2(a-b)) exhibited the well referred *D* and *G* band at 1355 cm^{-1} and 1588 cm^{-1}, respectively. The *D* is band ascribed to the lattice defect induced phonon mode. The *G* bands corresponds to the in plane vibrations of C–C atoms and a doubly degenerated phonon mode (E_{2g} symmetry) at the Brillouin zone center (Li *et al.*, 2014; Naumenko *et al.*, 2012). In general, there was a slight increase in the I_D/I_G ratio from 0.95 to 1.36, suggesting the formation of partially ordered crystal structures and decreased size of in-plane sp^2 domains during the reduction of GO to rGO (Naumenko *et al.*, 2012). However, in rGO–Co_3O_4 hybrid, the I_D/I_G ratio was decreased to 0.90, because of decreasing the sp^2 domain size of carbon atoms and the reduction of sp^3 to sp^2 carbon (Kim *et al.*, 2014). Additionally, the defects were observed in rGO matrix due to the removal of functional groups from GO layers (An *et al.*, 2001). This confirmed the successful reduction of GO to rGO. The *2D* band or second order zone boundary phonon was extremely important to differentiate between monolayer and multilayer sheets in graphene based material. Here, the *2D* band observed at 2901 cm^{-1} in GO, which was retained at the same position in rGO–Co_3O_4 composite (Figure 4.2(d)) respectively (How *et al.*, 2014). The inset Figure 4.2(d) showed the four intensity peaks at ~194, 482, 525, 615, and 686 cm^{-1} correspond to the B_{1g}, E_g, F_{2g}, F_{2g}, and A_{1g} modes of Co_3O_4 respectively.

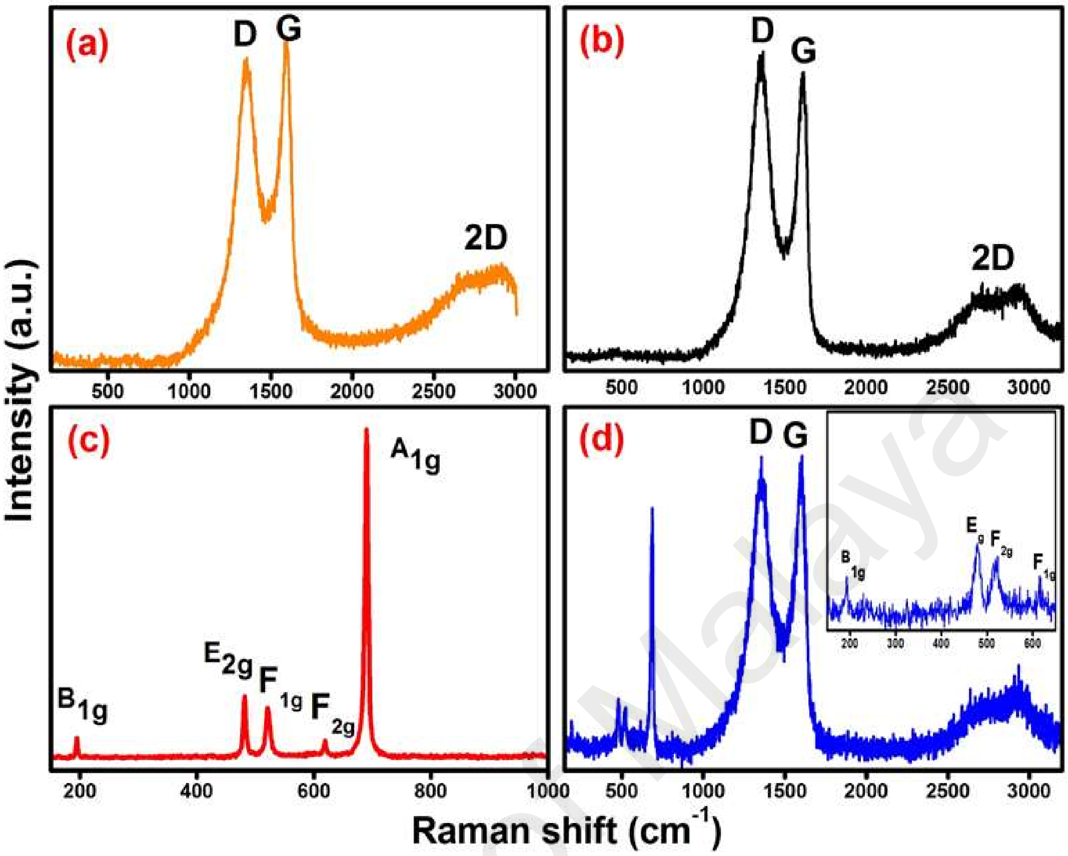

Figure 4.2: Raman spectra for (a) GO, (b) rGO, (c) Co_3O_4 and (d) rGO–Co_3O_4 composite.

4.2.1.3 Field Emission Scanning Electron Microscopy (FESEM)

The surface morphologies of synthesized pure Co_3O_4 and rGO–Co_3O_4 nanocube composites were investigated via FESEM and HRTEM analyses. Figure 4.3(a) showed clear distinction between pure cobalt oxide (inset: Figure 4.3(a)) and composite of cobalt oxide with rGO matrix (A2). The FESEM image (inset: Figure 4.3(a)) revealed the cubical surface morphology of Co_3O_4 with high particles aggregation, which led to reduce in the electrochemical surface area. This can be overcome by introducing rGO matrix as shown in Figure 4.3(b). The rGO matrix provided a platform to anchor cobalt oxide nanocubes, which were well distributed and intercalated with rGO sheets (A2 composite). However, in case of A3 and A4 composite exhibited Co_3O_4 aggregation on rGO matrix due to high concentration of cobalt precursor. The particles aggregations were increased with increasing concentration of cobalt precursor, which was clearly shown in Figure

4.3(c-d). The FESEM results clearly indicated that the low contents of Co_3O_4 with respect to rGO (in A1) led to decrease in the number of Co_3O_4 nanocubes exposed on the top layer of rGO. However, by increasing the contents of Co_3O_4, the number of exposed Co_3O_4 nanocubes over rGO sheets also get increased (A2). But at significantly higher contents of Co_3O_4 (in A3 and A4), particle aggregations became dominant resulting in decrease in electrochemical surface area. In addition, it is also evident that the variations in Co_3O_4 precursor did not affect the particle size and morphology of Co_3O_4.

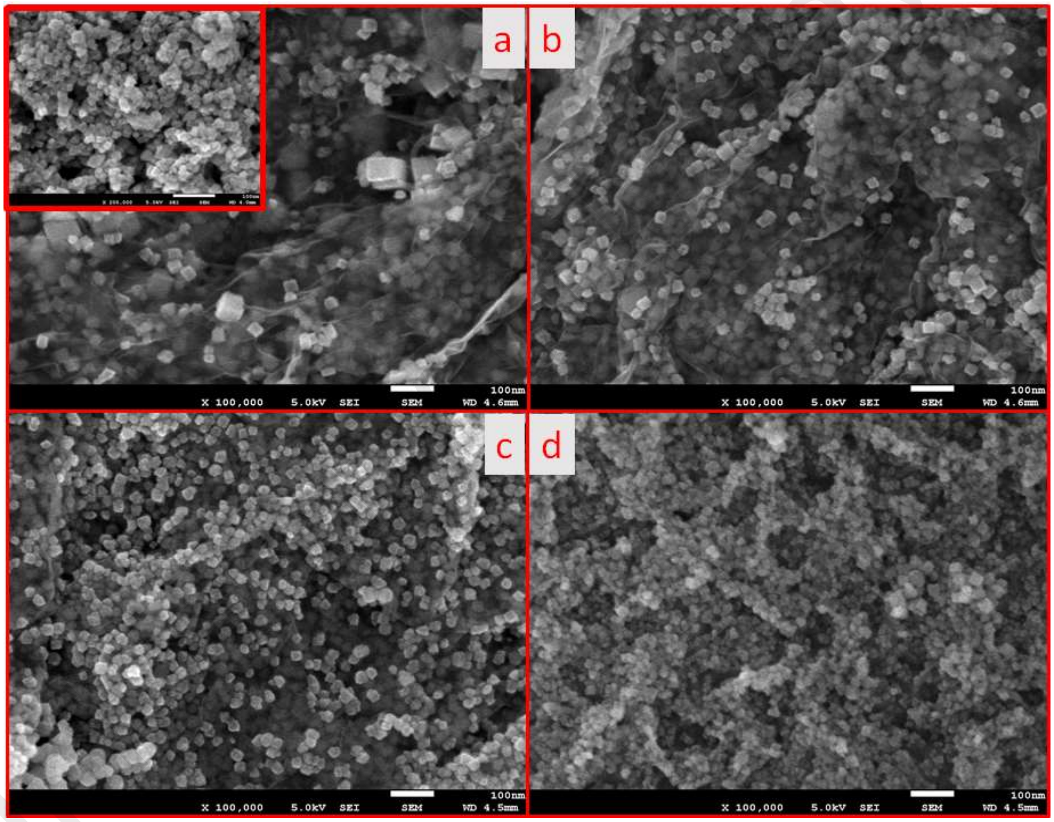

Figure 4.3: FESEM images of (a) A1 (inset: pure Co_3O_4), (b) A2, (c) A3 and (d) A4.

4.2.1.4 High Resolution Transmission Electron Microscopy (HRTEM)

In order to further investigate the morphology and the particle size of Co_3O_4 nanocubes, HRTEM images were taken. Figure 4.4 showed the HRTEM images of pure Co_3O_4 and rGO–Co_3O_4 composite (A2). Figure. 4.4(a) exhibited the cubical shape of pure Co_3O_4 with average particle size of ~ 45 nm. The inset of figure 4.3(a) shows the lattice spacing of 0.40 nm corresponding to the (111) at 2θ value of 19°. The cubical shape of Co_3O_4 was well distributed on transparent rGO matrix (Figure 4.4(b)) without effecting its cubic morphology. This result suggested that the rGO matrix provides a platform for improved electrochemical performance than that of pure Co_3O_4 due to effective intercalation and less particle aggregation of Co_3O_4 on rGO matrix, respectively.

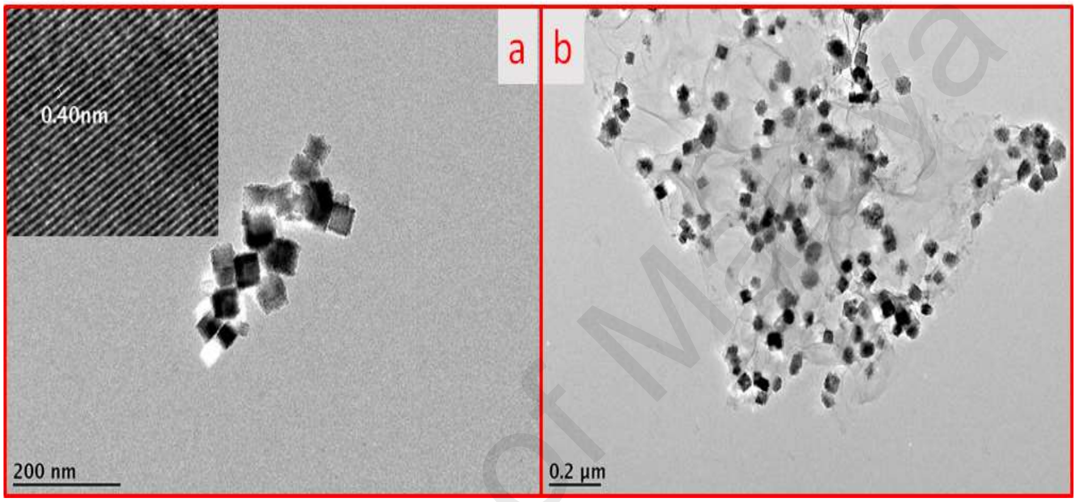

Figure 4.4: HRTEM images of (a) pure Co_3O_4 (inset: lattice fringes) and (b) rGO–Co_3O_4 composite (A2).

4.2.2 Electrochemical Performance Study of rGO─Co_3O_4 nanocubes for Supercapacitor

4.2.2.1 Cyclic Voltammetry

The electrochemical performance of pure Co_3O_4 and rGO–Co_3O_4 nanocubes based electrodes was evaluated for supercapacitor using CV analysis. Cyclic voltammograms were performed for A1, A2, A3 and A4 with potential window from 0 to + 0.55 V at various scan rates. The measured currents were normalized with the mass loading of active material on electrode.

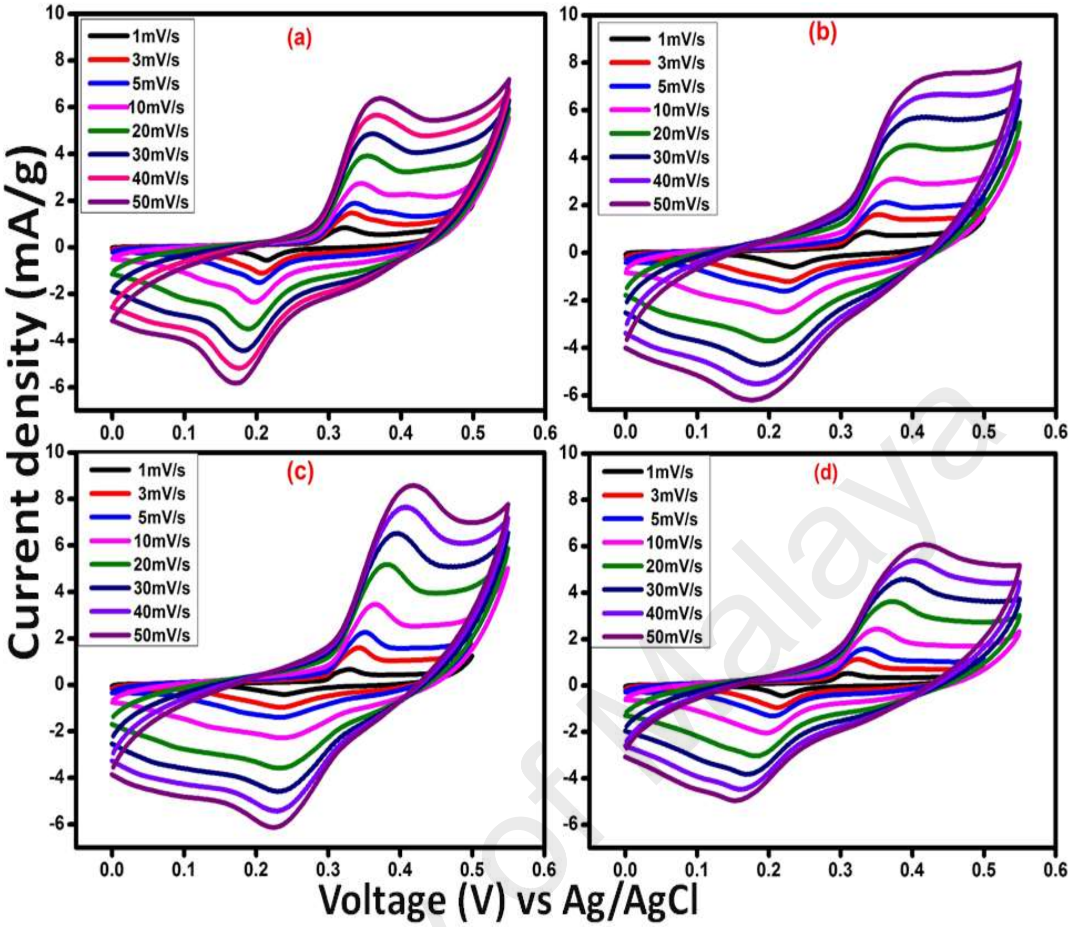

Figure 4.5: CV curves of (a) A1, (b) A2, (c) A3 and (d) A4 electrodes at different scan rates in 1 M KOH electrolyte.

Figure 4.5(a-d) showed the CV curves of A1, A2, A3, and A4 at different scan rates. Herein, the well-defined redox peaks showed the faradic behavior of battery type electrode material, which was due to the interaction of hydroxyl ions with respective electrode (Omar *et al.*, 2017). While increasing the scan rates, redox peak intensities increase with a slight peak shift towards higher potential, which was evidence of faster redox reaction rate occurring at the interface between the active material and electrolyte (Duraisamy *et al.*, 2015). Generally, the rate capability is mainly dependent on three processes such as (i) the diffusion of electrolyte ions, (ii) the adsorption of ions on the electrode surface and (iii) the charge transfer in the electrode. However, any of these processes were relatively slow at higher scan rate, which lead to reduce the specific capacity (Li *et al.*, 2011). In addition to this, the characteristic shape of the CV curve was not significantly changed, which was indicating that rGO–Co_3O_4 composites have an outstanding rate capability (Wang *et al.*, 2011).

The charge storage mechanism of Co_3O_4 for a faradaic battery type electrode in alkaline medium was based on simple OH^- entering reaction, which was described in the following equation (Xu *et al.*, 2010):

$$Co_3O_4 + OH^- + H_2O \xleftrightarrow{\text{Charge/Discharge}} 3\,CoOOH + e^- \tag{4.1}$$

The CV curves of pure Co_3O_4 nanocubes at different scan rates are depicted in Figure 4.6(a). It showed that the well redox peaks were not observed, which can be due to the high aggregation of Co_3O_4 nanocubes, resulting to reduce the active electrochemical surface area. In addition to this, with increasing scan rates, the cathodic and anodic peaks were rapidly shifted to the low and high potentials respectively. This was mainly due to the insufficient diffusion time for OH^- to interact with respective electrode at higher scan rates (Subramanian *et al.*, 2005; Xu *et al.*, 2008). However, in the case of composites (rGO–Co_3O_4 nanocubes), rGO matrix provided highly conductive platform for the Co_3O_4 nanocubes due to the uniform dispersion and intercalation of nanocubes on rGO matrix. This led to an increase of the electrochemical surface areas via augmenting the electroactive sites of Co_3O_4 nanocubes on rGO matrix.

The comparison CV results of A1, A2, A3 and A4 rGO–Co_3O_4 at the scan rate of 10 mVs^{-1} are shown in Figure 4.6(b), suggesting that the A2 has well-defined redox peaks with maximum peak current at lower potential than that of its counterparts. Therefore, this confirmed that the A2 was the optimized composite due to its less particle aggregations (as confirmed by FESEM).

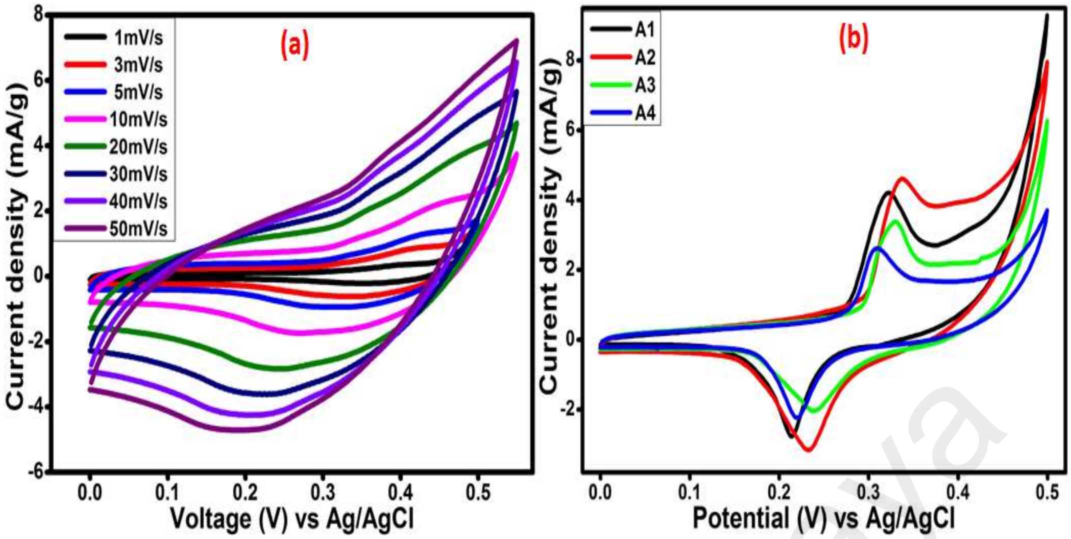

Figure 4.6: CV curves of (a) Co_3O_4 nanocubes at different scan rate, (b) CVs of A1, A2, A3, and A4 at a scan rate of 10 mVs^{-1} in 1 M KOH.

4.2.2.2 Galvanostatic Charge Discharge

The cyclic stability of Co_3O_4 decorated rGO matrix was examined by GCD analysis. Figure 4.7 shows the GCD curve of rGO–Co_3O_4 composite electrodes at various current densities (from 200 to 500 mAg^{-1}) under potential range from 0 to 0.45 V (vs Ag/AgCl). The specific capacity (Q_S) can be calculated by the following equation:

$$Q_S = \frac{I \times \Delta t}{m} \tag{4.2}$$

where "I" is the discharge current (A), "t" is the discharge time (s) and "m" is the mass of active material (g). The obtained specific capacity of 97.2, 125, 61 and 55.3 Cg^{-1} corresponds to A1, A2, A3 and A4 at a current density of 200 mAg^{-1}, respectively.

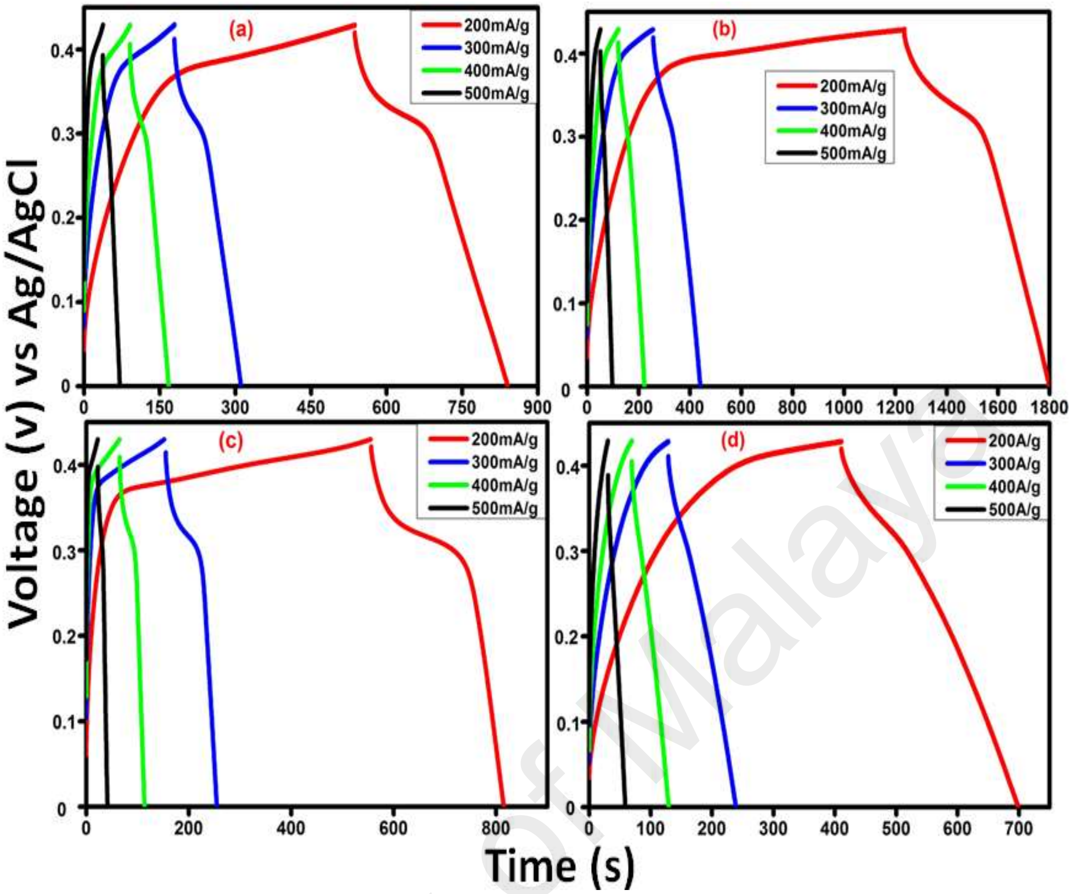

Figure 4.6: GCD curves for (a) A1, (b) A2, (c) A3 and (d) A4.

Figure 4.7(a) revealed that the *Qs* value was varied with respect to molar concentration of cobalt oxide precursor. It confirmed that the lowest specific capacity was observed in pure cobalt oxide, which was due to the high aggregation of Co_3O_4 nanocubes, resulting in the poor electrochemical performance. While introducing rGO, the specific capacity was significantly increased from 53 to 97.2 Cg^{-1} (A1) as shown Figure 4.7(a). The improved specific capacity was owing to high dispersion and the intercalation of Co_3O_4 on rGO matrix. Further increasing the molar concentration of cobalt precursor, the specific capacity tend to attain the maximum value of 125 Cg^{-1} (A2). However, beyond this addition of cobalt concentrations, the specific capacity turned to decrease (A3 and A4) due to the aggregation of Co_3O_4 nanocubes on rGO, resulting to limit the OH^- ions diffusion into the electrode surface. It was evident that the A2 showed the maximum specific capacity of 125 Cg^{-1}. Figure 4.7(b) revealed the specific capacity vs. current density plot. The values of specific capacity was decreased with increasing current density. This was due to the asynchronous movement of electric charges with respect to current rates. At higher current densities, the diffusion/migration of charges through the electrodes was very slow (Duraisamy *et al.*, 2016).

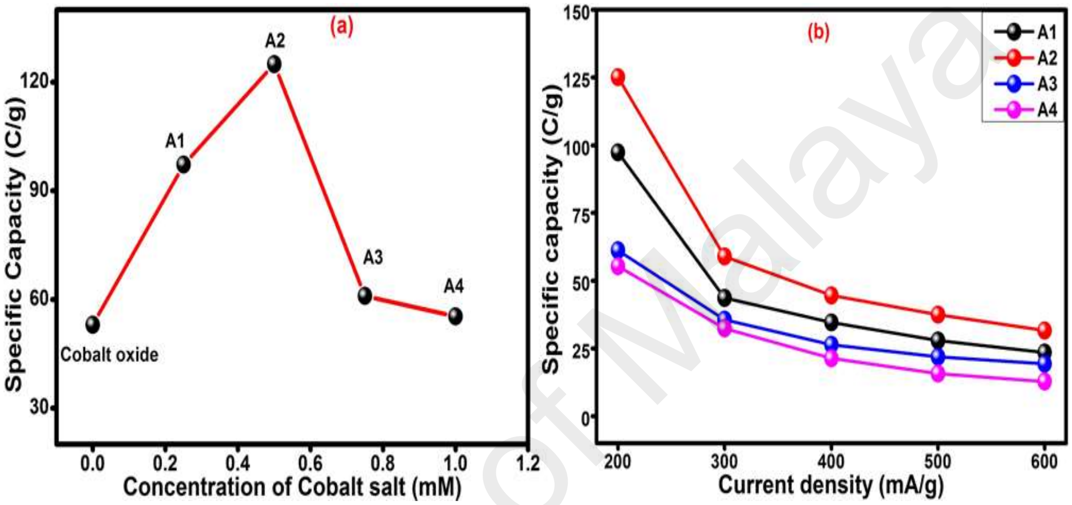

Figure 4.7: (a) Comparison of specific capacity with respect to molar concentration of Co_3O_4 precursor for A1, A2, A3 and A4 (b) Variation in specific capacity at different current densities for A1, A2, A3 and A4.

4.2.2.3 Electrochemical Impedance Spectroscopy

To further elucidate the origin of high electrochemical performance, EIS was carried out to examine the conductivity of the rGO–Co_3O_4 composites. The equivalent series resistance (ESR) could be obtained from the intersection point of the curves with the axis of real impedance. The difference in the ESR of electrodes attributes to the different conductance of electrode materials. ESR of the A1, A2, A3, and A4 electrodes (Figure 4.8(a)) was found to be 1.25, 1.3, 1.37 and 1.57 **Ω**, respectively. The ESR of rGO–Co_3O_4 composites was increased with increasing cobalt precursor concentrations, indicating poor conductivity of material at high molar concentration. This is due to the aggregation of cobalt oxide and weak interaction of Co_3O_4 with rGO matrix. At high frequency region, the observed larger semicircle indicated poor electrical conductivity due to high interfacial charge transfer resistance (Pendashteh *et al.*, 2013). Nyquist plots of the composite with lower molar concentration of cobalt precursor revealed the smaller diameter of semicircle as compared with higher concentration, resulting the lower charge transfer resistance.

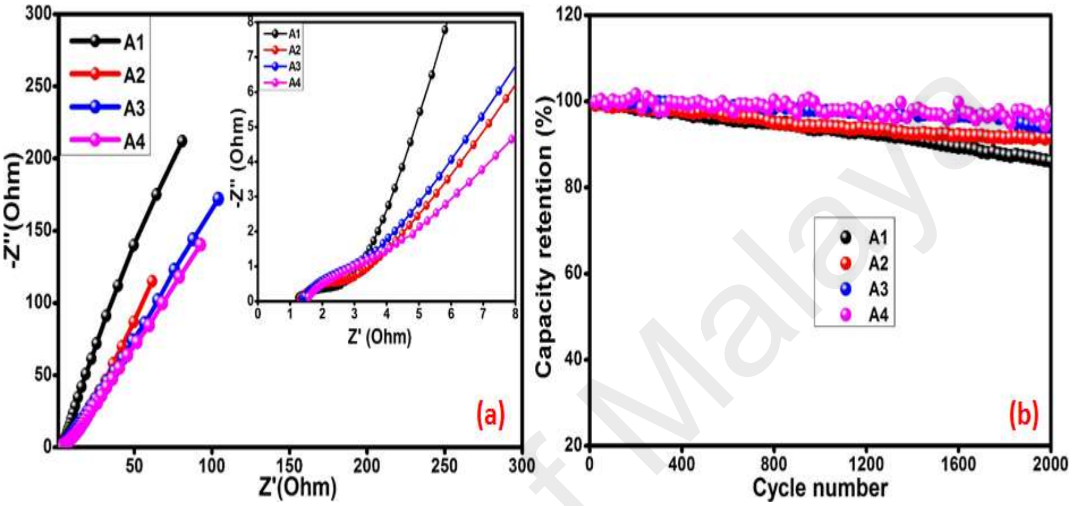

Figure 4.8: (a) EIS spectra of A1, A2, A3 and A4, (b) Life cycle test of A1, A2, A3 and A4.

Long term cycling stability test was a key factor to evaluate the stability of electrodes for practical applications. The long term cycling performance over 2000 cycles of electrode materials was carried out by repeating the charge/discharge test at a current density of 3 Ag^{-1}. The cyclic stability of A1, A2, A3 and A4 corresponds to 86, 91.6, 94 and 97.5 % of capacity retention with respect to initial value (Figure 4.8(b)) respectively. These results confirmed that the cyclic stability was increased with increasing the molar concentration of cobalt precursor.

However, the specific capacity was decreased beyond some limitation of molar concentration due to the particle aggregation. The maximum specific capacity (125 Cg^{-1}) with longer cyclic stability (91.6 % after 2000 cycles) was observed at A2 as compared with other electrodes. Therefore, these results indicate that the A2 is a promising candidate for high performance energy storage systems.

4.2.2.4 Asymmetric Supercapacitor Studies

(a) Cyclic Voltammetry

In order to investigate the complete device performance, asymmetric supercapacitor was fabricated by using rGO–Co_3O_4 nanocubes (A2) as battery type positive electrode, while AC as a negative electrode as shown in Figure 4.9(a). The increase in the operation potential window is one of the key factor that can significantly enhance the energy density of real supercapacitor. Therefore, prior to asymmetric supercapacitor assembly, CVs of AC based electrode and rGO–Co_3O_4 nanocubes based electrode were recorded in three electrode cell system in order to determine the maximum operational potential (Figure 4.9(b)). Figure 4.9(c) shows the CV curve of rGO–Co_3O_4 nanocubes//AC supercapacitor and it reveals that quasi CV curve can be obtained up to the maximum voltage of 1.55 V. Beyond this voltage CV curve cannot maintain its stable rectangular shape (Figure 4.9(c)). In addition, no redox peaks were observed at potential window of 0-0.4 V, however redox peaks appeared upon extending the potential window until 1.55 V, manifesting that capacity of the device was also contributed from the faradaic reaction. Figure 4.9(d) shows the CV of curves of the asymmetric supercapacitor at various scan rates. It is evident from Figure 4.9(d) that asymmetric supercapacitor is stable at higher scan rates even at 100 mVs^{-1} as it showed rectangular CV curve which express the excellent rate capability of supercapacitor device.

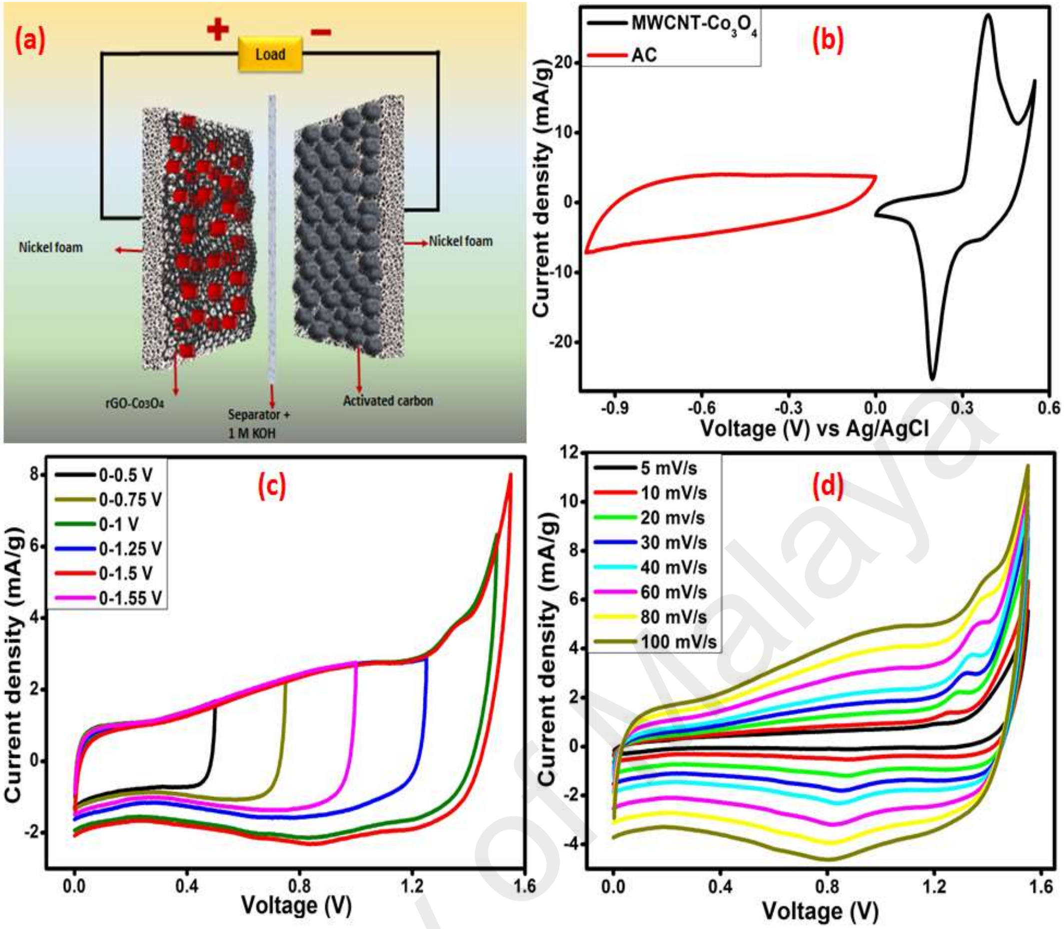

Figure 4.9: (a) Schematic asymmetric supercapacitor assembly, (b) Comparative CV curves of rGO–Co_3O_4 nanocubes as a positive electrode and AC as a negative electrode performed at a scan rate of 10 mV s^{-1} in a three-electrode cell using 1 M KOH electrolyte, (c) CV curves of rGO–Co_3O_4 nanocubes//AC supercapacitor at different potential windows at a scan rate of 50 mVs^{-1} and (d) at different scan rates in 1 M KOH.

(b) Galvanostatic Charge Discharge

The GCD curves for different potential windows were recorded which are shown in Figure 4.10. Almost symmetric charge discharge curves were observed within the potential window of 0-1.55 V (Figure 4.10(a)). This shows the good capacitive behavior with reversible redox reaction of the device (Li *et al.*, 2013). Figure 4.10(b) displays the GCD curves at different current densities (0.2-0.6 Ag^{-1}) in a potential window of 0-1.55 V. It is evident from Figure 4.10(b) that asymmetric supercapacitor possesses non-linear charge discharge curves. This was due to effect of faradaic reaction taking place between rGO–Co_3O_4 nanocubes and electrolyte. This inferred that specific capacity of the device was not only due to the electric double charge storage but also due to the faradaic reaction. The specific capacity of asymmetric device from discharge curve was calculated by the equation 4.2.

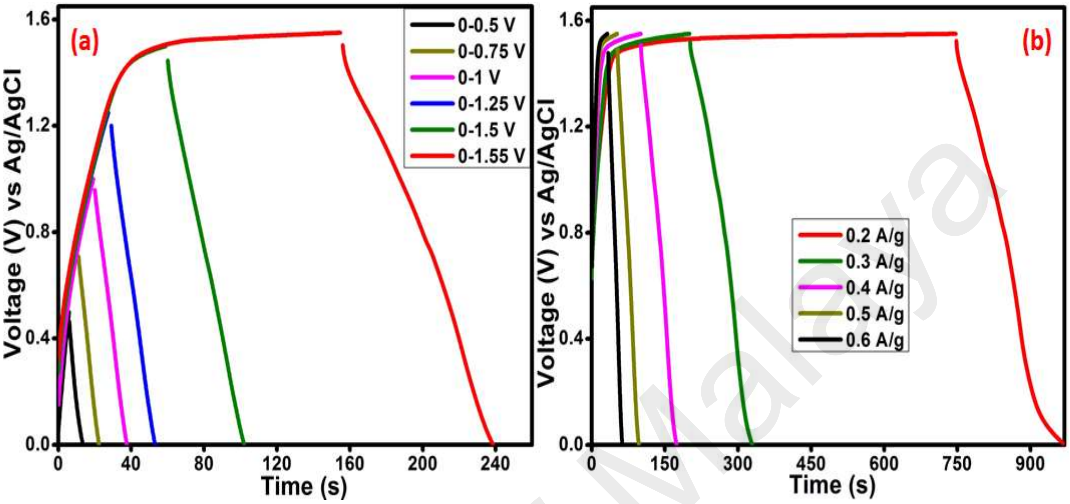

Figure 4.10: GCD curves of rGO–Co_3O_4 nanocubes//AC (a) at different potential windows and (b) at different current densities

The specific capacity of the device found to be 89.9 Cg^{-1} at a current density of 0.2 Ag^{-1}. In addition, supercapacitor also showed good capacitive retention even at elevated current densities. The energy density and power density of rGO–Co_3O_4 nanocubes//AC supercapacitor is calculated by the following formulas;

$$E\ (Wh/kg) = \frac{Q \times \Delta V}{2 \times 3.6} \tag{4.3}$$

$$P\ (W/kg) = \frac{E \times 3600}{\Delta t} \tag{4.4}$$

Where Q is specific capacity, ΔV is the potential window for charge/discharge and t is the discharge time. It is found that the value of energy density decayed from 19.28 to 7.75 $Wh.kg^{-1}$, while the value of power density increased from 309.85 to 996.42 $W.kg^{-1}$ at a current density range of 0.2-6 Ag^{-1}. The maximum power density delivered by the supercapacitor was 996.42 $W.kg^{-1}$ with energy storage capacity of 7.75 $Wh.kg^{-1}$. These values are comparable to the reported work which are summarized in Table 4.1. The power density of rGO–Co_3O_4 nanocubes//AC supercapacitor is significantly high at low current density of 0.2 Ag^{-1} with promising energy density value.

Table 4.1: Performance comparison of rGO–Co_3O_4 nanocubes//AC supercapacitor with reported works

Material	Current density (Ag^{-1})	Power density ($W.kg^{-1}$)	Energy density ($Wh.kg^{-1}$)	Reference
PANI[1]$ZnCo_2O_4$//AC	0.5	375	13	(Omar *et al.*, 2017)
AC//PANI-M90	0.5	378	14.7	(Lee *et al.*, 2017)
Ni_3S_2/MWCNT-NC[2]//AC	1	798	19.8	(Dai *et al.*, 2013)
N300//AC	0.4	559	76	(Omar *et al.*, 2017)
rGO–Co_3O_4 nanocubes//AC	0.2	996.4	7.75	This work
[1]Polyaniline,	[2]NC Conductive carbon nanomaterials			

(c) *Electrochemical Impedance Spectroscopy and Life Cycle Test*

To further elucidate the performance of asymmetric supercapacitor, EIS spectrum was recorded. Figure 4.11(a) displays the EIS spectrum of rGO–Co_3O_4 nanocubes//AC supercapacitor. The low ESR value of 4 Ω manifest that rGO–Co_3O_4 nanocubes//AC based supercapacitor has low internal resistance. Moreover, the diameter of the semicircle at high frequency region determines the faradaic charge transfer resistance (R_{ct}) which depend upon the electrode surface area and electrical conductivity of the electrode material. In case of rGO–Co_3O_4 nanocubes//AC supercapacitor, small circle in high frequency region with R_{ct} value of 2 Ω was observed, revealing the low charge transfer resistance at electrode/electrolyte interface. Inclined line at low frequency region (Warburg impedance) is responsible of OH^- diffusion from electrolyte into the electrode surface. The rGO–Co_3O_4 nanocubes//AC supercapacitor showed vertical spike closer to imaginary axis, demonstrating the excellent capacitive behavior of the device (Sahu *et al.*, 2015).

Besides CV, GCD and EIS, life cycle test is an important performance characterization in order to evaluate the practical application of the device. Figure 4.11(b) depicts the life cycle test of rGO–Co_3O_4 nanocubes//AC supercapacitor. It was found that the capacity retention of assembled asymmetric supercapacitor remained more than 90 % at a current density of 1 Ag^{-1} even after 3000 cycles. This result showed excellent stability of the device.

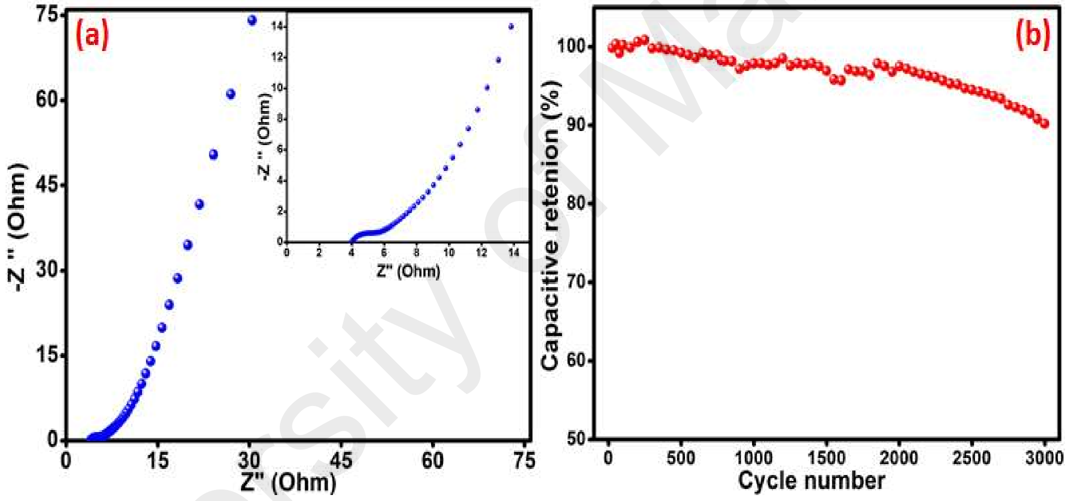

Figure 4.11: (a) EIS spectrum and (b) cycling stability of rGO–Co_3O_4 nanocubes//AC at a current density of 1 Ag^{-1}.

4.3 Structural, Morphological and Electrochemical Characterizations of rGO–Co_3O_4 nanograins[2]

4.3.1 Structural and Morphological Characterizations

4.3.1.1 X-ray Diffraction

The crystalline nature of GO, rGO, Co_3O_4, and rGO–Co_3O_4 nanograins was analyzed by recording the XRD patterns, which are shown in Figure 4.12. The GO (Figure 4.12(a)) exhibited a sharp and intense diffraction peak at a 2θ value of 10° which corresponds to the (001) lattice plane (Wang *et al.*, 2010). The sharpness of the peak indicated that the high interlayer distance is due to the existence of oxygen containing functional groups on the basal plane of GO (Liang *et al.*, 2011). However, the peak of GO disappeared and two broad peaks appeared at 2θ values of 26.8° and 42.7°, attributed to the (002) and (100) lattice planes of the rGO, respectively (Figure 4.12(a, inset)). These peaks arise from the graphene sheets which were disorderedly stacked upon the hydrothermal treatment, which confirms the successful reduction of GO into rGO (Shahid *et al.*, 2014). Figure 4.12(b) shows the XRD patterns of the Co_3O_4 nanograins and rGO–Co_3O_4 nanocomposite. The diffraction pattern of pure Co_3O_4 (shown in Figure 4.12(b, inset)) exhibited strong crystalline peaks at 2θ values of 18.1°, 30.9°, 36.4°, 44.2°, 54.9°, 58.6°, and 64.4° which correspond to (111), (220), (311), (400), (422), (511), and (440) planes, respectively. The rGO–Co_3O_4 nanocomposite showed the same diffraction peaks pattern as Co_3O_4 nanograins, (Figure 4.12(b, inset)). No other characteristic peaks were observed, suggesting the purity of Co_3O_4 nanograins embedded rGO matrix. All XRD

---

[2] **Section 4.3 of this chapter is published as:** Numan, A., Shahid, M. M., Omar, F. S., Ramesh, K., & Ramesh, S. (2017). Facile fabrication of cobalt oxide nanograin-decorated reduced graphene oxide composite as ultrasensitive platform for dopamine detection. *Sensors and Actuators B: Chemical*, 238, 1043-1051.

diffraction peaks for Co_3O_4 nanograins can be indexed as a cubical crystal phase Co_3O_4 (space group Fd-3m (227), PDF-96-900-5893) without showing any impurity phase.

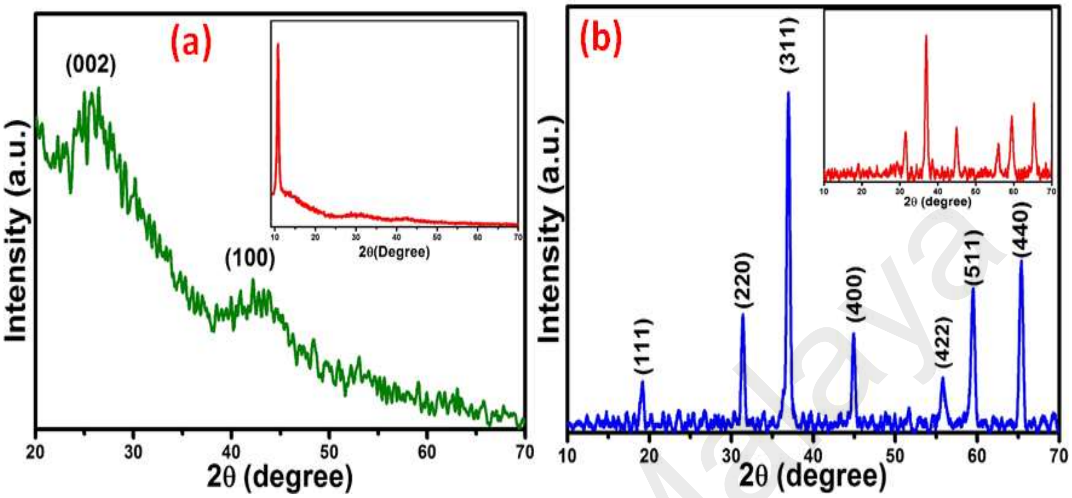

Figure 4.12: XRD patterns (a) rGO (inset GO), (b) rGO–Co_3O_4 nanograins (inset Co_3O_4).

4.3.1.2 Raman Spectroscopy

Raman spectroscopy is a non-destructive conventional tool which is employed to evaluate the functional groups and structural changes in graphite and graphene based materials. The Raman spectrum of GO (Figure 4.13(a)) and rGO (Figure 4.13(a, inset)) show two intense and well-documented *D* band peak at 1351 cm^{-1}, and *G* band peak at 1593 cm^{-1}. The *D* band vibration is attributed to the sp^3 defects produced in the lattice by the breathing mode of k-point photons of A_{1g} symmetry of GO and rGO (Park *et al.*, 2009; Wang *et al.*, 2010). The *G* band refers to the vibration of sp^2 C–C bond in the hexagonal carbon matrix (Chen *et al.*, 2012). The intensity ratio between *D* and *G* bands (*D/G*) is usually employed to specify the average size and degree of structural disorder of the in plane sp^2 domains (Wang *et al.*, 2010). The *D/G* ratio of GO was found to be approximately 0.93, which was significantly increased up to 1.05 in rGO, suggesting the formation of partially ordered crystal structures with a decrease in size of in-plane sp^2 domains and the removal of oxygen moieties during the reduction of GO (Li *et al.*, 2014). However, in rGO–Co_3O_4 nanocomposite, the *D/G* ratio decreased to 0.90, as a result of decrease in the sp^2 domain size (C–C bond) and the reduction of sp^3 to sp^2 carbon (Wang *et al.*, 2010). Additionally, the defects were observed in rGO matrix due to the removal of oxygen containing functional groups from GO layers (Wang *et al.*, 2010). This confirmed the successful reduction of GO into rGO. Despite this, the *2D* band (obtained by the Raman scattering of second order of zone boundary phonons of graphene) is extremely important to differentiate between monolayer, double or multi-layer graphene sheets. A slight increment in the intensity of *2D* band was observed in rGO than GO, suggesting the formation of exfoliated rGO sheets from the stacked multilayer GO sheets. In fact, during the reduction of GO into rGO, oxygen containing functional groups on GO were reduced, which could result in restacking of graphene sheets. However, at the same time Co_3O_4 nanograins get intercalated between the graphene sheets and avoid them from restacking by acting as spacer in between the different layers of graphene. The Raman spectrum of the rGO–Co_3O_4 nanograins remained nearly the same value of D/G for rGO together with *2D* band intensity (Figure 4.13(b)). The peaks aroused at 192, 482, 517, 614 and 687 cm^{-1} are attributed to the B_{1g}, E_g, $F^1{}_{2g}$, $F^2{}_{2g}$ and A_{1g} modes of Co_3O_4, respectively (Fig. 4.13(b, inset)) (Kim *et al.*, 2011).

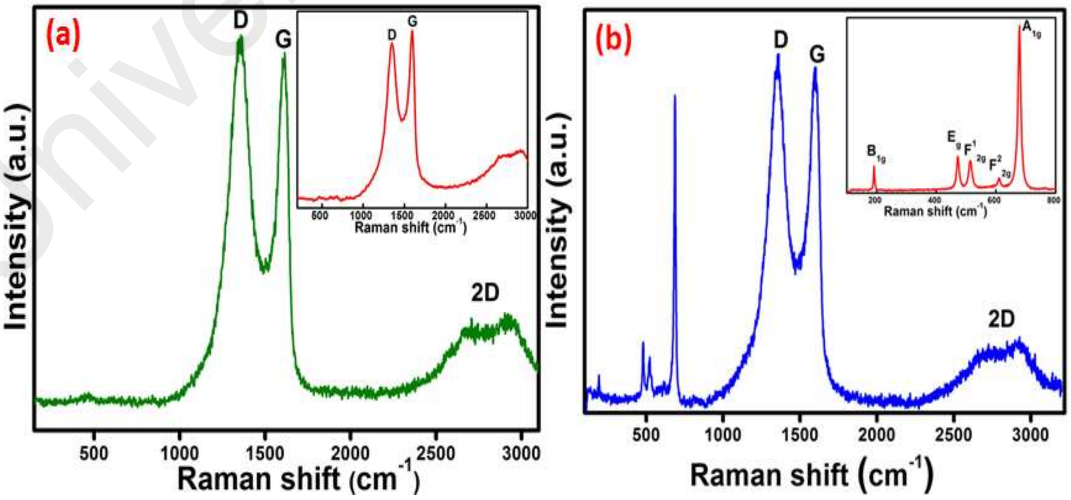

Figure 4.13: Raman spectra of (a) rGO sheets (inset: the Raman spectrum of GO sheets) and (b) rGO–Co_3O_4 nanocomposite (inset: the Raman modes of Co_3O_4 nanograins).

4.3.1.3 Field Emission Scanning Electron Microscopy

The surface morphologies of the synthesized pure Co_3O_4 and rGO–Co_3O_4 nanograins were investigated via FESEM. Figure 4.14(a, inset) showed the formation of granular structure of pure Co_3O_4 with high particle aggregations, which were successfully incorporated on to the surface of transparent rGO sheets without affecting their granular structure. There is a clear distinction between pure Co_3O_4 nanoparticles and in composite with rGO (Figure 4.14(a)). Unaided Co_3O_4 nanograins were highly aggregated, while in rGO–Co_3O_4 nanograins, rGO significantly reduced the aggregations by providing anchoring sites for Co_3O_4 nanograins.

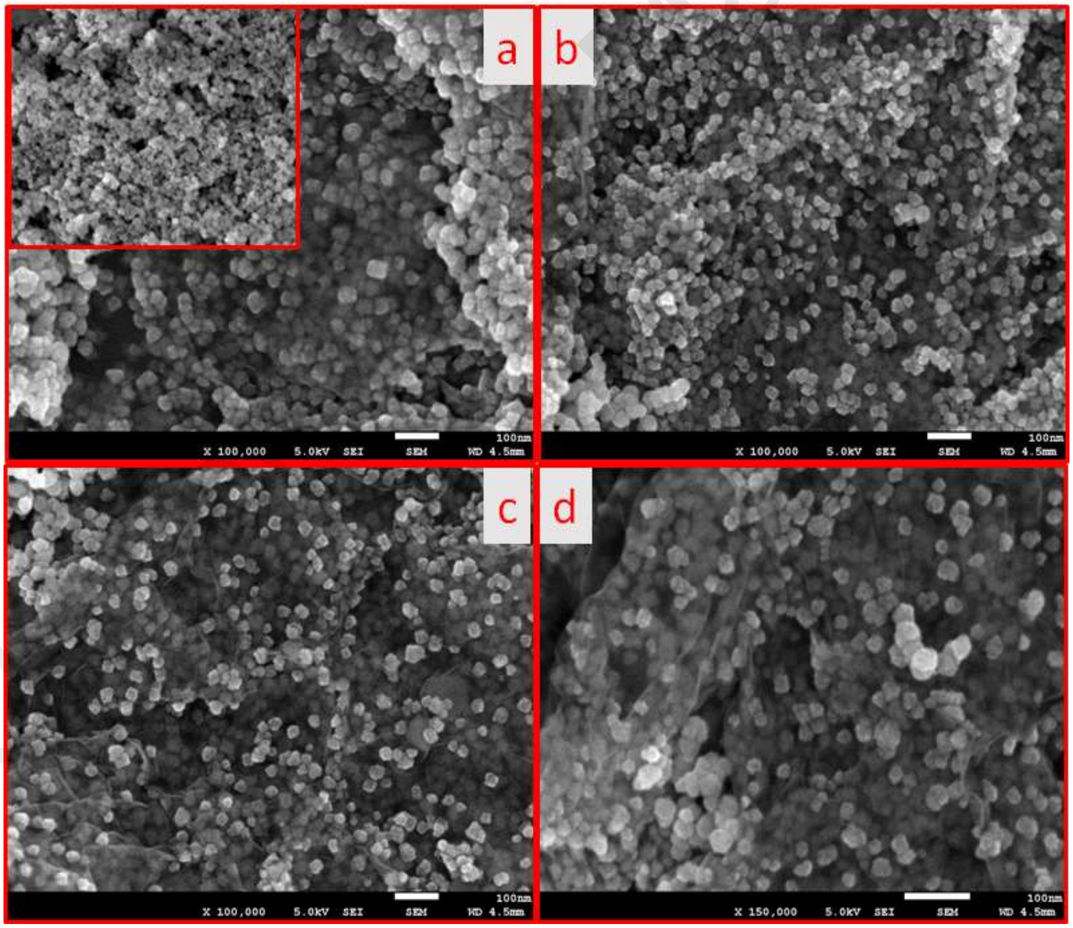

Figure 4.14: FESEM images of rGO–Co_3O_4 nanograins (a) B1 (Inset: Co_3O_4 nanograins), (b) B2, (c) B3 and (d) B4.

The FESEM images (Figure 4.14(a-b)) of B1 and B2 showed some aggregations of Co_3O_4 nanograins. This might be due to the lagging of rGO sheet surfaces which were insufficient to provide nucleation sites for cobalt ions during hydrothermal process. As a result, some of particles of Co_3O_4 grow freely in the phase solution, independent from graphene sheets and tend to aggregate with each other. However, with increasing the GO contents in B3, the aggregation of Co_3O_4 nanograins was decreased as more sites were available for the deposition of Co_3O_4 nanograins on GO sheets (Figure 4.14(c)). In addition, some of the nanograins get intercalated within rGO sheets (displaying blurred image) while most of the nanograins were well distributed and exposed on rGO surface (displaying sharp images). But on further increasing the GO contents in B4, most of the Co_3O_4 nanograins sandwiched within the GO sheets and fewer particles were exposed on the top layer of rGO sheets which resulted in reduction of electrochemical surface area (Figure 4.14(d)).

4.3.2 Electrocatalytic Performance Study of rGO-Co_3O_4 nanograins for Electrochemical Sensing of DA

Cobalt oxide is a well reputed catalyst with its exceptional catalytic activity, whereas rGO being a highly conductive sheet provides a conductive platform to Co_3O_4 nanograins. Thereby, the synergistic effect of rGO and Co_3O_4 nanograins can enhance the electrocatalysis by improving electron transfer rate and good accessibility between DA and electrode surface.

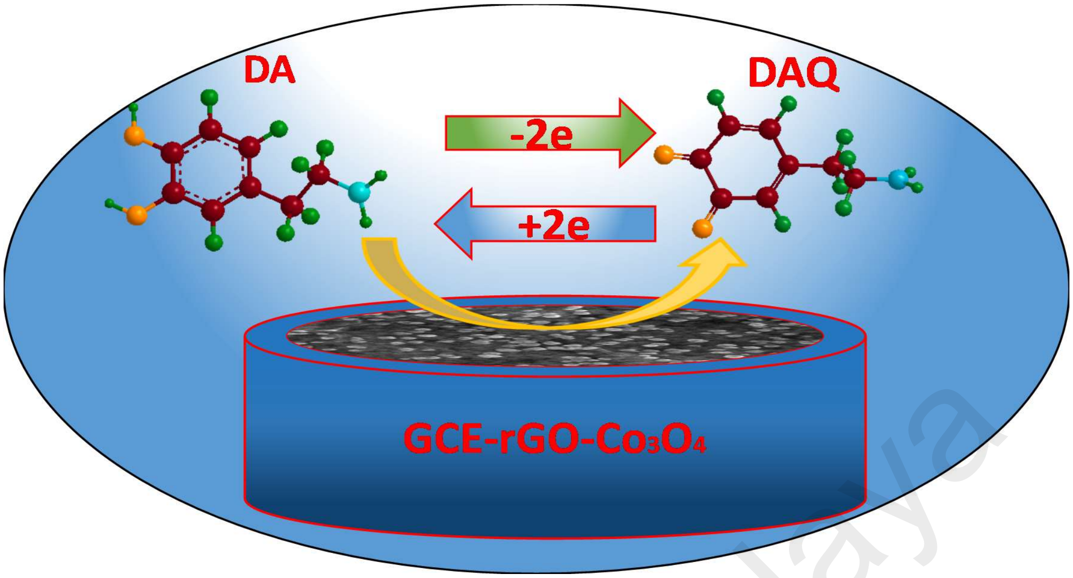

Figure 4.15: Schematic representation of electrocatalysis of DA at rGO–Co_3O_4 nanograins modified GCE.

A schematic illustration of the redox electrochemistry of DA at the rGO–Co_3O_4 nanocomposite modified GCE is depicted in Figure 4.15. Owing to high electroactivity, DA easily gets oxidized electrocatalytically resulting the formation of dopamine quinone (DAQ) on the surface of rGO–Co_3O_4 nanocomposite modified GCE. Upon application of potential to the modified electrode, DA was oxidized to DAQ by exchanging 2 electrons and 2 protons with modified electrode and produce faradaic current (Nurzulaikha *et al.*, 2015).

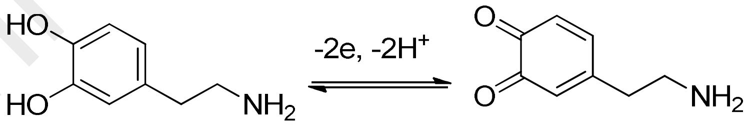

(4.5)

4.3.2.1 Cyclic Voltammetry

The electrocatalytic performance of rGO–Co_3O_4 nanograins modified GCE was examined to elucidate the charge transfer behavior. Figure 4.16 displays the cyclic voltammetric responses of the modified electrodes in 0.1 M phosphate buffer (PB) (pH 7.2) at a scan rate of 50 mVs^{-1} in the presence of 0.5 mM DA. The background current for the bare GCE (black line) showed well-defined redox peaks with the anodic (E_{pa}) and cathodic (E_{pc}) peaks at 285 mV and 14 mV respectively with the peak difference (ΔE) of 271 mV. However, a significant shift of oxidation peak to the lower potential with improved peak current was observed in the case of unaided Co_3O_4 nanorgrains modified GCE, which indicates decent electrocatalytic activity of Co_3O_4 nanograins towards DA. Further noticeable improvement in redox peak current was observed in B1 and B2 modified GCE. This enhancement in electrochemical behavior can be ascribed to the presence of electrically conductive platform of rGO that was providing excellent electron transport facility which in turn accelerated the electron kinetics at the electrode/electrolyte interface. However, in case of B4 (blue line) modified GCE, a decrease in redox peak current was observed without any significant shift in peak potentials.

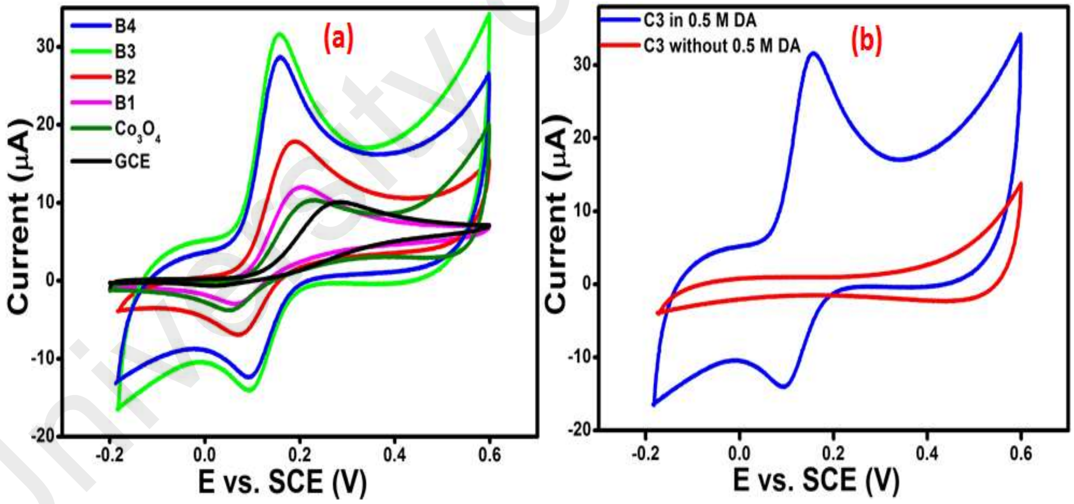

Figure 4.16: (a) CV obtained for bare GCE, Co_3O_4 nanograins, B1, B2, B3 and B4 modified GCE in 0.5 mM DA with 0.1 M PB at a scan rate of 50 mVs^{-1} (b) Comparison of CV curves of B3 with and without 0.5 M DA in 0.1 M PB.

It is evident that rGO–Co_3O_4 nanograins exhibited excellent catalytic activity for DA detection as compared to unaided Co_3O_4 nanograins and bare GCE. This supports the fact that rGO provided enhanced conductive area for Co_3O_4 nanograins and contributed effectively in electron promotion during electrocatalytic oxidation of DA. Enhanced electrocatalytic response was observed for B3 modified/GCE (green line) as compared to B1, B2 and B4. It exhibited 3.1 fold higher current and very small redox peak difference (ΔE = 69 mV) as compared to bare GCE. The poor response of B1 and B2 to oxidize DA might be due to the aggregation of Co_3O_4 nanograins caused by low concentration of rGO, which result in the reduction of exposed electrochemical surface area to electrolyte. The less exposure of Co_3O_4 nanograins in B4 (Figure 4.14(d)) on the top surface of rGO was due to the sufficient number of rGO sheets that significantly decrease the density of Co_3O_4 nanograins. These results are in good agreement with aforementioned FESEM results. The B3 was considered optimized sample for further electrochemical studies. In order to confirm the oxidation of DA, background studies were performed by running CV with and out presence of DA in 0.1 M PB. From Figure 4.14(b) it is evident that redox peaks are due to the presence of DA. In the absence of DA no peak was found, which confirmed that redox peaks arose from the electro oxidation of DA.

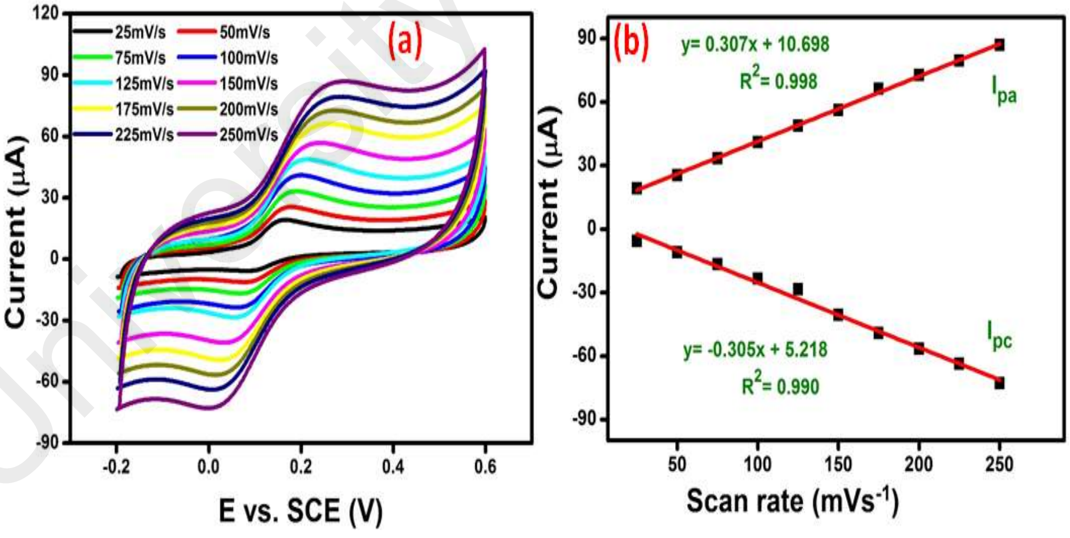

Figure 4.17: (a) CVs observed for rGO–Co_3O_4 nangrains (B2) in 0.1 M PB (pH 7.2) containing 0.1 mM DA at various scan rates, (b) the plots of peak current versus the scan rates.

The influence of scan rates on the electrocatalytic response of B3 modified GCE towards DA oxidation was studied at different scan rates (from 25 to 250 mVs^{-1}). It is evident from Figure 4.17(a) that by increasing the scan rates, redox peak current also increased linearly with a slight shift in oxidation potential in the positive direction, indicating the occurrence of quasi-reversible reaction. The calibration plot (Figure 4.17(b)) of redox peak currents (I_{pa} & I_{pc}) with scan rates showed a linear correlation (R^2=0.998 and 0.99) which revealed that the electroxidation of DA at rGO–Co_3O_4 nanograins (B3) modified GCE is an adsorption controlled process (How *et al.*, 2014; Suresh *et al.*, 2014).

The CV curve (Figure 4.18(a)) were recorded for composite B3 modified GCE at different molar concentrations of DA in 0.1 M of PB (pH 7.2). Significantly, the oxidation peak current increased linearly with the addition of DA in the range of 0.5 to 5 mM and anodic peak potential underwent a slightly positive shift. The logarithmic plot of peak current (I_{pa}) and different concentrations DA showed a linear plot with a slope value nearly equal to 1, which confirms that the electrochemical oxidation of DA follows the first order kinetics with respect to DA concentration at the C3 composite modified electrode (Figure 4.18(c)).

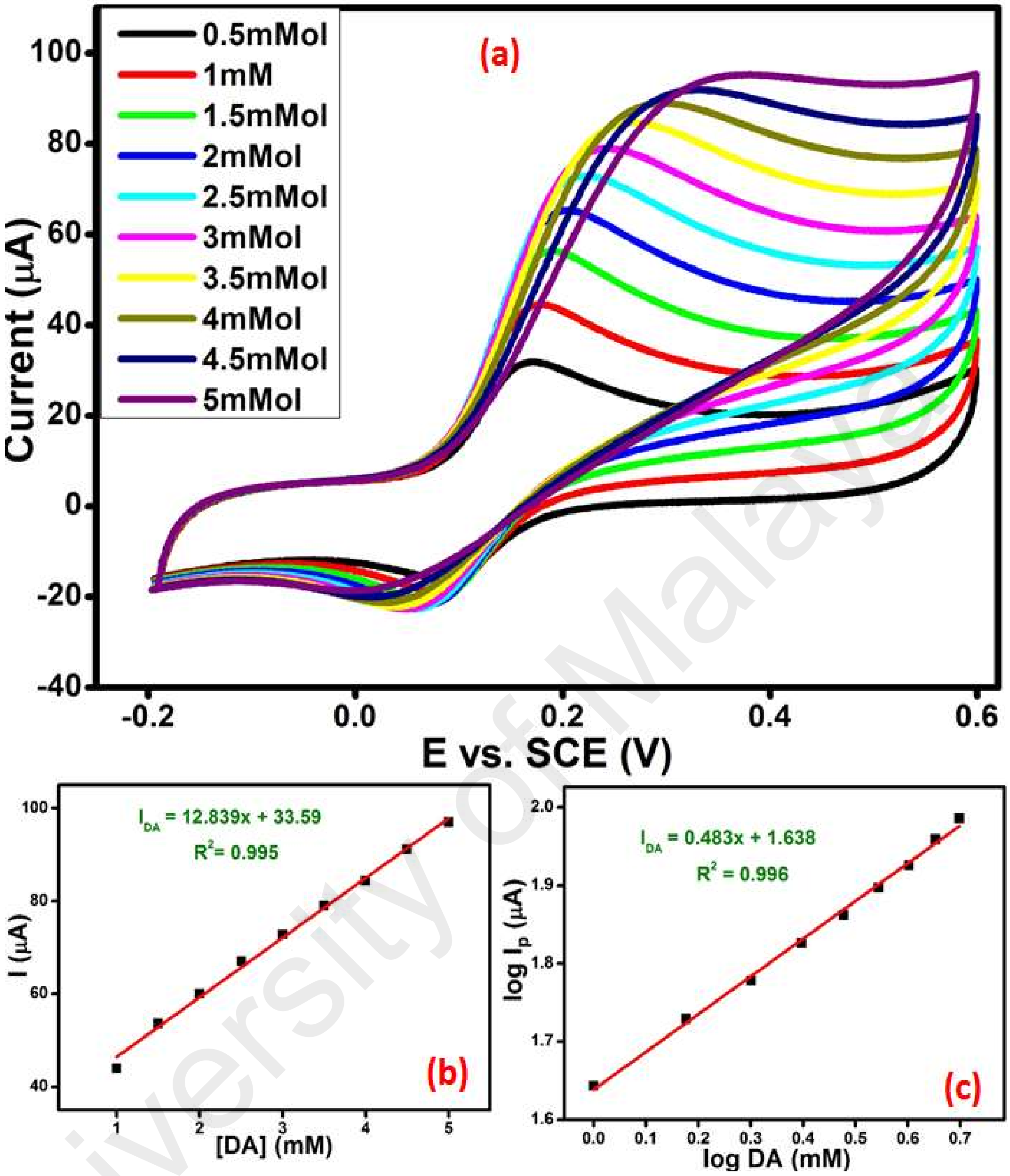

Figure 4.18: (a) Cyclic voltammograms obtained at the rGO–Co_3O_4 nanograins modified electrode during the successive addition of different concentrations (b) Plot of I_{pa} vs molar concentration of DA (c) Plot of log I_{pa} vs log [molar concentration of DA].

4.3.2.2 Choronoamperometry

The amperometric detection method is an important tool for the detection of low concentrations of bioanalytes and to perform the interference studies. Figure 4.19(a) depicts the amperometric responses of B3 modified GCE on the successive injections of 1 μM of DA in a homogeneously stirred solution of 0.1 MPB at a fixed time interval of

60 s. It can be seen that B3 modified GCE showed rapid response by significant increase in response current to each injection of DA at a fixed potential of +0.16 V, indicating that the B3 modified GCE was effectively stimulated the oxidation of DA in 0.1 M PB (pH 7.2). The calibration curve (Figure 4.19(b, inset)) indicates that the B3 modified GCE performs a linear response towards DA with the concentration from 1 to 30 μM.

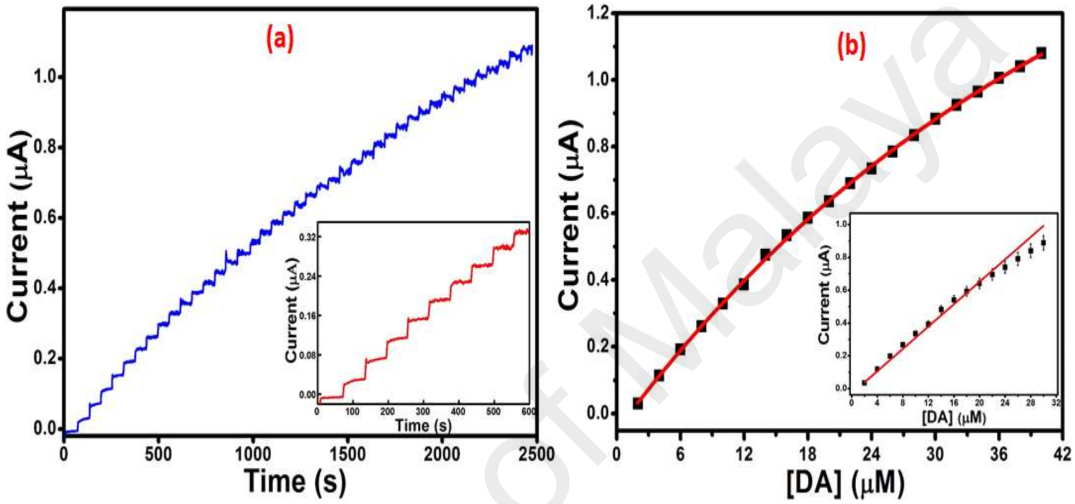

Figure 4.19: Amperometric i–t curve obtained at B3 modified GCE for the successive addition of 1 mM DA in 0.1 M PB (pH 7.2) at an applied potential of +0.16 V with a regular interval of 60 s (b) corresponding calibration plot of current versus concentration of DA.

The limit of detection (LOD) and limit of quantification (LOQ) for DA can be estimated using the standard deviation of the y-intercepts (SD) and the slope of the regression lines (S) (LOD = 3.3(SD/S) and LOQ = 10(SD/S)) (Kim *et al.*, 2010). The LOD and LOQ values for DA using B3 modified GCE were found to be 0.277 μM and 0.924 μM respectively. The sensitivity of B3 modified electrode was 0.389 ± 0.005 μA μM^{-1} cm^{-2}. The comparison of the electrochemical sensing performance of the present B3 modified GCE in terms of LOD, sensitivity, selectivity and linear range are comparable with some of the reported GCE based electrochemical sensors for the detection of DA, which is summarized in Table 4.2.

Table 4.2: A comparison of some of the reported electrochemical sensors for DA detection.

Type of Electrode	Method	pH	LOD (µM)	LOQ (µM)	Linear range (µM)	Sensitivity (µAµM^{-1})	Reference
Graphene/SnO$_2$/GCE	DPV[1]	6.8	1	Nil	0-100	Nil	(Nurzulaikha *et al.*, 2015)
rGO/TiO$_2$/GCE	DPV	6.5	6	Nil	2-60	Nil	(How *et al.*, 2014)
V$_2$O$_5$@PANI/GCE	CA	Nil	0.39	130	6.6-110	Nil	(Suresh *et al.*, 2014)
Graphene/GCE	DPV	Nil	2.64	Nil	4-100	Nil	(Kim *et al.*, 2010)
FANE[2]	DPV	7.4	0.2	Nil	1 – 150	Nil	(Zheng *et al.*, 2013)
ERGO[3]/GCE	DPV	7	0.5	Nil	0.5 – 60	0.482	(Yang *et al.*, 2014)
(GE/Au/GE/CFE)	DPV	7	0.59	Nil	0.59–43.95	Nil	(Du *et al.*, 2013)
rGO–Co$_3$O$_4$ nanograins	CA	7.2	0.277	0.924	0–30	0.389	Present work

[1] Differential pulse voltammetry [2] Flower-like Au nanostructure-covered gold electrode

[3] Electrochemically reduced graphene oxide

4.3.2.3 Interference Study

Further, the selectivity of the B3 for the detection of DA was examined by injecting three different interfering species; uric acid, glucose and AA in the evenly stirred PB containing DA and the change in the current response was observed. Figure 4.20 depicts the recorded amperometric i–t curve response for the consecutive additions of DA and interfering species (sample time of 60 s) in a homogeneously stirred 0.1 M PB (pH 7.2). First, alternate injections of DA with uric acid, glucose and AA were used to record the current response. On each injection of DA, current response was observed which was equal to the oxidation current of DA. On the other hand, the injections of interfering species did not give any current response even with 100 fold higher concentration than

DA. Next, three consecutive injections of DA followed by three injections of UA, glucose and AA respectively were used to analyze the current response. Again interfering species did not show any current response, contrary to the DA which gave current stair on each injection. This confirmed that the addition of interfering species did not contribute any current response even with a 100-fold higher concentration than DA.

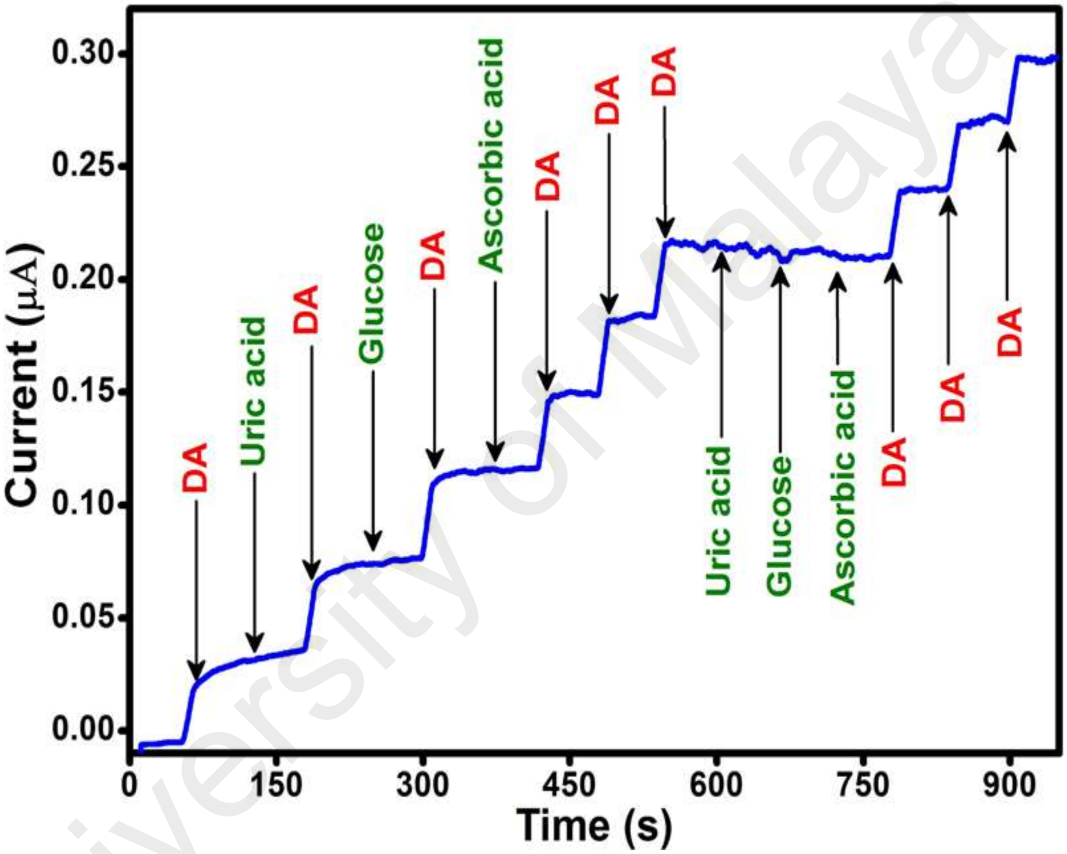

Figure 4.20: Amperometric i–t curve obtained at B3 modified GCE for the successive addition of 1 µM of DA and each 1 mM of uric acid, glucose and AA in 0.1 M PB (pH 7.2) at a regular interval of 60 s. The applied potential was + 0.16 V.

On the other hand, every injection of DA in the same solution showed approximately the same magnitude of response current for the oxidation of DA. This phenomenon is due to low oxidation potential (+ 0.16) which was used in amperometric method for interference studies. The low potential helped in detecting DA selectively even in the presence of high concentration interfering species. These results revealed that the present sensor possesses good selectivity and sensitivity towards the quantitative determination of DA even in the presence of common physiological interfering species.

4.3.2.4 Real Time Sample Test

In order to evaluate the performance and reliability of proposed sensor in real application, analytical determination of DA in two urine samples was performed using standard addition method. The analytical results were summarized in Table 4.3. To ascertain the accuracy of the results, different concentrations of DA were added in urine containing PB solution and detected. The recovery of spiked sample ranged between 98.3 to 103.4 %, which indicated the successful application of rGO-Co_3O_4 nanograins for the detection of DA.

Table 4.3: Determination results of DA by using rGO–Co_3O_4 nanograins in real urine samples (n = 3).

Urine sample	**Add concentration (µM)**	**Found Concentration (µM)**	**RSD (%)**	**Recovery (%)**
Sample 1	1	1.010	1.48	101
	3	2.972	1.04	99.1
	6	5.900	2.58	98.3
Sample 2	1	1.034	1.68	103.4
	3	2.948	1.07	98.3
	6	6.011	1.17	100.1

4.3.2.5 Stability and Reproducibility

For the stability study of proposed sensor, the CV response of B3 modified GCE was recorded for DA in a range between -0.2 and 0.6 V at a scan rate of 50 mVs^{-1}. The CV response was recorded on each day for one week. The peak current was considered as a factor for indicating the stability of the modified electrode. Here, I is the current response of fresh sensor and I_0 is the current response after storage as shown in Figure 4.21. A 10.3 % decrease in the anodic peak current with slight shift in peak potential was observed after one week. This revealed that B3 modified GCE can also withstand being stored in solution for a period of time (one week) and the electrocatalytic performance remain almost unchanged, which confirms that modified electrode is very stable and reproducible for the detection of DA.

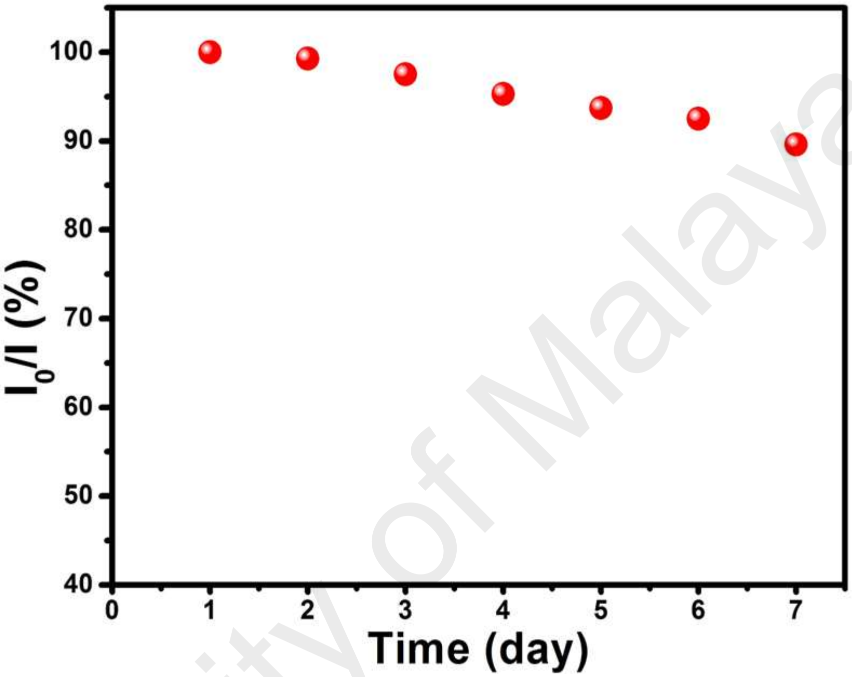

Figure 4.21: Stability of the proposed sensor stored at ambient conditions over 7 days using 0.1 M PB (pH 7.2).

4.4 Structural, Morphological and Electrochemical Characterizations of MWCNT-Co_3O_4 nanocubes[3]

4.4.1 Structural and Morphological Characterizations

4.4.1.1 X-ray Diffraction

XRD analysis was performed in order to investigate the crystallinity and phase purity of the nanocomposite. Figure 4.22(a) and 4.22(b) depicts the XRD patterns for acid

---

[3] **Section 4.4 of this chapter is published as:** Numan, A., Shahid, M. M., Omar, F. S., Rafique, S., Bashir, S., Ramesh, K., & Ramesh, S. (2017). Binary nanocomposite based on Co_3O_4 nanocubes and multiwalled carbon nanotubes as an ultrasensitive platform for amperometric determination of dopamine. *Microchimica Acta*, 1-10.

treated MWCNTs and MWCNT−Co_3O_4 nanocomposite (C4), respectively. For MWCNTs (Figure 4.22(a)) the diffraction peaks were observed at 2θ value of 25.9° and 43° corresponding to the (0 0 2) and (1 0 0) lattice planes of hexagonal graphite structure. This suggests that cylindrical structure of MWCNTs was partially damaged during acid treatment (Irfan *et al.*, 2015). In XRD pattern for MWCNT−Co_3O_4 nanocomposite (Figure 4.22(b)), major diffraction peaks were observed around 31.3°, 36.9°, 44.9°, 55.5°, 59.4° and 65.2° which can be indexed to (2 2 0), (3 1 1), (4 0 0), (4 2 2), (5 1 1) and (4 4 0) crystal planes of face centered cubic structure of Co_3O_4 (JCPDS Card No. 65-3103) without showing any impurity peak (Su *et al.*, 2014) . The pure cobalt oxide nanocubes exhibited strong crystalline peaks at the same 2θ value (Figure 4.22(a, inset)), confirming the successful synthesis of Co_3O_4 nanocubes.

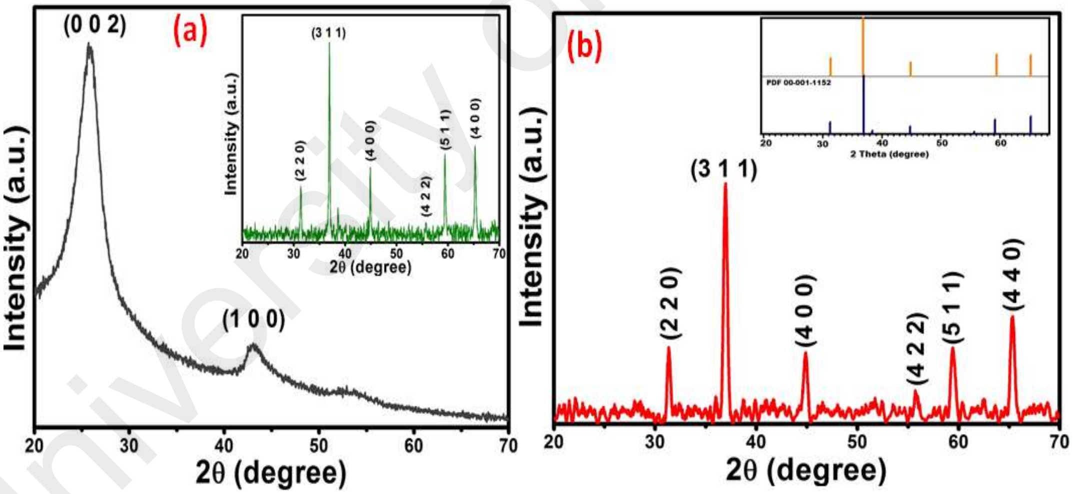

Figure 4.22: (a) XRD patterns of MWCNTs (inset: Co_3O_4 nanocubes), (b) XRD patterns of MWCNT−Co_3O_4 nanocomposite (C4) (inset: matched stick pattern).

4.4.1.2 Raman Spectroscopy

Raman spectroscopy is an effective and non-destructive technique to analyze the structural changes and defects produced due to the growth of metal/metal oxide nanostructures on the surface of *sp*^{2} nanocarbon based materials. Figure 4.23(a) and 4.23 (b) show the Raman spectra for acid treated MWCNTs and MWCNT−Co_3O_4

nanocomposite, respectively. Three well documented and prominent *D*, *G* and *2D* band peaks were observed at 1347, 1577 and 2937 cm^{-1} respectively, for both acid treated MWCNTs and MWCNT−Co_3O_4 nanocomposite (C4). The *D* (defect) band arose due to the presence of defects or disorder structure (vacancies and heptagon-pentagon pairs) on the surface of MWCNTs, while *G* (graphite) band was attributed to the hybridized C-C stretching vibration along MWCNT axis (Figure 4.23(a) and 4.23(b)) (Dresselhaus *et al.*, 2002; Guan *et al.*, 2013). Thus, the ratio between the intensity of *D* and *G* bands (I_D/I_G) can be employed to analyze the structural disorder and degree of graphitization during integration of Co_3O_4 nanocubes to MWCNTs. The I_D/I_G value for acid treated MWCNTs was estimated to be 1.92, which was due to the partially damaged structure caused by the surface modification of MWCNTs during acid treatment. However, after the growth of Co_3O_4 nanocubes in hydrothermal treatment, I_D/I_G value together with *2D* band intensity decreased slightly to 1.17 (Figure 4.23(b)). The decrease in the intensity of I_D/I_G from 1.92 to 1.17 value was attributed to the graphitic veracity followed by formation of small graphitic fragments (Colindres *et al.*, 2014). This also revealed that integration of Co_3O_4 nanocubes involved chemical bonding with the surface of MWCNTs rather than physical decoration(Moghim *et al.*, 2015) . In addition to this, small peaks at 193, 469, 515, 610 and 747 cm^{-1} were also observed, which correspond to the $B^1{}_g$, $E^2{}_g$, $F^2{}_g$, $F^1{}_g$ and $A^1{}_g$ respectively (Figure 4.23 (a, inset)). These peaks are attributed to the phonon modes of Co_3O_4 (Numan *et al.*, 2016).

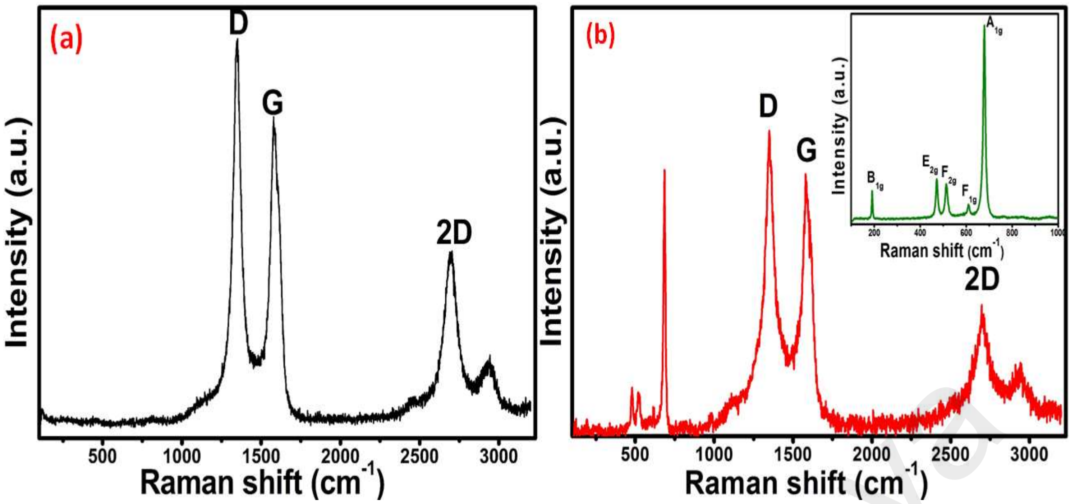

Figure 4.23: (a) Raman spectrum of MWCNTs, (d) Raman spectrum of MWCNT−Co_3O_4 nanocubes (C4) (inset: the Raman spectrum of Co_3O_4 nanocubes).

4.4.1.3 X-ray Photoelectron Spectroscopy

XPS analysis was performed to investigate the chemical composition and binding states of MWCNT−Co_3O_4 nanocomposite (Figure 4.24). All binding energies found through XPS spectra were calibrated first using the C1*s* photoelectron peak at 284.8 eV as the reference. The survey scan spectrum of MWCNT−Co_3O_4 nanocomposite shown in Figure 4.24(a) displayed the sharp and well defined peaks at 284.6, 530.1 and 779.8 eV corresponding to the characteristic peaks of C 1*s*, Co 2*p* and O 1*s* respectively. The core level deconvoluted spectrum of C 1*s* in Figure 4.24(b) consists of four peaks having binding energies at 284.6, 285.4, 288.6 and 289.0 eV. The peaks at 284.6 and 285.4 eV correspond to the non-oxygenated sp^2 (C=C) and sp^3 (C−C) hybridized carbon, while the peaks at 288.6 and 289.0 eV are attributed to the presence of carbon in carbonyls (HO-C = O) and carboxyl (HO-C = O) functional groups (Abouali *et al.*, 2015; Tan *et al.*, 2016). Figure 4.24(c) depicts the high resolution spectrum Co, containing two major peaks of binding energies at 780.6 and 795.5 eV correspond to the $2p_{3/2}$ and $2p_{1/2}$ respectively. The gap between two peaks is about 15 eV with the peak intensity ratio ($2p_{3/2}$: $2p_{1/2}$) of 2:1, which are the typical characteristic of standard of Co_3O_4 spectrum (Tan *et al.*, 2015). In addition to this, weak shake-up satellite peak at 786.9 eV is observed which confirmed the existence of Co^{2+} in the composite (Huang *et al.*, 2012). The core level spectrum of O 1*s* is resolved into four Gaussian peaks at 529.7, 530.1, 531.6 and 533.3 eV (Figure 4.24(d)). The peak at 529.7 eV is ascribed to the lattice oxygen of Co_3O_4. The other three peaks at higher binding energy values of 530.1, 531.6 and 533.3 eV are associated with the oxygen in cobalt monoxide hydroxide ions, oxygen containing bonds (C-O/C=O) and water contents adsorbed on the surface of Co_3O_4 (Li *et al.*, 2006; Xiong *et al.*, 2012).

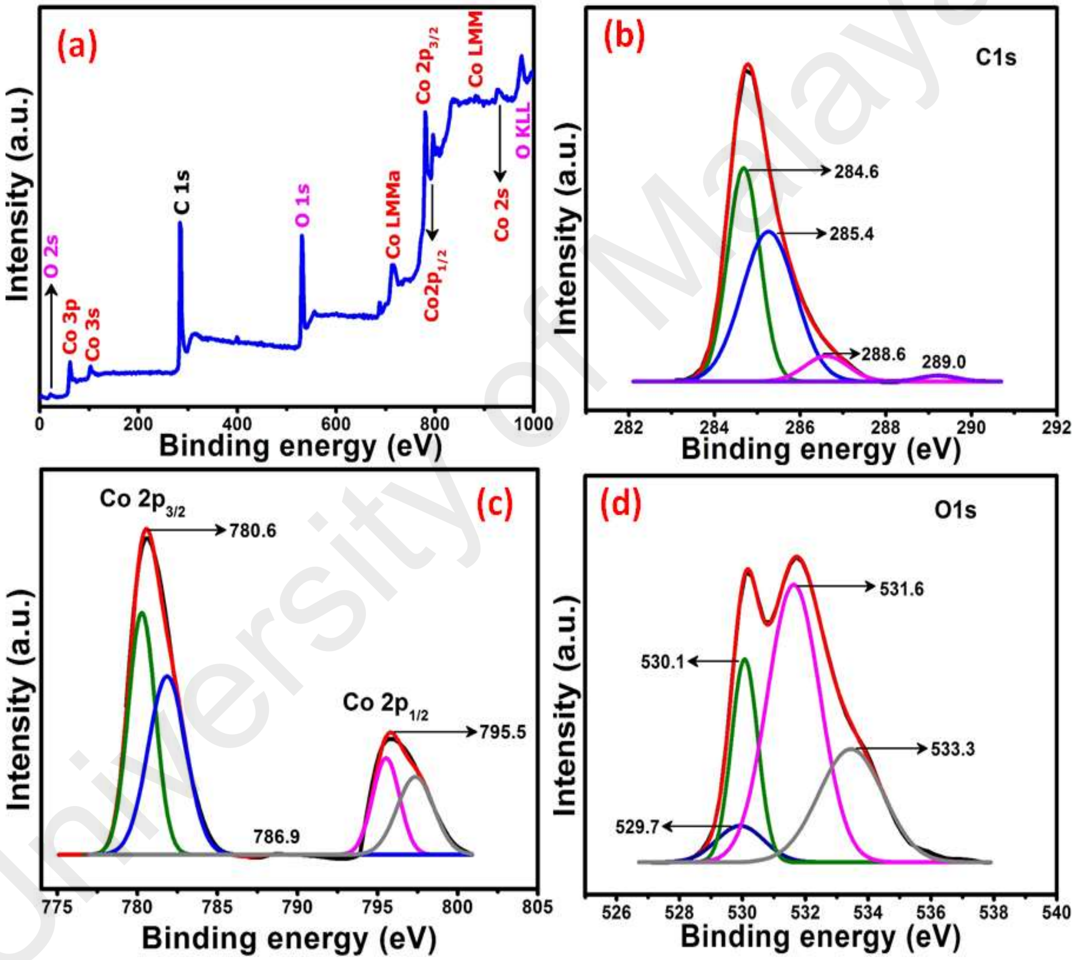

Figure 4.24: (a) Survey spectrum of the MWCNT−Co_3O_4 nanocomposite (C4), (b) high resolution spectrum of the C 1*s* region, (c) high resolution spectrum of the Co 2*p* region and (d) high-resolution spectrum of the O 1*s* region.

4.4.1.4 Field Emission Scanning Electron Microscopy

The surface morphology of synthesized nanocomposite was also confirmed by FESEM images (Figure 4.25). Highly aggregated Co_3O_4 nanocubes were observed in Figure 4.25(a) in the absence of MWCNTs. However, upon addition of MWCNTs, these aggregations were significantly decreased resulting in highly exposed and well decorated Co_3O_4 nanocubes, which is shown in Figure 4.25(b). But due to lower contents of MWCNTs in C1, C2 and C3, some of the particles grow independently in the solution phase and tend to aggregate (Figure 4.25(a), (b) & (c)). The reduced contents of MWCNTs were insufficient to provide the anchoring site for the growth of Co_3O_4 nanocubes, therefore, Co_3O_4 nanocubes grow independently and aggregate together. Upon increasing the contents of MWCNTs in C3, the particle aggregations were eliminated and uniform distribution of Co_3O_4 nanocubes over MWCNTs was obtained (Figure 4.25(e)). Further increase in the contents of MWCNTs resulted in the bundling of MWCNTs covering Co_3O_4 nanocubes. This led to the decrease the exposure of nanocubes and electrochemical surface area (Figure 4.25(f)). Hence, C4 was the optimized composite in which 16 wt. % (40 mg) of MWCNTs was the optimum amount for uniform integration of Co_3O_4 nanocubes.

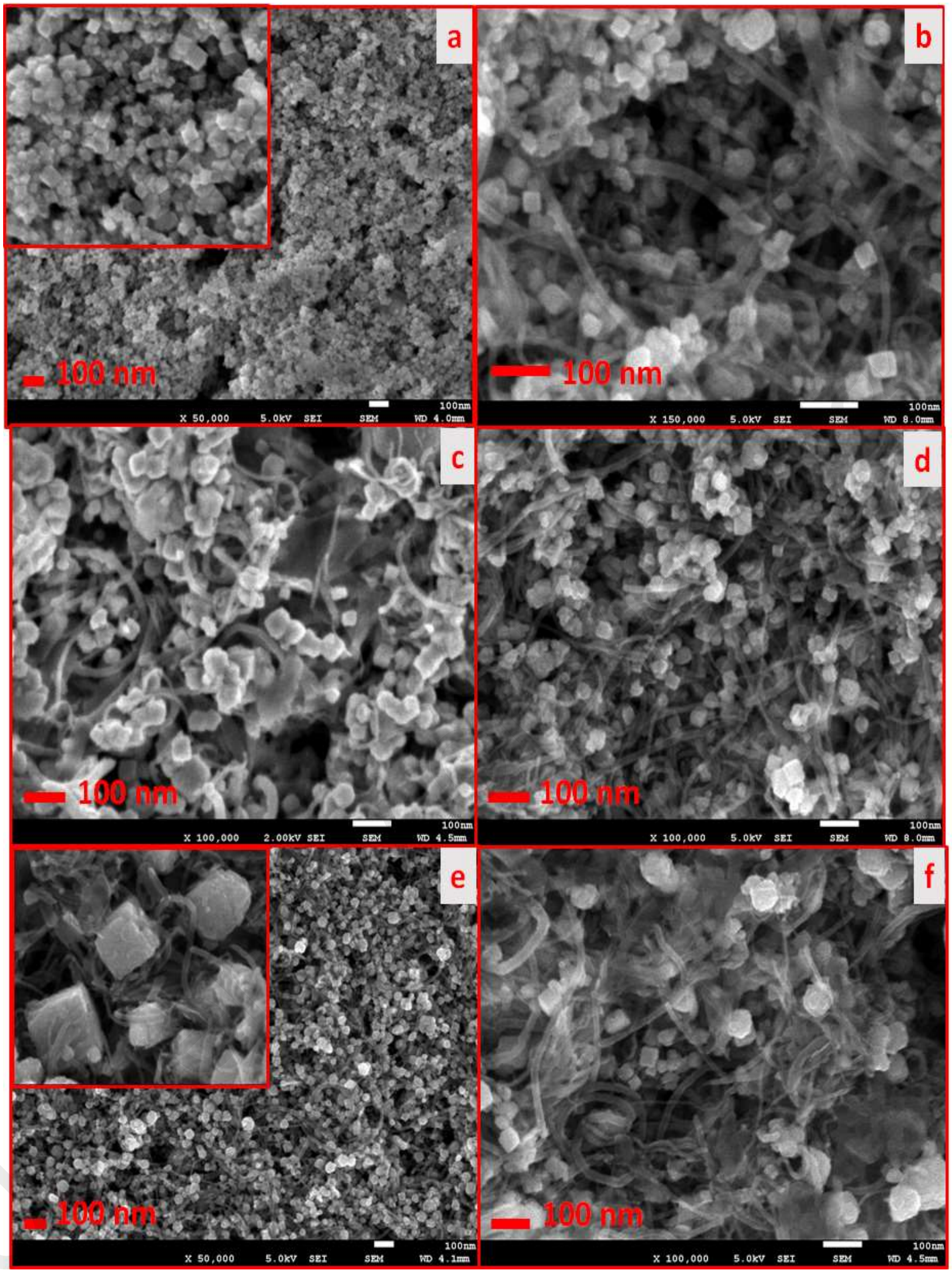

Figure 4.25: FESEM images of (a) low resolution image of Co_3O_4 nanocubes, (inset; high resolution of Co_3O_4) (b) C1, (c) C2, (d) C3, (e) C4, (inset; high resolution of Co_3O_4) and (f) C4.

4.4.1.5 Energy-Dispersive X-ray Spectroscopy and Mapping

The elemental distribution and purity of MWCNT−Co_3O_4 nanocomposite was analyzed by EDX elemental mapping (Figure 4.28). The EDX spectrum shown in Figure

4.26(a, inset) displays the prominent peaks of cobalt, oxygen, carbon and silicon (arose from the substrate) without showing impurity peak. Figure 4.26(a) shows the FESEM image of nanocomposite used for EDX elemental mapping. The independent elemental Co, O and C distributions are shown in Figure 4.26(b), (c) and (d) respectively, which display a uniform distribution of all elements. High density of red (Figure 4.26(b)) and blue (Figure 4.26(d)) dots are evidence of increased amounts of Co and C in the MWCNT−Co_3O_4 nanocomposite. Moreover, the combined elemental distribution shown in Figure 4.26(e) depicts the homogeneous distribution of all color dots indicating the uniform decoration of Co_3O_4 nanocubes on MWCNTs.

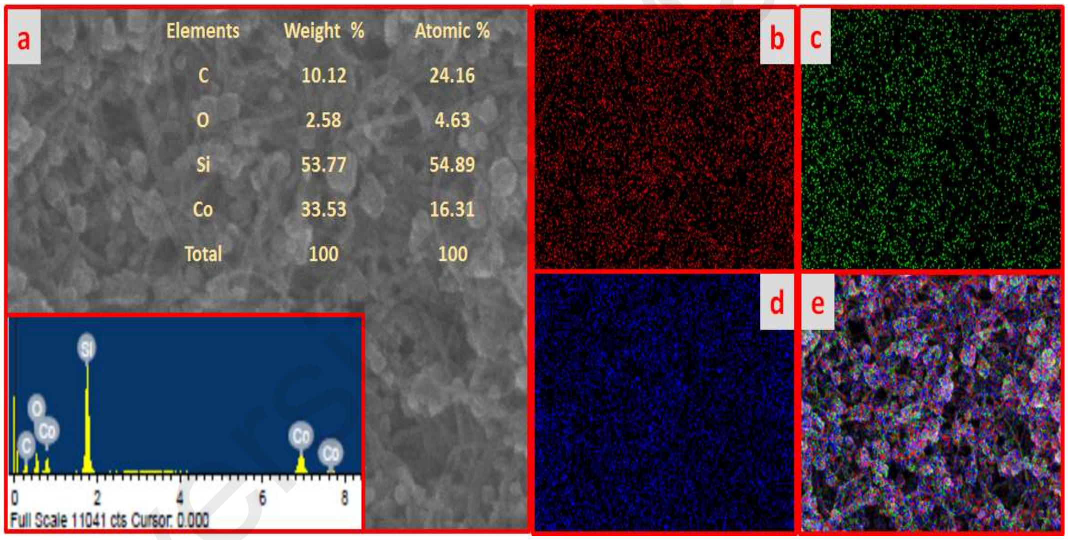

Elements	Weight %	Atomic %
C	10.12	24.16
O	2.58	4.63
Si	53.77	54.89
Co	33.53	16.31
Total	100	100

Figure 4.26: (a) FESEM image of MWCNT−Co_3O_4 nanocomposite (inset: EDX spectrum), (b) EDX mapping of (b) Co, (c) O, (d) MWCNTs and (e) MWCNT−Co_3O_4 nanocomposite.

4.4.1.6 High Resolution Transmission Electron Microscopy

HRTEM micro images were taken to investigate microstructure and the surface morphology of the synthesized hybrid. Figure 4.27 shows the HRTEM images of Co_3O_4 nanocubes, MWCNTs and MWCNT−Co_3O_4 nanocomposite. From Figure 4.27(a) & (b), sharp and well defined cubical structured Co_3O_4 nanoparticle with an average particle size of 32.5 nm are evident. Figure 4.27(a, inset) shows the distance between adjacent planes is 0.47 nm, corresponding to the inter-planar spacing of (111) plane of Co_3O_4 (Panwar *et al.*, 2015) . On the other hand, lose and unbundled acid treated MWCNTs with broader length distributions are shown in Figure 4.27(c). The dispersed MWCNTs were due to the electrostatic repulsion of electronegative functional groups on the surface of MWCNTs, which restricts them from bundling. During hydrothermal reaction, MWCNTs served as a platform for the growth of Co_3O_4 nanocubes. The functional groups on the cylindrical surface of MWCTNs served as nucleation sites for the growth as discussed earlier. This resulted in uniform distribution of Co_3O_4 nanocubes, which leads in the enhancement of electrochemical surface area (Figure 4.27(d)). Moreover, the average particle size (32 nm) remained the same in the composite (Figure 4.27(e)). The selected area electron diffraction (SAED) pattern of MWCNT−Co_3O_4 nanocomposite (Figure 4.27(f)) displayed six strong lattice fringes (2 2 0), (3 1 1), (4 0 0), (4 2 2), (5 1 1) and (4 4 0) correspond to the characteristic peaks of face centered cubic structured of Co_3O_4 demonstrated by XRD.

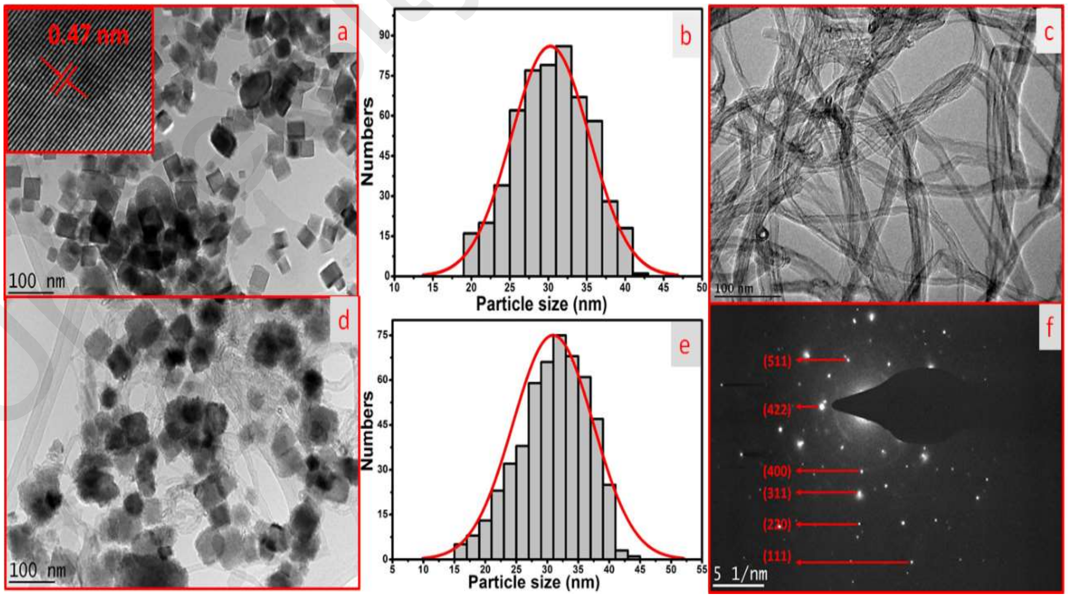

Figure 4.27: HRTEM images of (a) MWCNT−Co_3O_4 nanocomoposite (inset: lattice fringes), (b) particle size distribution of Co_3O_4 nanocubes, (c) acid treated MWCNTs, (d) MWCNT−Co_3O_4 nanocomposite (C4), (e) particle size distribution of Co_3O_4 in composite MWCNT−Co_3O_4 and (f) SAED pattern of MWCNT−Co_3O_4 nanocomposite.

4.4.2 Electrochemical Performance Study of MWCNT─Co_3O_4 nanocubes for Supercapacitor

4.4.2.1 Cyclic Voltammetry

In order to investigate and optimize the MWCNT─Co_3O_4 nanocomposite, CV curves were recorded in standard three electrode cell system in a potential window from 0─0.55 V. Figure 4.28 depicts the CV results of all nanocomposites (pure Co_3O_4, C1, C2, C3, C4 and C5) at different scan rates (3, 5, 10, 20, 30, 40, and 50 mVs^{-1}). Each sample showed well defined redox peak which were due to faradaic reactions at electrode/electrolyte as explained earlier in section 4.2.2.1. This was indication of battery type behavior of MWCNT─Co_3O_4 nanocomposites (Brousse *et al.*, 2015). The oxidation and reduction peak currents were augmented progressively with significant peak shift to the higher and lower potential respectively, by increasing the scan rates (3–50 mVs^{-1}). Moreover, the shape of the peaks was not distorted for all sample of MWCNT─Co_3O_4 nanocomposite, even at 50 mVs^{-1} which reveals the high electrochemical reversibility (Shah *et al.*, 2016).

Figure 4.29 displays the comparative CV curve of Co_3O_4 nanocubes and all samples of MWCNT─Co_3O_4 nanocomposites. For Co_3O_4 nanocubes well defined redox peaks with smaller current density were observed. However, in case of C1, C2, C3 and C4, the peak currents were increased gradually. This indicated that presence of MWCNT effectively increase the conductivity of the sample. Moreover, as the contents of MWCNT were increased from sample C1 to C4, the sharpness of the peak was increased respectively.

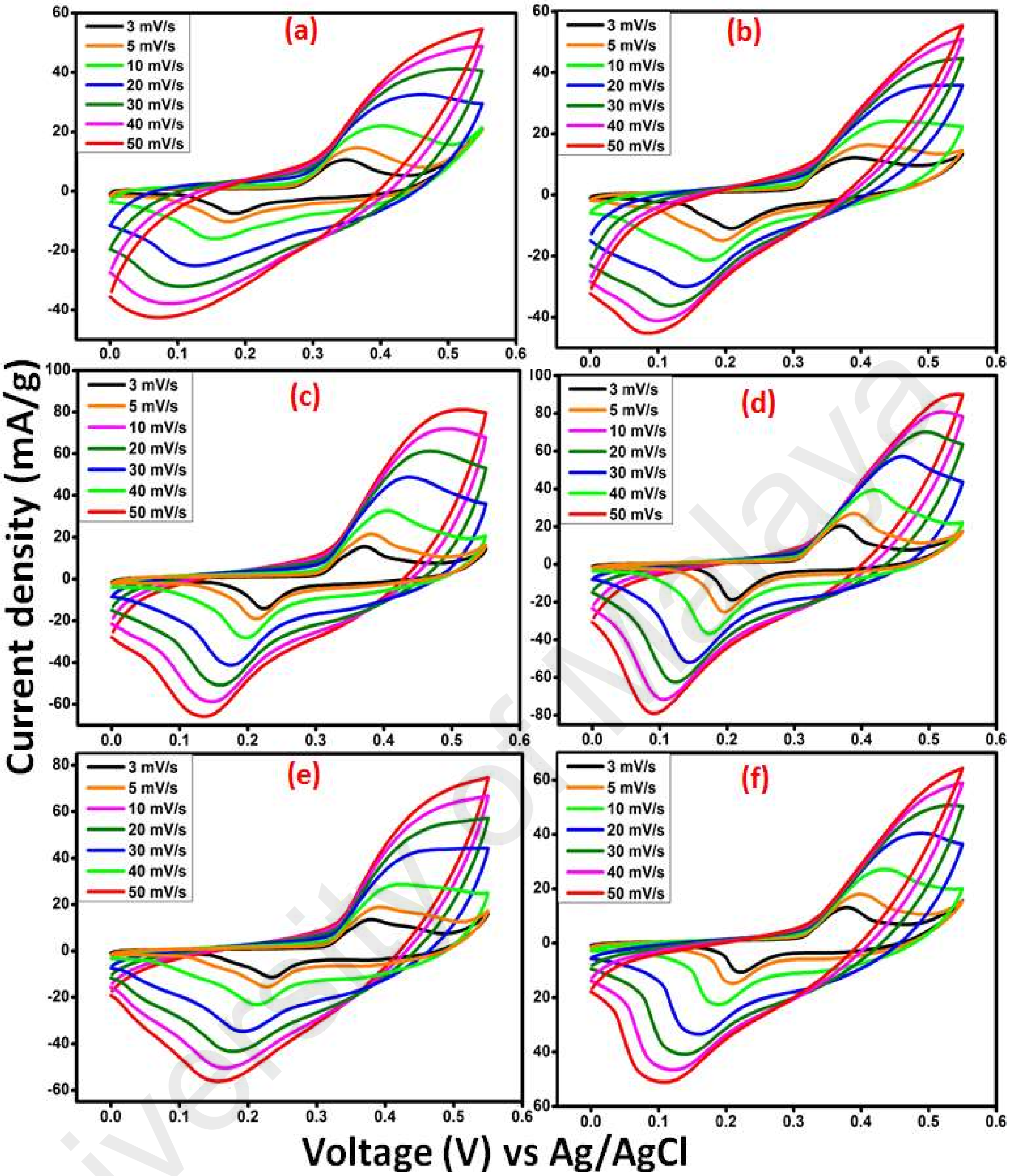

Figure 4.28: CV curves of (a) Co_3O_4 nanocubes, (b) C1, (c) C2, (d) C3, (e) C4 and (f) C5 at different scan rates (3 – 50 mVs^{-1}).

This suggests that MWCNTs provided platform for the uniform growth of Co_3O_4 nanocube which led to the enhancement of electrochemical surface area (as the contents of MWCNTs was increased). The redox peak current for C5 was reduced which was due to the higher amount MWCNT in C5, which covered most of Co_3O_4 nanocubes, resulting in the reduction of active sites for faradaic reaction (also confirmed by FESEM images). Hence CV results suggested that C4 was the optimized sample.

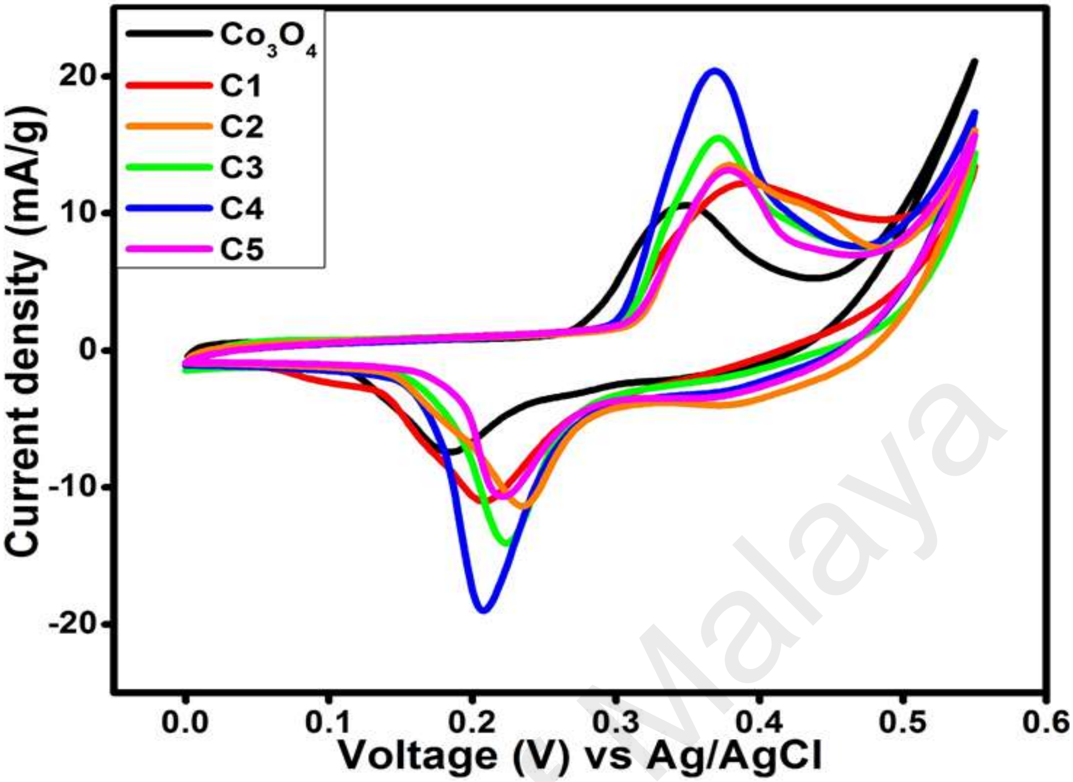

Figure 4.29: CV curves of Co_3O_4 nanocubes, C1, C2, C3, C4 and C5 at a scan rate of 5 mVs^{-1}.

4.4.2.2 Galvanostatic Charge Discharge

Figure 4.30 presents GCD curves of the Co_3O_4 nanocubes and all samples of MWCNT−Co_3O_4 nanocomposites. The charge/discharge curve for all of the samples consists of linear and non-linear part. The linear part at the start of charge and at the end of discharge curve was due to the charge storage due to the EDLC effect at electrode/electrolyte interface. Conversely, the non-linear part of charge discharge curve was due to faradaic reactions taking place at the electrode surface. This reveals that charge storage at electrode surface was due to the combination of both EDLC and faradaic reactions (Akinwolemiwa *et al.*, 2015). The specific capacity of the samples was found by equation 4.2. The maximum specific capacity was found to be 142.2 Cg^{-1} given by C4 followed by C3 (95.4 Cg^{-1}), C2 (88.2 Cg^{-1}), C5 (81.2 Cg^{-1}), C1 (75 Cg^{-1}) and Co_3O_4 nanocubes (67.6 Cg^{-1}) at a current density of 0.2 Ag^{-1}. By increasing the current density, the specific capacity of all the samples was decreased linearly (Figure 4.31). The specific capacity dropped below 50 % for almost all of the samples when current density was increased from 0.2 to 1 Ag^{-1}.

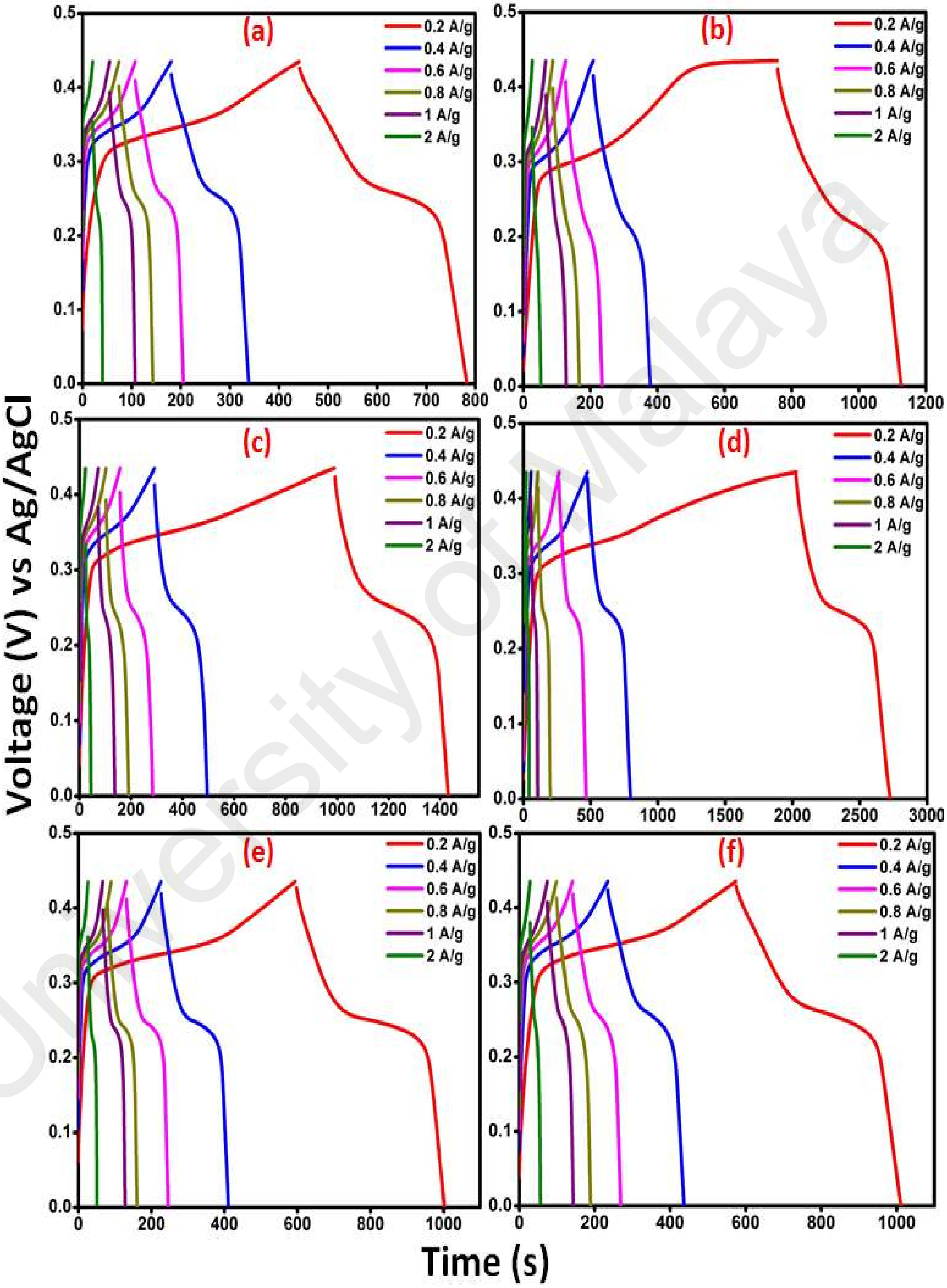

Figure 4.30: GCD curves of (a) Co_3O_4 nanocubes, (b) C1, (c) C2, (d) C3, (e) C4 and (f) C5 at different current densities (0.2–2 Ag^{-1}).

This indicates that the rate capability of the samples was not so good. Moreover, the specific capacity value was increased linearly by the increase in the contents of MWCNT, which was due to the less particle aggregations at elevated contents of MWCNT. But for C5, specific capacity dropped significantly due to the higher contents of MWCNT which bundled around Co_3O_4 nanocubes leading to block the electroactive cites for faradaic reactions. Therefore, C4 was chosen as optimized sample for further asymmetric assembly of supercapacitor in order to evaluate the performance of real time device study.

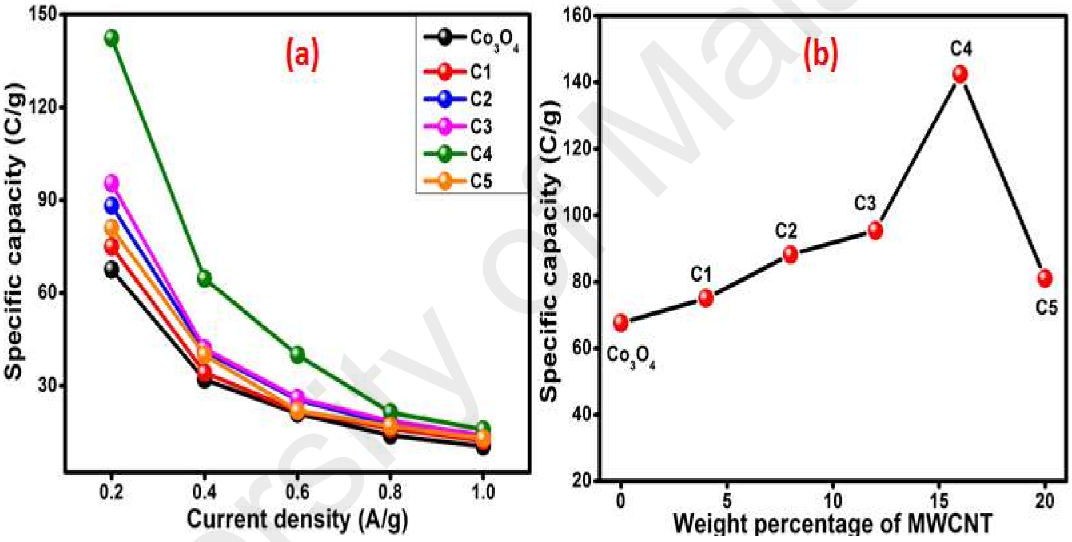

Figure 4.31: (a)Variation in specific capacity at different current densities (0.2, 0.4, 0.6, 0.8 and 1 Ag^{-1}) for Co_3O_4 nanocubes, C1, C2, C3, C4 and C5, (b) Comparison of specific capacity with respect to weigh percentage of MWCNT in C1, C2, C3, C4 and C5.

4.4.2.3 Electrochemical Impedance Spectroscopy

Figure 4.32 portrays the Nyquist plots of Co_3O_4 nanocubes and composites of MWCNT−Co_3O_4 (C1, C2, C3, C4 and C5). The starting intercept of EIS curve on X-axis at high frequency region is equivalence series resistance (ESR) which is offered by bulk electrolyte and related to the charge transfer between electrode and electrolyte (Zhong *et al.*, 2015). The ESR values of 2.68, 2.30, 2.22, 2, 1.55 and 1.06 were found for Co_3O_4 nanocubes, C1, C2, C3, C4 and C5, respectively (Figure 4.32(a, inset)). The value of ESR decreased systematically by increasing in the contents of MWCNT, which is clear indication of enhancement of conductivity of composites by at the higher contents of MWCNT. Furthermore, the diameter of semicircle (R_{ct}) in EIS for Co_3O_4 nanocubes based electrode is higher compared to its counter parts electrodes corresponding to the higher charge transfer resistance which was due to absence of MWCNT and high aggregations of nanocubes. Among MWCNT−Co_3O_4 nanocomposites, C1 displayed the smallest R_{ct}, suggesting its lowest charge transfer resistance. In addition to this, Wargburg impedance at low frequency region infers the capacitive behavior of the materials. Out of all nanocomposites C4 displayed the most vertical line parallel to the imaginary axis, indicates its low ion diffusion resistance and high capacitive behavior.

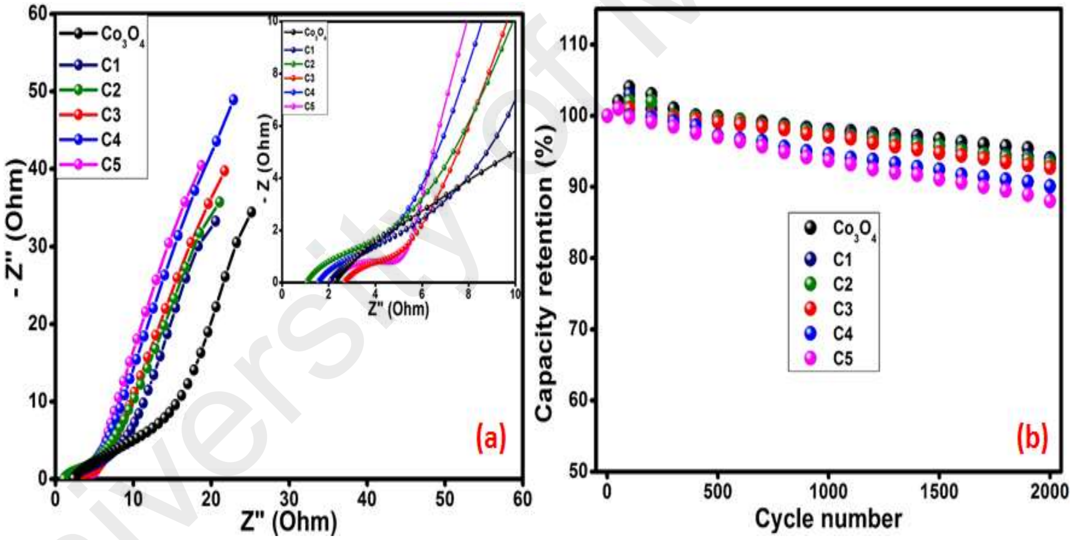

Figure 4.32: EIS spectra of Co_3O_4 nanocubes, C1, C2, C3, C4 and C5, (b) Life cycle test of Co_3O_4 nanocubes, C1, C2, C3, C4 and C5.

4.4.2.4 Asymmetric Supercapacitor Studies

(a) Cyclic Voltammetry

The high specific capacity (Q) and wider potential window (V) are two important factors which govern the power density and energy density of supercapacitor. In order to find out the maximum possible potential window for asymmetric supercapacitor, initially CV was performed for AC and C4 in standard three electrode cell system (shown in

Figure 4.33(a)). AC was chosen for negative electrode owing to its high conductive and high porous nature which makes it able to absorb more electrolyte ions, so that the operating voltage window can be extended (Halper *et al.*, 2006). Figure 4.33(c) shows the operating potential window of AC (0 to -1V) and MWCNT–Co_3O_4 nanocubes (0−0.55 V), which suggest the stable potential window of the device (labeled as MWCNT–Co_3O_4 nanocubes //AC) is 1.55 V (Figure 4.33(c)).

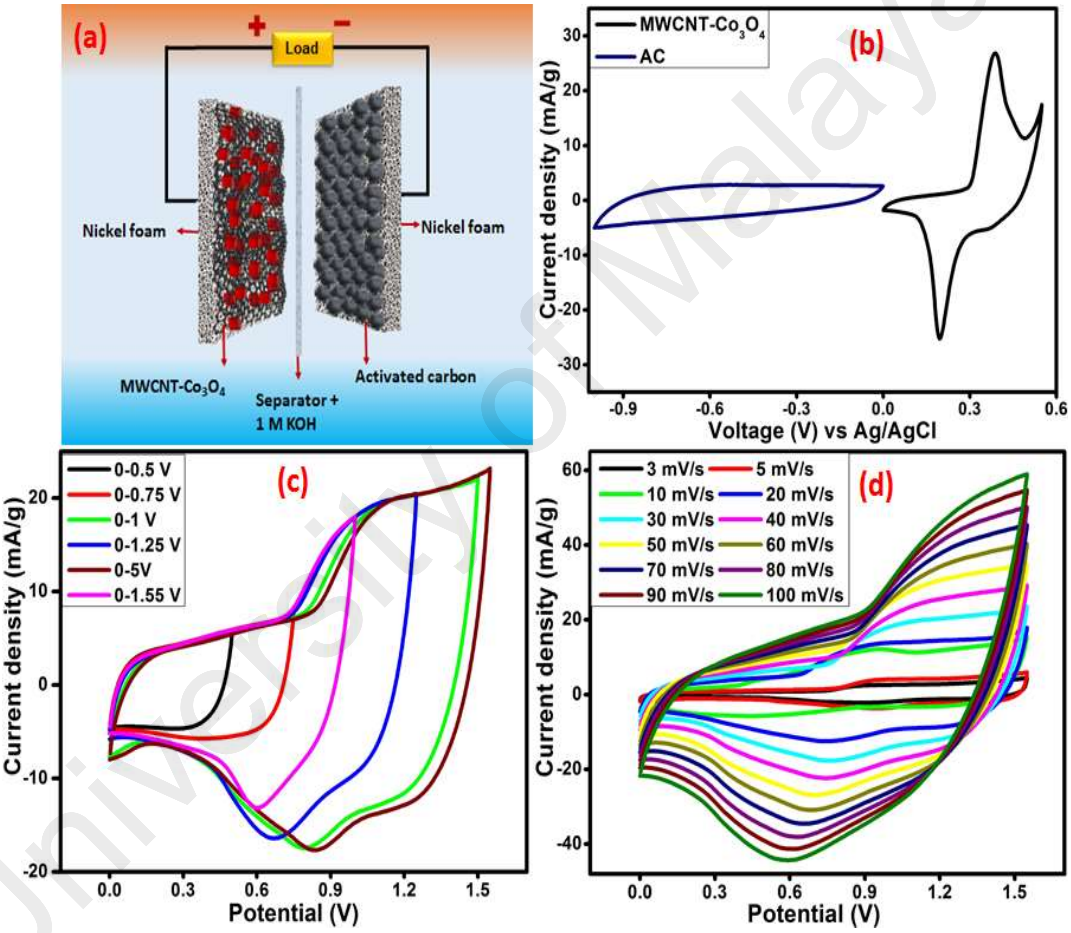

Figure 4.33: (a) Schematic assembly of MWCNT–Co_3O_4 nanocubes //AC supercapacitor (b) Comparative CV curves of MWCNT–Co_3O_4 nanocubes as a positive electrode and AC as a negative electrode performed at a scan rate of 10 mV s^{-1} in a three-electrode cell using 1 M KOH electrolyte, (c) CV of MWCNT–Co_3O_4 nanocubes //AC supercapacitor at different potential windows (d) CV of MWCNT−Co_3O_4 nanocubes//AC supercapacitor at different scan rates.

Figure 4.33(d) shows the CVs of the MWCNT−Co_3O_4 nanocubes//AC supercapacitor measured at different potential windows varying from 0.5 to 1.55 V at a scan rate of 30 mVs^{-1}. When the potential is 0.6 V, a weak oxidation peak and a strong reduction peak appeared which demonstrates that capacity was contributed from the faradaic reaction of C4. Figure 4.33(d) displays a quasi-rectangular CV curves at different scan rates. (5-50 mVs^{-1}). The presence of redox peaks manifest that specific capacity is not only contributed by EDLC effect from AC electrode but also due to the faradaic reaction taking place at MWCNT−Co_3O_4 nanocubes electrode. The CV shape is well retained even at high scan rate of 50 $mV.s^{-1}$ suggesting a good rate capability of the device (Figure 4.33(d)).

(b) Galvanostatic Charge Discharge

Figure 4.34(a) presents the GCD curves of MWCNT−Co_3O_4 nanocubes//AC supercapacitor at different potential windows (0.5–1.55 V) at a current density of 1 Ag^{-1}. A symmetric GCD curve was found until 0.75 V. Above 0.75 V, the charge curve remains the same but discharge curve shape was changed. In addition to this, IR drop at discharge curve was also increased at higher potential windows. Figure 4.34(b) depicts the GCD curves of MWCNT−Co_3O_4 nanocubes//AC supercapacitor within the current density from 0.3 to 0.6 Ag^{-1} in a potential window of 0–1.55 V. The discharge curve of the supercapacitor can be divided into two parts. Part one is a steep line at the start of discharge curve. This line discharge behavior was owing to the EDLC effect of the MWCNT−Co_3O_4 nanocubes//AC supercapacitor. The second non-linear part at end of discharge curve was due to pseudocapacitive behavior of the device. The curves of the device were almost symmetric at all current densities, indicating the excellent electrochemical performance of the device.

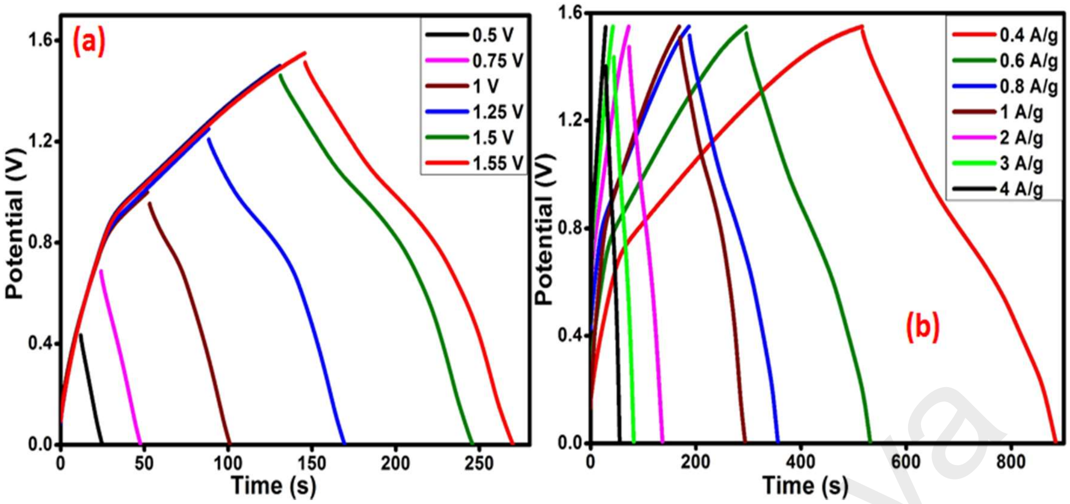

Figure 4.34: GCD curves of MWCNT−Co_3O_4 nanocubes//AC (a) at different potential windows and (b) at different current densities.

Table 4.4: Performance comparison of MWCNT−Co_3O_4 nanocubes//AC with reported works.

Material	Current density (Ag^{-1})	Power density ($W.kg^{-1}$)	Energy density ($Wh.kg^{-1}$)	Reference
Ni_3S_2/MWCNT-NC//AC	1	798	19.8	(Dai *et al.*, 2013)
NH_4CoNiP//HPC[1]	0.1	101	35.3	(Zhao *et al.*, 2016)
$NiCo_2O_4$–rGO/AC		324.9	23.3	(Wang *et al.*, 2012)
MWCNT−Co_3O_4 nanocubes//AC	0.2	309.85	19.28	This work
[1] hierarchical porous carbon				

It was found that the value of energy density decayed from 19.28 to 7.75 $Wh.kg^{-1}$, while the value of power density increased from 309.85 to 996.42 $W.kg^{-1}$ at current density of 0.2–6 Ag^{-1}. The maximum power density delivered by the supercapacitor was 996.42 $W.kg^{-1}$ with energy storage capacity of 7.75 $Wh.kg^{-1}$. These values are comparable to the reported work which are summarized in Table 4.4.

(c) Electrochemical Impedance Spectroscopy and Life Cycle Test

The charge transfer behavior and the intrinsic mechanism of the electrodes of supercapacitor device is further elucidated by EIS spectrum. Figure 4.35(a) presents the Nyquist plot of MWCNT−Co_3O_4 nanocubes//AC asymmetric supercapacitor device. The typical semicircle and straight line can be seen at low and high frequency regions, respectively. The ESR value (the first intercept of semicircle at real axis) was found to be 0.5 **Ω**, which is responsible of electrolyte and electrode resistance. The low value of ESR reveals the excellent conductivity with low internal resistance of electrodes of MWCNT−Co_3O_4 nanocubes//AC supercapacitor. The R_{ct} value lies at low frequency region (diameter of semicircle) is responsible for resistance electrolyte diffusion. The R_{ct} value was found to be 5.4 **Ω**. This value is not significant, which means that the electrodes of MWCNT−Co_3O_4 nanocubes//AC supercapacitor offers low charge transfer resistance electrolyte ions. In addition to this, the Warburg impedance deduced by the straight line originated from the OH^- diffusion within the electrode material. The MWCNT−Co_3O_4 nanocubes//AC supercapacitor exhibited almost vertical line parallel to the imaginary axis which indicates its high capacitive behavior.

The stability of the supercapacitor device over long term charge discharge cycle is an essential performance characterization which is important for the commercialization of the device. It was found that the capacity retention of assembled asymmetric supercapacitor remained more than 85 % at current density of 1 Ag^{-1} even after 3000 cycles. This results showed excellent stability of the device.

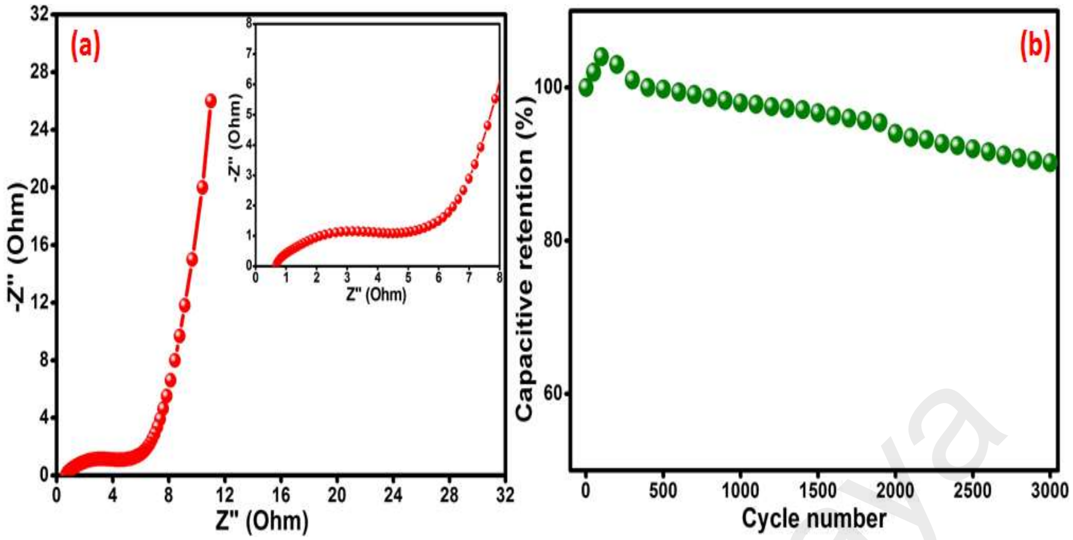

Figure 4.35: (a) EIS spectrum and (b) cycling stability of MWCNT−Co_3O_4 nanocubes//AC supercapacitor at current density of 1 Ag^{-1}.

4.4.3 Electrocatalytic Performance Study of MWCNT−Co_3O_4 nanocubes for Electrochemical sensing of DA

DA is highly electroactive in nature, so upon application of electric potential it easily gets oxidized to dopamine quinone (DAQ) by liberating electrons. A schematic illustration of the redox behavior of DA at the MWCNT−Co_3O_4 nanocomposite modified GCE is portrayed in Figure 4.36. During forward potential sweep, DA is oxidized to DAQ by releasing two electrons at modified electrode surface, while on reverse potential sweep DAQ is reduced back to DA. This exchange of electrons at modified electrode surface produce faradaic current.

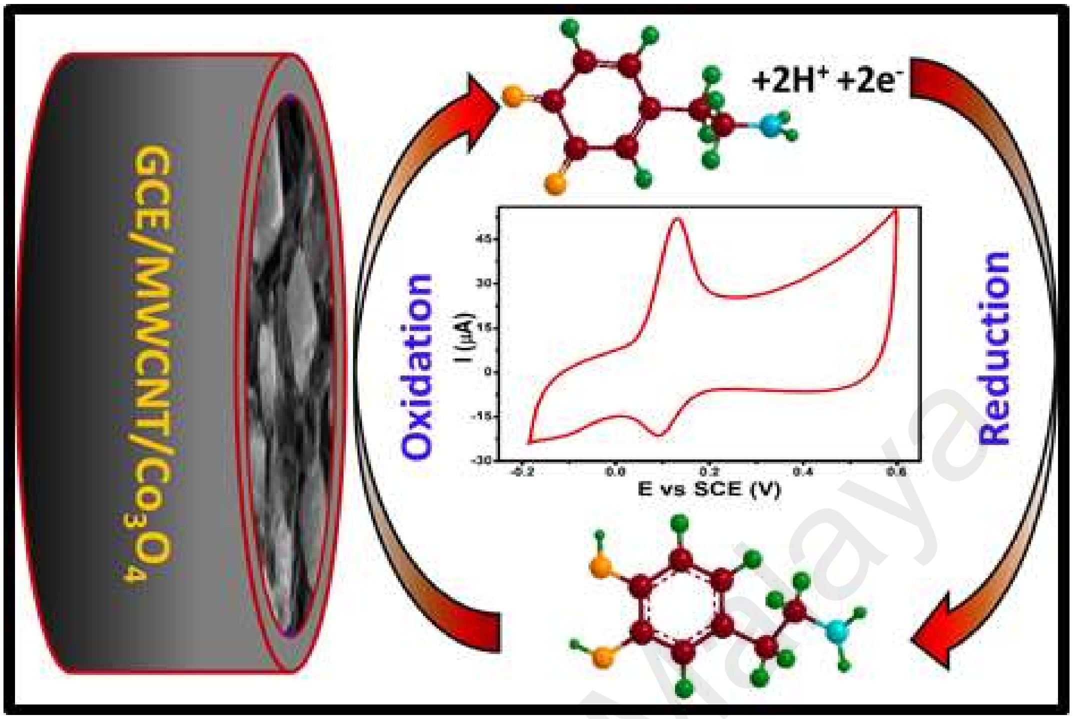

Figure 4.36: (a) Schematic representation of electroxidation of DA at MWCNT−Co_3O_4 nanocomposite modified GCE.

4.4.3.1 Cyclic Voltammetry

The charge transfer kinetics and electrocatalytic behavior of the sensors were examined by recording cyclic voltammograms (CV) responses in 0.1 M Phosphate buffer (pH ~ 7.2) at scan rate of 50 mVs^{-1} in the presence of 0.5 mM DA. Figure 4.37(a) shows the CVs of GCE modified with synthesized nanocomposites. Well defined redox peaks with anodic (E_{ap}) and cathodic (E_{cp}) peak at 210 and 40 mV respectively, with peak difference (ΔE) of 170 mV were shown by GCE. But upon modification of GCE with Co_3O_4 nanocubes, the peak potentials shifted to lower values leading to decrease in ΔE (150 mV) with improved redox peak current.

This confirmed the good catalytic activity of Co_3O_4 modified GCE towards DA. However, C1 modified GCE displayed noticeable shift in peak potentials to the low potentials with substantial enhancement in the current. The shift in peak potentials to the lower values can be attributed to the introduction of MWCNTs to Co_3O_4 nanocubes, which acted as highly conductive wires facilitating fast charge transfer kinetics. In addition, MWCNTs efficiently reduced the particle aggregations leading to the increase in effective electrochemical surface area resulting in the improvement of redox peak currents. Further improvement in redox peak currents together with shift in peak potentials to the lower potential was observed for C2, C3 and C4 modified GCE. But in case of C5, redox peak currents decreased significantly without any shift in peak potentials (Figure 4.37(a)).

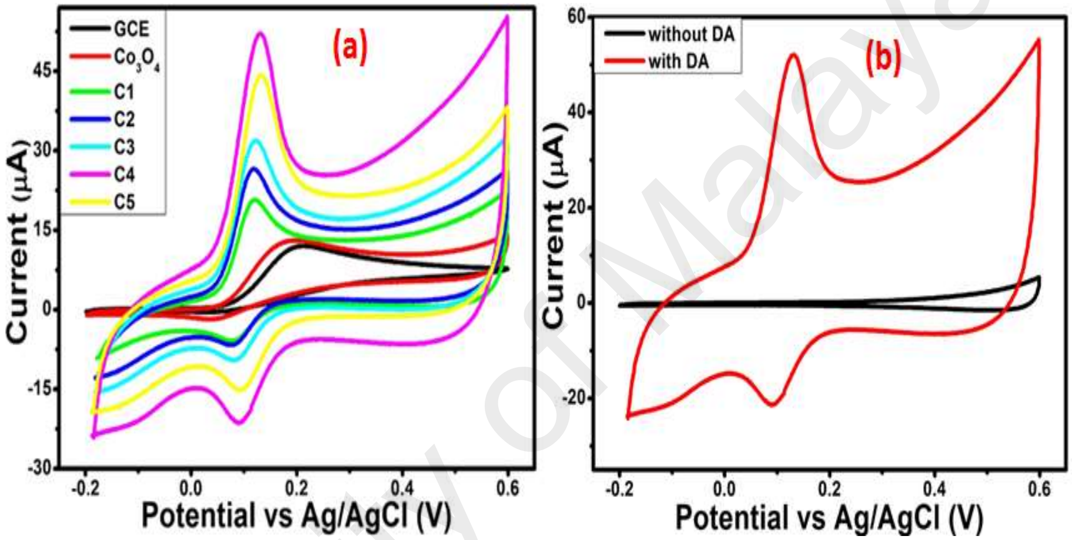

Figure 4.37: (a) CV curves obtained for bare GCE, Co_3O_4 nanocubes, C1, C2, C3, C4 and C5 nanocomposite modified GCE for 0.5 mM DA in 0.1 M PB (pH ~ 7.2) at a scan rate of 50 mV s^{-1} (b) Comparison of CV curves of MWCNT−Co_3O_4 nanocomposites (C4) modified GCE with and without 0.5 M DA in 0.1 M PB (pH ~ 7.2).

It is obvious that MWCNT−Co_3O_4 nanocomposite exhibited enhanced catalytic activity towards the electroxidation of DA compared to bare GCE and unsupported Co_3O_4 nanocubes. This revealed that MWCNTs in the composite MWCNT−Co_3O_4 played a vital role during electrocatalytic activity by providing conducting platform which accelerated charge transport kinematics. Improved electrocatalytic response was observed for C4 modified GCE in terms of oxidation current and peak potential. It exhibited 4.3 fold higher peak oxidation current with very small peak difference (ΔE ~ 37 mV) compared to bare GCE. However, in the absence of DA, C4 modified GCE did not give any current response (Figure 4.37(b)). The poor electrocatalytic response of C1, C2 and C3 was due to the high aggregations of Co_3O_4 nanocubes, as the contents of MWCNTs were insufficient for their uniform growth as discussed in section 4.4.1.4 (Figure 4.27(b), (c) and (d)). Ultimately, the less faces of Co_3O_4 nanocubes were exposed to the electrolyte resulting decrease in the electrochemical surface area. However, less exposure of Co_3O_4 nanocubes in C5 due to higher contents of MWCNTs which covered most of the Co_3O_4 nanocubes lead to the low catalytic response of C5 (Figure 4.27(f)). Thus, C4 was considered optimized composite for further studies.

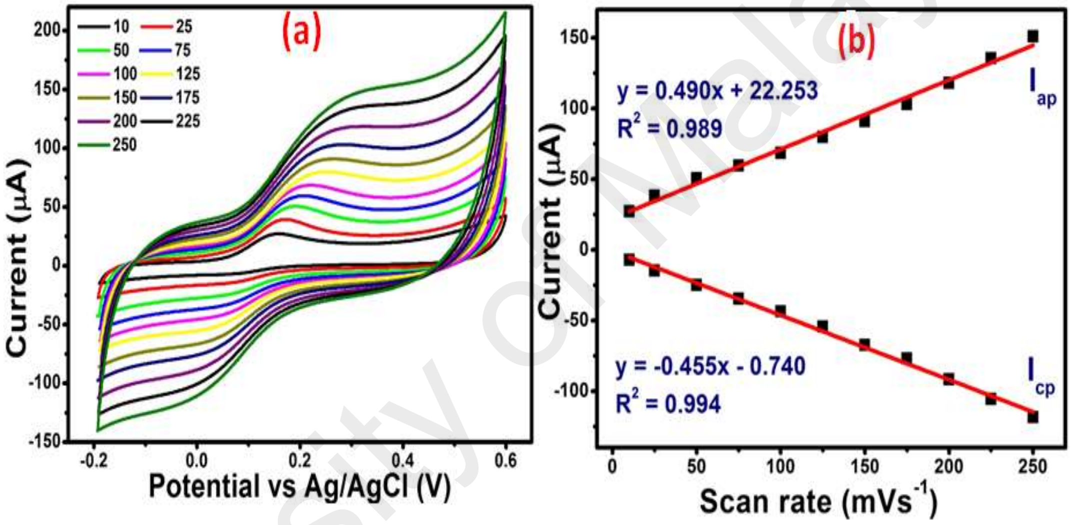

Figure 4.38: (a) CVs observed for MWCNT−Co_3O_4 nanocomposite in 0.1 M PB (pH 7.2) containing 0.1 mM DA at various scan rates, (d) the calibration plots of peak currents versus the scan rates.

The effect of scan rate on the electrocatalytic response of MWCNT−Co_3O_4 nanocomposite modified GCE towards DA oxidation was studied at different scan rate (from 10 to 225 mVs^{-1}) in 0.1 M Phosphate buffer (pH ~ 7.2) as background electrolyte (in the presence of 0.5 mM DA) using CV. Figure 4.38(a) depicts well defined redox peaks, which were enhanced with increasing scan rates. Both anodic (I_{ap}) and cathodic (I_{cp}) peak currents were increased linearly with increase in slight shift in peak potentials. The calibration plot (Figure 4.38(b)) of I_{ap} and I_{cp} with different scan rates showed a linear correlation (R^2 = 0.989 and 0.994), which confirmed that electron transfer reaction involved a surface-controlled process (Shahid *et al.*, 2015).

Figure 4.39(a) shows the electrocatalytic responses of MWCNT−Co_3O_4 nanocubes modified GCE at different molar concentrations of DA in 0.1 M of PB (pH ~ 7.2). Significantly, the oxidation peak current increased linearly with the addition of DA in the range of 0.5 to 5 mM and anodic peak potential underwent slightly positive shift (Figure 4.39(a)). The plot of peak current (I_{pa}) and different concentrations DA showed a linear plot with a slope value nearly equal to 1, which confirmed the electrochemical oxidation of DA follows the first order kinetics with respect to DA concentration at the C4 modified electrode (Figure 4.39(b)).

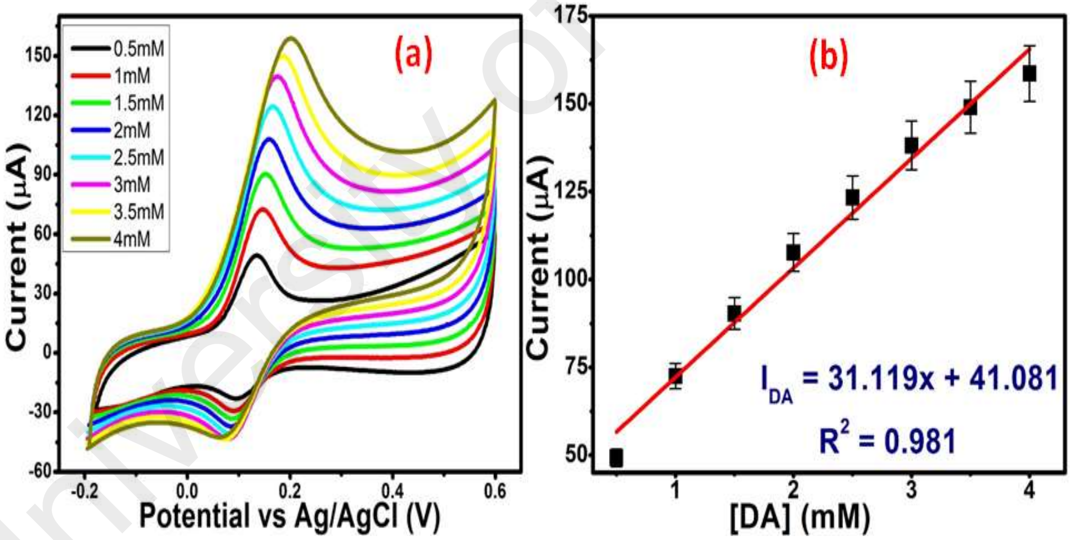

Figure 4.39: (a) CV curve obtained at the rGO−Co_3O_4 nanocomposite modified GCE with the successive addition of different concentrations of DA, (b) Plot of anodic peak current vs. molar concentration of DA.

4.4.3.2 Choronoamperometry

The CA curve technique is employed to detect the DA because it is a facile analytical technique which facilitates low concentration detection of analytes and is convenient to perform interference studies. In order to investigate the sensing capability of all modified electrodes, each electrode was run at a fixed potential (applied potentials were the peak potentials from Figure 4.40(a)) in homogeneously stirred 0.1 M PB (pH ~ 7.2) for the successive addition of 0.5 mM DA at a regular time interval of 60 s. Figure 4.40(a) displays the amperometric responses of the bare GCE and GCE modified with Co_3O_4 nanocubes, C1, C2, C3, C4, and C5. It is obvious, from Figure 4.40(a) that each electrode gave current response upon injection of 0.5 mM of DA. However, C4 modified GCE gave the highest current response which affirms the excellent oxidation capability of C4 towards DA. The enhanced electrocatalytic performance of C4 is attributed to the highly exposed Co_3O_4 nancubes on MWCNTs which lead to the augmentation of effective electrochemical surface area. These results are in good agreement to the aforementioned CV results discussed in section 4.4.3.1. Moreover, the calibration plots for the current response versus concentration values ranging from 0.5 to 5 mM showed linear relationship for all modified electrodes (Fig. 4.40(b)).

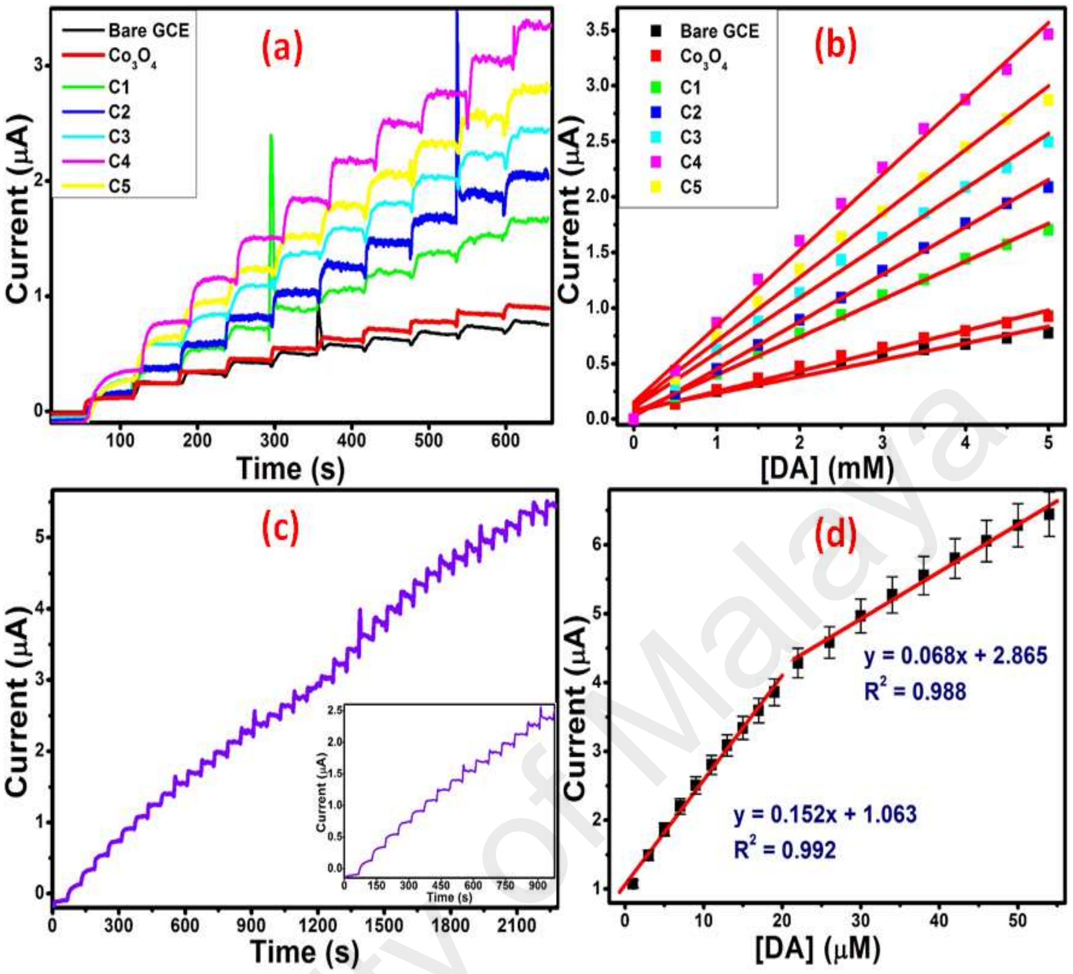

Figure 4.40: (a) Amperometric i–t curves obtained at bare GCE, Co_3O_4 nanocubes, C1, C2, C3, C4 and C5 modified GCE for the successive addition of 0.5 mM of DA in 0.1 M PB (pH ~ 7.2) at a regular interval of 60 s, (b) corresponding calibration plots of current versus concentration of DA. Applied potentials were the peak potentials obtained from Fig. 4b, (c) Amperometric i–t curve of MWCNT−Co_3O_4 nanocomposite (C4) modified GCE for the successive addition of 1 mM DA in 0.1 M PB (pH 7.2) at an applied potential of +0.13 V with a regular interval of 60 s and (d) corresponding calibration plots of current versus concentration of DA.

In order to calculate the LOD, repeated measurements were performed at low concentrations for C4 modified GCE. Figure 4.40(c) depicts the amperometric response curve for C4 modified GCE for the successive addition of DA with different concentrations in 0.1 M PB (pH ~ 7.2) at an applied potential of + 0.13 V. First, twenty spikes of 1 μM and then twenty spikes of 2 μM of DA were used to record the current. Upon each injection of DA with a sample interval of 60 s, C4 modified GCE gave significant current response. Figure 4.40(d) shows the calibration plot of amperometric current response at different concentrations of DA. It is noticeable that calibration plot displayed two separate linear segments corresponding to the two different concentration ranges of DA. The first linear segment of calibration plot correspond to the first concentration range of DA from 1 to 20 µM (20 injections with each injection of 1 µM) with a correlation coefficient of 0.992 (n = 20). The second linear segment is attributed to the second concentration range of DA from 20 to 60 (20 injections with each injection of 2 µM) with a correlation coefficient of 0.988 (n = 20). The current response was decreased even at higher concentrations of DA due to kinetic limitations of C4 modified electrode. Hence, lower range was used to estimate the performance parameters for the sensor (How *et al.*, 2014). The LOD and LOQ were estimated to be 0.176 µM and 0.573 µM respectively, by using the standard deviation (SD) of the y-intercepts and the slope of the regression lines of lower range (S), (LOD = 3.3(SD/S) and LOQ = 10(SD/S)) (Jayabal *et al.*, 2013). The sensitivity of modified electrode is found to be 0.151 $\mu A \mu M^{-1}$. These results suggest that the fabricated MWCNT─Co_3O_4 nanocubes sensor demonstrated enhance catalytic performance in terms of low LOD, wider linear range and good sensitivity towards DA detection. The comparison of the electrocatalytic performance of the MWCNT─Co_3O_4 nanocube modified GCE with some of the reported GCE based electrochemical sensors for the detection of DA is summarized in Table 4.5. The developed sensor showed better performance in terms of LOD, sensitivity and linear range compared to the reported works.

Table 4.5: Performance comparison of reported electrochemical sensors for DA detection.

Type of Electrode	**Method**	**pH**	**LOD (µM)**	**LOQ (µM)**	**Linear range (µM)**	**Sensitivity (µAµM-1)**	**Reference**
GNB (Graphene nanobelts)	CA	7.0	0.58	1.95	2-202	0.95	(Kannan *et al.*, 2016)
Graphene/SnO$_2$/GCE	DPV	6.8	1	-	0-100	-	(Nurzulaikha *et al.*, 2015)
GNS-Bi	CA	7	0.35	5.30	1-30	5.304	(Mani *et al.*, 2015)
HNP-AuAg (Hierarchical nanoporous)	CA	7.0	0.2	-	5-335	-	(Hou *et al.*, 2016)
Pt–Gr–CNT	DPV	7.0	9.199	-	0.2-30	-	(Ramakrishnan *et al.*, 2015)
rGO–Co$_3$O$_4$ nanocomposite/ GCE	CA	7.2	0.277	0.924	0-30	0.389	(Numan *et al.*, 2017)
V$_2$O$_5$@PANI/GCE	CA	Nil	0.39	130	6.6-110	-	(Suresh *et al.*, 2014)
ERGO/GCE	DPV	7	0.5	-	0.5-60	0.482	(Yang *et al.*, 2014)
MWCNT─Co$_3$O$_4$/GCE	CA	7.2	0.176	0.573	0-20	0.151	Present work

4.4.3.3 Interference Studies

During electrochemical sensing of an analyte, it is important for the sensor to detect the target molecule selectively without producing any interfering current response. The AA and UA are the two important interfering agents which coexist with DA. Therefore, it is very important to evaluate the detection capability of a DA sensor in the presence of AA and UA. The selectivity of the MWCNT−Co$_3$O$_4$ nanocubes based sensor for the detection of DA was examined in the presence of different interferents like UA, AA, glucose, and urea by using CA. Usually, square wave voltammetry (SWV) and differential pules voltammetry (DPV) are employed to evaluate the selectivity of a DA in the presence of UA and AA. But in the case of CA, the selectivity of DA can be evaluated even in the presence of higher number of potential interferents such as UA, AA, glucose, urea and NaCl etc. In addition to this, oxidation potential of DA is very close to AA and UA, so it is very difficult to get separated and well defined oxidation peaks for each analyte. However these problems are avoided in CA.

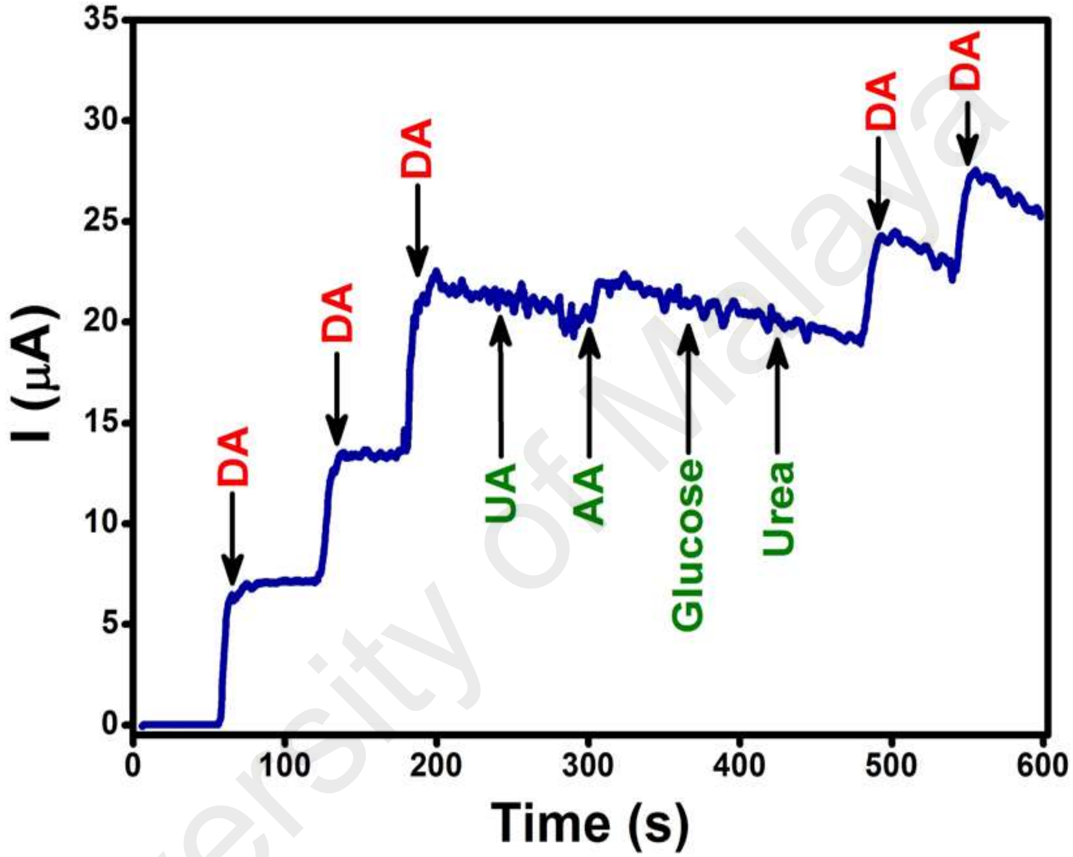

Figure 4.41: Amperometric i–t curve of MWCNT−Co_3O_4 nanocomposite modified GCE for the successive addition of DA and interfering species each of 0.5 mM in 0.1 M PB at a regular interval of 60 s. The applied potential was + 0.13 V.

Figure 4.41 depicts the recorded amperometric i–t curve response for the consecutive additions of DA and interferents in a homogeneously stirred 0.1 M Phosphate buffer at a constant applied potential of + 0.13 V. Three consecutive injections of DA (each of 0.5 mM) were used at the start and it was found that each injection gave significant current response. After this, UA, AA, glucose and urea were injected respectively, with the sample time of 60 s. However, no obvious increase in current response was observed for all interfering species except AA even at fifty fold higher concentration then DA. Compared to DA, only 12 % current response was observed for AA which indicates that the signal of DA is much stronger compared to AA. These results revealed that the sensor possesses good selectivity towards the quantitative determination of DA even in the presence of common physiological interferents.

4.4.3.4 Real Time Sample Test

In order to evaluate the performance and reliability of the sensor in real application, analytical determination of DA in two urine samples was performed using standard addition method. The analytical results are summarized in Table 4.6. To ascertain the accuracy of the results, different concentrations of DA were added in urine containing Phosphate buffer and detected. The recovery of spiked sample ranged between 99.1 to 104 %, which is indication of the successful application of rGO−Co_3O_4 nanocomposite for the detection of DA.

Table 4.6: Analytical results of DA detection by using MWCNT−Co_3O_4 nanocomposite in real urine samples (n = 3).

Urine sample	**Add concentration (µM)**	**Found Concentration (µM)**	**RSD (%)**	**Recovery (%)**
Sample 1	1	1.04	1.46	104.00
	5	5.30	1.06	106.00
	10	10.05	0.40	100.05
Sample 2	1	1.07	2.43	107.00
	5	4.87	1.54	97.40
	10	9.91	0.66	99.10

4.4.3.5 Stability and Reproducibility

For the stability study of the sensor, CV response of C1 modified GCE was recorded for DA in a range between -0.2 and 0.6 V at a scan rate of 50 mVs^{-1}. The CV response was recorded on after every two days with in two weeks. The peak current was considered as a factor for indicating the stability of the modified electrode. Here, I is the current response of fresh sensor and I_0 is the current response after storage as shown in Figure 4.42(a). A 16.7 % decrease in the anodic peak current with slight shift in peak potential was observed after two weeks. This revealed that C4 modified GCE can also withstand being stored in the solution for a period of time (two weeks) and the electrocatalytic performance remain almost unchanged, which confirms that modified electrode is very stable and reproducible for the detection of DA.

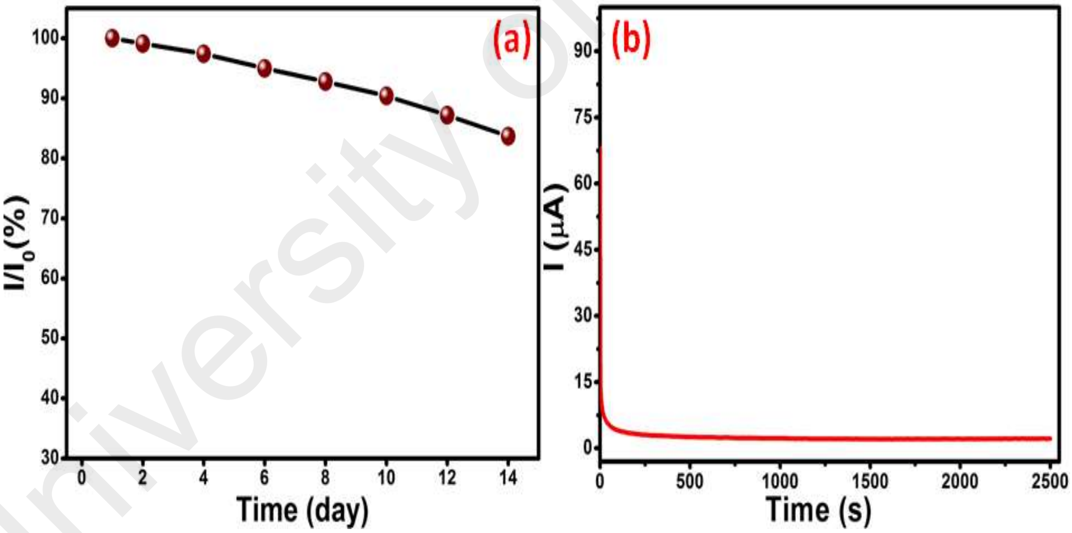

Figure 4.42: (a) Stability of the proposed sensor stored at ambient conditions over 14 days using 0.1 M PB (pH ~ 7.2), (b) CA response of C4 modified GCE in 0.1 M PB (pH ~ 7.2) containing 0.5 mM DA at constant potential of + 0.13 V for 2500 s.

Additionally, operational stability of MWCNT─Co_3O_4 nanocubes modified GCE was also evaluated by performing CA in 0.1 M PB containing 0.5 mM DA at a constant potential of + 0.13 V for 2500 s. A very stable current response was observed and only 7.32 % decay in the current was observed after 2500 s (Figure 4.42(b). This confirms the excellent operational stability of modified GCE.

4.5 Performance Comparison of the Developed Nanocomposites

4.5.1 rGO─Co_3O_4 nanocubes Vs MWCNT─Co_3O_4 nanocubes for Supercapacitor

The electrochemical performance of rGO─Co_3O_4 nanocubes and MWCNT─Co_3O_4 nanocubes for supercapacitor are summarized in Table 4.7. It is evident that, MWCNT─Co_3O_4 nanocubes demonstrated superior electrochemical energy storage performance compared to rGO─Co_3O_4 nanocubes in terms of specific capacity (Q_s) and energy density (E). This means that MWCNT─Co_3O_4 nanocubes can deliver stored energy to the load for long duration. However, the power density (P) of rGO─Co_3O_4 nanocubes was found to be higher than MWCNT─Co_3O_4 nanocubes, manifesting that rGO─Co_3O_4 nanocubes is suitable nanocomposite for energy storage applications especially where high spikes of power are required.

The higher value of Q_s and E of MWCNT─Co_3O_4 nanocubes compared to rGO─Co_3O_4 nanocubes is attributed due to the following factors:

- CNTs are highly porous in nature due to which they offer more area to OH^- to interact with the active sites of material. Therefore, more faradaic reactions can takes place resulting in higher Qs and E. However, rGO is not porous so OH^- can interact only to the top surface of the material.
- rGO is in the form of sheets which covered most of the Co_3O_4 nanocubes. These intercalated nanocubes cannot participate in the faradaic reactions resulting in less electrochemical performance for energy storage. But in case

of MWCNT─Co_3O_4 nanocubes, there are voids where electrolyte can diffuse and undergo faradaic reaction

- It is very difficult to produce single layer of rGO, which means not all the electrochemical surface area of rGO can be utilized.
- As Faradaic reactions were more dominant in the MWCNT─Co_3O_4 nanocubes compared to rGO─Co_3O_4 nanocubes therefore, MWCNT─Co_3O_4 nanocubes gave energy density compared to rGO─Co_3O_4 nanocubes. At the same time, rGO (which is carbonaceous material) was exposed more to electrode in rGO─Co_3O_4 nanocubes compared to MWCNT─Co_3O_4 nanocubes, therefore it gave high power density due dominant EDL effect.

Table 4.7: Performance comparison of rGO─Co_3O_4 nanocubes VS MWCNT─Co_3O_4 nanocubes as electrode material for supercapacitor.

Material	Q_s (Cg^{-1})	P ($W.kg^{-1}$)	E ($Wh.kg^{-1}$)	Capacity Retention (%)
rGO─Co_3O_4 nanocubes	125	996.4	7.75	91.4
MWCNT─Co_3O_4 nanocubes	147	309.57	28.88	90.2

4.5.2 rGO─Co_3O_4 nanograins Vs MWCNT─Co_3O_4 nanocubes for Electrochemical Sensors

The performance parameters of rGO─Co_3O_4 nanograins and MWCNT─Co_3O_4 nanocubes as electrochemical sensing material for DA are summarized in Table 4.8. The sensing ability of MWCNT─Co_3O_4 nanocubes was higher than rGO─Co_3O_4 nanograins as it shows low LOD, higher limit of quantification and good sensitivity. However, MWCNT─Co_3O_4 nanocubes demonstrated poor selectivity during the detection of DA. On the other hand, rGO─Co_3O_4 nanograins displayed excellent selectivity on the cost of slightly higher LOD. Selectivity is vitally important parameter for electrochemical sensor in order to detect target molecule in the presence of common physiological analytes. Therefore, poor selectivity of a sensor cannot be compromised on the LOD. Hence, rGO−Co_3O_4 nanograins is considered better sensor for DA compared to MWCNT−Co_3O_4 nanocubes.

Table 4.8: Performance comparison of rGO−Co_3O_4 nanocubes vs. MWCNT−Co_3O_4 nanocubes as electrochemical sensors.

Material	**LOD (µM)**	**Linear range (µM)**	**Sensitivity (µAµM^{-1})**	**LOQ (µM)**	**Selectivity**
rGO−Co_3O_4 nanocubes	0.277	0−30	0.389	0.924	Good
MWCNT−Co_3O_4 nanocubes	0.176	0−20	0.151	0.573	Poor

CHAPTER 5: CONCLUSIONS AND FUTURE WORK

5.1 Conclusions

Carbon matrix supported cobalt oxide (Co_3O_4) nanostructures are successfully synthesized by single step hydrothermal route. Their complete structural, morphological and compositional characterizations were carried out. The synthesized nanocomposites were evaluated for energy storage and electrochemical sensing applications. Overall, three different nanocomposites were prepared which are based on rGO, MWCNT and Co_3O_4 nanostructures.

In system one, the effect of different molar concentrations of cobalt precursor-based rGO–Co_3O_4 nanocubes were studied on the morphology and electrochemical performance of supercapacitor. Different molar concentrations of Co_3O_4 nanocubes intercalated rGO were synthesized using a hydrothermal method. Surface morphology of the composite materials revealed the uniform distribution of Co_3O_4 on the rGO matrix with an average particle size of 45 nm. The maximum specific capacity of 125 Cg^{-1} in three electrode cell system was observed in A2. The high specific capacity was attributed to the lower charge transfer resistance than that of its counterpart electrodes materials because of effective ion transfer and fewer particle aggregations on rGO matrix. Moreover, A2 exhibited long-term cyclic stability of 91.6 % over 2000 cycles with good reversibility. Additionally, the fabricated (rGO–Co_3O_4 nanocubes//AC) hybrid supercapacitor device can be cycled reversibly at a cell voltage of 1.55 V, which exhibited excellent electrochemical performances with a power density of 996.4 $W.kg^{-1}$ and an energy density of 7.75 $Wh.kg^{-1}$. It also demonstrated a superior life cycle more than 90 % capacity retention after 3000 cycles. These results demonstrate that controlling the molar concentration of cobalt precursor-based Co_3O_4 with rGO composite has potential in development of electrode materials for energy storage applications.

In system two, rGO–Co_3O_4 nanograins were synthesized by hydrothermal route and were optimized by varying the contents of rGO such as 5.7, 7.4, 9.1 and 10.7 wt. %, which were denoted as B1, B2, B3 and B4, respectively. The crystallinity of rGO–Co_3O_4 nanograins is examined by XRD. Raman spectrum revealed the successful reduction of GO into rGO. The surface morphology revealed that the granular shaped Co_3O_4 were decorated on rGO matrix with the average particle size of ∼35 nm. For electro-chemical oxidation of DA, GCE was modified with nanocomposites and it was found that B3 modified GCE showed enhanced electrocatalytic performance in terms of peak catalytic current and shift in over potential when compared to those of B1, B2 and B4 modified GCE. The LOD was found to be 0.277 μM with S/N ratio of 3 with quantitative limit of 0.924 μM using the amperometric i–t curve technique. In addition, the B3 modified GCE displayed good selectivity for the detection of DA in the presence of a 100-fold higher concentration of uric acid, glucose and AA. The developed sensor also demonstrated excellent reproducibility in real time urine sample. The sensor studies suggested that 3D rGO–Co_3O_4 nanograins endow excellent catalytic activity, high selectivity and sensitivity towards DA.

In third and last system, composites containing cobalt oxide (Co_3O_4) nanocubes integrated with MWCNT were synthesized by a hydrothermal route. The prepared nanocomposites were employed for supercapacitor and electrochemical sensing application. The fractions of MWCNTs in the composites were varied from 4, 8, 12, 16 and 20 wt. %, and the resulting materials are denoted as C1, C2, C3, C4 and C5, respectively. The formation of products with high structural crystallinity was confirmed by XPS, Raman spectroscopy and XRD. A morphological study by FESEM and HRTEM showed the successful integration of Co_3O_4 nanocubes to the MWCNTs with an average particle size of ∼32 nm. Supercapacitor studies revealed that C4 gave the highest specific capacity (147 $C.g^{-1}$) in three electrode cell system compared to its counterpart nanocomposites. The high specific capacity was attributed to the optimized contents of MWCNT which provided platform for the uniform growth of Co_3O_4 nanocubes leading to high electrochemical surface area and lower charge transfer resistance. Additionally, C4 exhibited long-term cyclic stability of 90.2 % over 2000 cycles with good reversibility. The hybrid supercapacitor (MWCNT–Co_3O_4 nanocubes//AC) was fabricated in order to evaluate the performance of optimized nanocomposite (C4) for real time supercapacitor device. The CV results showed that MWCNT–Co_3O_4 nanocubes//AC device can be cycled reversibly at a cell voltage of 1.55 V. The fabricated hybrid supercapacitor demonstrated excellent electrochemical performances with a power density of 309.5 $W.kg^{-1}$ and an energy density of 31.6 $Wh.kg^{-1}$. It also exhibited superior life cycle more than 90 % capacity retention after 3000 cycles.

In order to investigate the performance of the MWCNT–Co_3O_4 nanocubes for electrochemical sensing DA, the surface of a GCE was modified with the MWCNT–Co_3O_4 nanocubes. CV results showed that the C4-modified GCE displayed the best performance in terms of oxidation potential and peak current in comparison to that of a bare GCE, Co_3O_4 nanocubes, or GCE modified with C1, C2, C3 or C5. The detection limit (at an S/N ratio of 3) was found to be 0.176 μM by using CA, and the linear range was between 1 and 20 μM. Additionally, developed sensor showed excellent performance in real time urine sample.

In conclusion, the electrochemical performance of rGO−Co_3O_4 nanostructures (nanocubes and nanograins) and MWCNT−Co_3O_4 nanocubes is evaluated for supercapacitor and electrochemical sensing applications. Overall, MWCNT−Co_3O_4 nanocubes showed better performance for supercapacitor application in terms of specific capacity and energy density compared to rGO−Co_3O_4 nanocubes. The higher energy storage ability of MWCNT−Co_3O_4 nanocubes was due to the high porous nature of

MWCNT where electrolyte ions can access more active sites of electrode material for redox reactions. In rGO−Co_3O_4 nanocubes, bigger rGO sheets covered most of the Co_3O_4 nanocubes which lead to the less exposure of Co_3O_4 nanocubes to the electrolyte resulting less redox reaction for energy storage.

However, the performance of rGO−Co_3O_4 nanograins for electrochemical detection of DA was more promising compared to MWCNT−Co_3O_4 nanocubes. Although, MWCNT−Co_3O_4 nanocubes gave less LOD but its recognition of target molecule was poor due to the overlapping potentials of target and interfering molecules. But, rGO−Co_3O_4 nanograins selectively detect the target molecule even in presence of 100 folds higher concentration of interfering species. The high selectivity of the rGO−Co_3O_4 nanograins was due to the high conductivity of the rGO compared to MWCNT. Due to high conductivity, the oxidation potentials of target and interfering molecules were separated.

In summary, MWCNT−Co_3O_4 nanocubes is good candidate for energy storage while rGO−Co_3O_4 nanograins is excellent candidate for electrochemical sensing applications.

5.2 Future Work

In this work, the performance of rGO−Co_3O_4 nanocubes was evaluated for energy storage application. However, it is expected that it can also provide good performance for electrochemical sensing of bioanalytes. Similarly, rGO−Co_3O_4 nangrains was evaluated for electrochemical sensing of DA, but its energy storage capability can also be evaluated. Therefore, in future, rGO−Co_3O_4 nanocubes can be exploited for electrochemical sensing of bioanalytes (DA, UA, AA, glucose e.t.c.), while rGO−Co_3O_4 nangrains can be investigated for energy storage application.

Graphene is outstanding candidate for electrochemical applications due to its ballistic conductivity and excellent electrochemical surface area. But it is very difficult to utilize the full electrochemical surface is due to the stacking nature of its 2D sheets. However, if the sheets of graphene can be separated as single or even double layer, then its maximum features can be utilized. In addition to this, the bigger sheets of graphene most of the time cover metal oxide nanoparticles leading to less exposure of the catalyst nanoparticles to the analyte/electrolyte.

In future studies, sonochemical synthesis (using horn sonicator) technique can be used to exfoliate the sheets of graphene to obtain single or double layer of graphene sheet. Hence most of the electrochemical surface area of graphene can be utilized. The horn sonicator can effectively tear bigger graphene sheets to micro size graphene sheets which results in less intercalation and more exposure of catalyst nanoparticles. Additionally, sonication will induce more edges sites of graphene which are more active for electrochemical reactions compared to basal plan. This can significantly enhance the electrochemical activity of the graphene.

REFERENCES

Abdelwahab, A. A., & Shim, Y.-B. (2015). Simultaneous determination of ascorbic acid, dopamine, uric acid and folic acid based on activated graphene/mwcnt nanocomposite loaded au nanoclusters. *Sensors and Actuators B: Chemical, 221*, 659-665.

Abouali, S., Akbari Garakani, M., Zhang, B., Xu, Z.-L., Kamali Heidari, E., Huang, J.-q., Huang, J., & Kim, J.-K. (2015). Electrospun carbon nanofibers with in situ encapsulated co_3o_4 nanoparticles as electrode for high performance supercapacitors. *ACS Applied Materials & Interfaces, 7*(24), 13503-13511.

Akinwolemiwa, B., Peng, C., & Chen, G. Z. (2015). Redox electrolytes in supercapacitors. *Journal of the Electrochemical Society, 162*(5), A5054-A5059.

Amoruso, S., Ausanio, G., Bruzzese, R., Vitiello, M., & Wang, X. (2005). Femtosecond laser pulse irradiation of solid targets as a general route to nanoparticle formation in a vacuum. *Physical Review B, 71*(3), 033406.

An, K. H., Kim, W. S., Park, Y. S., Moon, J.-M., Bae, D. J., Lim, S. C., Lee, Y. S., & Lee, Y. H. (2001). Electrochemical properties of high-power supercapacitors using single-walled carbon nanotube electrodes. *Advanced Functional Materials, 11*(5), 387-392.

Ando, Y., Zhao, X., Shimoyama, H., Sakai, G., & Kaneto, K. (1999). Physical properties of multiwalled carbon nanotubes. *International Journal of Inorganic Materials, 1*(1), 77-82.

Aurora, R., Kristo, D., Bista, S., & Rowley, J. (2012). Zak rs; casey kr; lamm ci; tracy sl; rosenberg rs. The treatment of restless legs syndrome and periodic limb movement disorder in adults—an update for 2012: Practice parameters with an evidence-based systematic review and meta-analyses. *Sleep, 35*(8), 1039-1062.

Babu, S. S., Möhwald, H., & Nakanishi, T. (2010). Recent progress in morphology control of supramolecular fullerene assemblies and its applications. *Chemical Society Reviews, 39*(11), 4021-4035.

Banerjee, S., Hemraj-Benny, T., & Wong, S. S. (2005). Covalent surface chemistry of single-walled carbon nanotubes. *Advanced Materials, 17*(1), 17-29.

Banerjee, S., Naha, S., & Puri, I. K. (2008). Molecular simulation of the carbon nanotube growth mode during catalytic synthesis. *Applied Physics Letters, 92*(23), 233121.

Becker, H. I. (1957). Low voltage electrolytic capacitor: Google Patents, U.S. 2,800,616.

Boos, D. L. (1970). Electrolytic capacitor having carbon paste electrodes: Google Patents, 3,536,963.

Brousse, T., Bélanger, D., & Long, J. W. (2015). To be or not to be pseudocapacitive? *Journal of the Electrochemical Society, 162*(5), A5185-A5189.

Brusso, B., & Chaparala, S. (2014). The evolution of capacitors [history]. *IEEE Industry Applications Magazine, 20*(6), 8-12.

Cao, G., & Wang, Y. (2004). *Nanostructures and nanomaterials: Synthesis, properties, and applications*: World Scientific.

Chabot, V., Higgins, D., Yu, A., Xiao, X., Chen, Z., & Zhang, J. (2014). A review of graphene and graphene oxide sponge: Material synthesis and applications to energy and the environment. *Energy & Environmental Science, 7*(5), 1564-1596.

Chan, W. C., Maxwell, D. J., Gao, X., Bailey, R. E., Han, M., & Nie, S. (2002). Luminescent quantum dots for multiplexed biological detection and imaging. *Current Opinion in Biotechnology, 13*(1), 40-46.

Chang, W., Skandan, G., Hahn, H., Danforth, S., & Kear, B. (1994). Chemical vapor condensation of nanostructured ceramic powders. *Nanostructured Materials, 4*(3), 345-351.

Chen, C.-M., Zhang, Q., Yang, M.-G., Huang, C.-H., Yang, Y.-G., & Wang, M.-Z. (2012). Structural evolution during annealing of thermally reduced graphene nanosheets for application in supercapacitors. *Carbon, 50*(10), 3572-3584.

Choi, W., Lahiri, I., Seelaboyina, R., & Kang, Y. S. (2010). Synthesis of graphene and its applications: A review. *Critical Reviews in Solid State and Materials Sciences, 35*(1), 52-71.

Chong, M. Y., Numan, A., Liew, C. W., Ramesh, K., & Ramesh, S. (2017). Comparison of the performance of copper oxide and yttrium oxide nanoparticle based hydroxylethyl cellulose electrolytes for supercapacitors. *Journal of Applied Polymer Science, 134*(13), 44636.

Ciesla, U., & Schüth, F. (1999). Ordered mesoporous materials. *Microporous and Mesoporous Materials, 27*(2), 131-149.

Clark, L. C., & Lyons, C. (1962). Electrode systems for continuous monitoring in cardiovascular surgery. *Annals of the New York Academy of Sciences, 102*(1), 29-45.

Colindres, S. C., Aguir, K., Cervantes Sodi, F., Vargas, L. V., Salazar, J. A. M., & Febles, V. G. (2014). Ozone sensing based on palladium decorated carbon nanotubes. *Sensors, 14*(4), 6806-6818.

Conway, B. (1999). The electrolyte factor in supercapacitor design and performance: Conductivity, ion pairing and solvation *Electrochemical supercapacitors* (pp. 335-375): Springer.

Dai, C.-S., Chien, P.-Y., Lin, J.-Y., Chou, S.-W., Wu, W.-K., Li, P.-H., Wu, K.-Y., & Lin, T.-W. (2013). Hierarchically structured ni_3s_2/carbon nanotube composites as high performance cathode materials for asymmetric supercapacitors. *ACS Applied Materials & Interfaces, 5*(22), 12168-12174.

Datsyuk, V., Kalyva, M., Papagelis, K., Parthenios, J., Tasis, D., Siokou, A., Kallitsis, I., & Galiotis, C. (2008). Chemical oxidation of multiwalled carbon nanotubes. *Carbon, 46*(6), 833-840.

Deftereos, N. T., Calokerinos, A. C., & Efstathiou, C. E. (1993). Flow injection chemiluminometric determination of epinephrine, norepinephrine, dopamine and l-dopa. *Analyst, 118*(6), 627-632.

Dillon, E. C., Wilton, J. H., Barlow, J. C., & Watson, W. A. (1989). Large surface area activated charcoal and the inhibition of aspirin absorption. *Annals of Emergency Medicine, 18*(5), 547-552.

Dresselhaus, M., Dresselhaus, G., Jorio, A., Souza Filho, A., & Saito, R. (2002). Raman spectroscopy on isolated single wall carbon nanotubes. *Carbon, 40*(12), 2043-2061.

Du, J., Yue, R., Ren, F., Yao, Z., Jiang, F., Yang, P., & Du, Y. (2013). Simultaneous determination of uric acid and dopamine using a carbon fiber electrode modified by layer-by-layer assembly of graphene and gold nanoparticles. *Gold Bulletin, 46*(3), 137-144.

Duraisamy, N., Numan, A., Fatin, S. O., Ramesh, K., & Ramesh, S. (2016). Facile sonochemical synthesis of nanostructured nio with different particle sizes and its electrochemical properties for supercapacitor application. *Journal of Colloid and Interface Science, 471*, 136-144.

Duraisamy, N., Numan, A., Ramesh, K., Choi, K.-H., & Ramesh, S. (2015). Investigation on structural and electrochemical properties of binder free nanostructured nickel oxide thin film. *Materials Letters, 161*, 694-697.

El-Kady, M. F., Shao, Y., & Kaner, R. B. (2016). Graphene for batteries, supercapacitors and beyond. *Nature Reviews Materials, 1*, 16033.

Ensafi, A. A., Taei, M., & Khayamian, T. (2009). A differential pulse voltammetric method for simultaneous determination of ascorbic acid, dopamine, and uric acid using poly (3-(5-chloro-2-hydroxyphenylazo)-4, 5-dihydroxynaphthalene-2, 7-disulfonic acid) film modified glassy carbon electrode. *Journal of Electroanalytical Chemistry, 633*(1), 212-220.

Fernandes, D. M., Costa, M., Pereira, C., Bachiller-Baeza, B., Rodríguez-Ramos, I., Guerrero-Ruiz, A., & Freire, C. (2014). Novel electrochemical sensor based on n-doped carbon nanotubes and fe_3o_4 nanoparticles: Simultaneous voltammetric determination of ascorbic acid, dopamine and uric acid. *Journal of Colloid and Interface Science, 432*, 207-213.

Fernández-García, M., & Rodriguez, J. A. (2011). Metal oxide nanoparticles. *Encyclopedia of Inorganic and Bioinorganic Chemistry*.

Fiipponi, L., & Sutherland, D. (2012). *Nanotechnologies: Principles, applications, implications and hands-on activities: A compendium for educators*: European Union, Directorate General for Research and Innovation.

Grahame, D. C. (1947). The electrical double layer and the theory of electrocapillarity. *Chemical Reviews, 41*(3), 441-501.

Guan, D., Gao, Z., Yang, W., Wang, J., Yuan, Y., Wang, B., Zhang, M., & Liu, L. (2013). Hydrothermal synthesis of carbon nanotube/cubic fe_3o_4 nanocomposite for enhanced performance supercapacitor electrode material. *Materials Science and Engineering: B, 178*(10), 736-743.

Guo, T., Nikolaev, P., Rinzler, A. G., Tomanek, D., Colbert, D. T., & Smalley, R. E. (1995). Self-assembly of tubular fullerenes. *The Journal of Physical Chemistry, 99*(27), 10694-10697.

Halper, M. S., & Ellenbogen, J. C. (2006). Supercapacitors: A brief overview. *The MITRE Corporation, McLean, Virginia, USA*, 1-34.

Han, M., Gong, Y., Zhou, J., Yin, C., Song, F., Muto, N., Takiya, T., & Iwata, Y. (2002). Plume dynamics during film and nanoparticles deposition by pulsed laser ablation. *Physics Letters A, 302*(4), 182-189.

Hasobe, T. (2010). Supramolecular nanoarchitectures for light energy conversion. *Physical Chemistry Chemical Physics, 12*(1), 44-57.

Henrich, V., & Cox, P. (1994). The surface chemistry of metal oxides: Cambridge University Press, Cambridge, UK.

Holdiness, M. R., Rosen, M. T., Justice, J. B., & Neill, D. B. (1980). Gas chromatographic-mass spectrometric determination of dopamine in subregions of rat brain. *Journal of Chromatography A, 198*(3), 329-336.

Hou, J., Xu, C., Zhao, D., & Zhou, J. (2016). Facile fabrication of hierarchical nanoporous auag alloy and its highly sensitive detection towards dopamine and uric acid. *Sensors and Actuators B: Chemical, 225*, 241-248.

How, G. T. S., Pandikumar, A., Ming, H. N., & Ngee, L. H. (2014). Highly exposed {001} facets of titanium dioxide modified with reduced graphene oxide for dopamine sensing. *Scientific Reports, 4*, 5044.

Huang, H., Zhu, W., Tao, X., Xia, Y., Yu, Z., Fang, J., Gan, Y., & Zhang, W. (2012). Nanocrystal-constructed mesoporous single-crystalline co_3o_4 nanobelts with superior rate capability for advanced lithium-ion batteries. *ACS applied materials & interfaces, 4*(11), 5974-5980.

Huang, N., Lim, H., Chia, C. H., Yarmo, M. A., & Muhamad, M. (2011). Simple room-temperature preparation of high-yield large-area graphene oxide. *International Journal of Nanomedicine, 6*, 3443-3448.

Hummers Jr, W. S., & Offeman, R. E. (1958). Preparation of graphitic oxide. *Journal of the American Chemical Society, 80*(6), 1339-1339.

Iijima, S. (1980). Direct observation of the tetrahedral bonding in graphitized carbon black by high resolution electron microscopy. *Journal of Crystal Growth, 50*(3), 675-683.

Inami, N., Mohamed, M. A., Shikoh, E., & Fujiwara, A. (2007). Synthesis-condition dependence of carbon nanotube growth by alcohol catalytic chemical vapor deposition method. *Science and Technology of Advanced Materials, 8*(4), 292-295.

Interrante, L. V., & Hampden-Smith, M. J. (1997). Chemistry of advanced materials: An overview. *Chemistry of Advanced Materials: An Overview, by Leonard V. Interrante (Editor), Mark J. Hampden-Smith (Editor), pp. 592. ISBN 0-471-18590-6. Wiley-VCH, December 1997.*, 592.

Irfan, M., Basri, H., Irfan, M., & Lau, W.-J. (2015). An acid functionalized mwcnt/pvp nanocomposite as a new additive for fabrication of an ultrafiltration membrane with improved anti-fouling resistance. *RSC Advances, 5*(116), 95421-95432.

Jackowska, K., & Krysinski, P. (2013). New trends in the electrochemical sensing of dopamine. *Analytical and Bioanalytical Chemistry, 405*(11), 3753-3771.

Jacobs, C. B., Peairs, M. J., & Venton, B. J. (2010). Review: Carbon nanotube based electrochemical sensors for biomolecules. *Analytica Chimica Acta, 662*(2), 105-127.

Jafarian, M., Mahjani, M., Heli, H., Gobal, F., Khajehsharifi, H., & Hamedi, M. (2003). A study of the electro-catalytic oxidation of methanol on a cobalt hydroxide modified glassy carbon electrode. *Electrochimica Acta, 48*(23), 3423-3429.

Janata, J. (2010). *Principles of chemical sensors*: Springer Science & Business Media.

Jayabal, S., & Ramaraj, R. (2013). Synthesis of core/shell au/ag nanorods embedded in functionalized silicate sol–gel matrix and their applications in electrochemical sensors. *Electrochimica Acta, 88*, 51-58.

Kannan, P. K., Moshkalev, S. A., & Rout, C. S. (2016). Highly sensitive and selective electrochemical dopamine sensing properties of multilayer graphene nanobelts. *Nanotechnology, 27*(7), 075504.

Kaya, M., & Volkan, M. r. (2012). New approach for the surface enhanced resonance raman scattering (serrs) detection of dopamine at picomolar (pm) levels in the presence of ascorbic acid. *Analytical Chemistry, 84*(18), 7729-7735.

Kim, H., Seo, D.-H., Kim, S.-W., Kim, J., & Kang, K. (2011). Highly reversible co_3o_4/graphene hybrid anode for lithium rechargeable batteries. *Carbon, 49*(1), 326-332.

Kim, Y.-R., Bong, S., Kang, Y.-J., Yang, Y., Mahajan, R. K., Kim, J. S., & Kim, H. (2010). Electrochemical detection of dopamine in the presence of ascorbic acid using graphene modified electrodes. *Biosensors and Bioelectronics, 25*(10), 2366-2369.

Kim, Y., Noh, Y., Lim, E. J., Lee, S., Choi, S. M., & Kim, W. B. (2014). Star-shaped pd@ pt core–shell catalysts supported on reduced graphene oxide with superior electrocatalytic performance. *Journal of Materials Chemistry A, 2*(19), 6976-6986.

Koch, C. (2003). Top-down synthesis of nanostructured materials: Mechanical and thermal processing methods. *Reviews on Advanced Materials Science, 5*(2), 91-99.

Kouhnavard, M., Ludin, N. A., Ghaffari, B. V., Sopian, K., & Ikeda, S. (2015). Carbonaceous materials and their advances as a counter electrode in dye-sensitized solar cells: Challenges and prospects. *ChemSusChem, 8*(9), 1510-1533.

Koumoto, K., & Yanagida, H. (1981). Electrical conduction in pure and li-substituted co_3o_4. *Journal of the American Ceramic Society, 64*(11), 156–157.

Kumar, R., Kim, H.-J., Park, S., Srivastava, A., & Oh, I.-K. (2014). Graphene-wrapped and cobalt oxide-intercalated hybrid for extremely durable super-capacitor with ultrahigh energy and power densities. *Carbon, 79*, 192-202.

Kuperman, A., & Aharon, I. (2011). Battery–ultracapacitor hybrids for pulsed current loads: A review. *Renewable and Sustainable Energy Reviews, 15*(2), 981-992.

Lee, C. C., Omar, F. S., Numan, A., Duraisamy, N., Ramesh, K., & Ramesh, S. (2017). An enhanced performance of hybrid supercapacitor based on polyaniline-manganese phosphate binary composite. *Journal of Solid State Electrochemistry*, 1-9.

Lencka, M. M., Oledzka, M., & Riman, R. E. (2000). Hydrothermal synthesis of sodium and potassium bismuth titanates. *Chemistry of Materials, 12*(5), 1323-1330.

Li, B., Xie, Y., Wu, C., Li, Z., & Zhang, J. (2006). Selective synthesis of cobalt hydroxide carbonate 3d architectures and their thermal conversion to cobalt spinel 3d superstructures. *Materials Chemistry and Physics, 99*(2), 479-486.

Li, J., Zeng, X., Ren, T., & van der Heide, E. (2014). The preparation of graphene oxide and its derivatives and their application in bio-tribological systems. *Lubricants, 2*(3), 137-161.

Li, J., Zhao, W., Huang, F., Manivannan, A., & Wu, N. (2011). Single-crystalline $ni(oh)_2$ and nio nanoplatelet arrays as supercapacitor electrodes. *Nanoscale, 3*(12), 5103-5109.

Li, S.-S., Zheng, J.-N., Ma, X., Hu, Y.-Y., Wang, A.-J., Chen, J.-R., & Feng, J.-J. (2014). Facile synthesis of hierarchical dendritic ptpd nanogarlands supported on reduced graphene oxide with enhanced electrocatalytic properties. *Nanoscale, 6*(11), 5708-5713.

Li, Z., Zhou, Z., Yun, G., Shi, K., Lv, X., & Yang, B. (2013). High-performance solid-state supercapacitors based on graphene-zno hybrid nanocomposites. *Nanoscale research letters, 8*(1), 473.

Liang, Y., Li, Y., Wang, H., Zhou, J., Wang, J., Regier, T., & Dai, H. (2011). Co_3o_4 nanocrystals on graphene as a synergistic catalyst for oxygen reduction reaction. *Nature materials, 10*(10), 780-786.

Lim, S. Y., Shen, W., & Gao, Z. (2015). Carbon quantum dots and their applications. *Chemical Society Reviews, 44*(1), 362-381.

Liu, Y., She, P., Gong, J., Wu, W., Xu, S., Li, J., Zhao, K., & Deng, A. (2015). A novel sensor based on electrodeposited au–pt bimetallic nano-clusters decorated on graphene oxide (go)–electrochemically reduced go for sensitive detection of dopamine and uric acid. *Sensors and Actuators B: Chemical, 221*, 1542-1553.

Livage, J., Henry, M., & Sanchez, C. (1988). Sol-gel chemistry of transition metal oxides. *Progress in Solid State Chemistry, 18*(4), 259-341.

Lue, J. T. (2007). Physical properties of nanomaterials. *Encyclopedia of nanoscience and nanotechnology, 10*(1).

Malik, M. A., Wani, M. Y., & Hashim, M. A. (2012). Microemulsion method: A novel route to synthesize organic and inorganic nanomaterials: 1st nano update. *Arabian journal of Chemistry, 5*(4), 397-417.

Mamiński, M., Olejniczak, M., Chudy, M., Dybko, A., & Brzózka, Z. (2005). Spectrophotometric determination of dopamine in microliter scale using microfluidic system based on polymeric technology. *Analytica Chimica Acta, 540*(1), 153-157.

Mani, V., Devasenathipathy, R., Chen, S.-M., Kohilarani, K., & Ramachandran, R. (2015). A sensitive amperometric sensor for the determination of dopamine at graphene and bismuth nanocomposite film modified electrode. *International Journal of Electrochemical Science, 10*, 1199-1207.

Mele, T., Čarman-Kržan, M., & Jurič, D. M. (2010). Regulatory role of monoamine neurotransmitters in astrocytic nt-3 synthesis. *International Journal of Developmental Neuroscience, 28*(1), 13-19.

Meregalli, V., & Parrinello, M. (2001). Review of theoretical calculations of hydrogen storage in carbon-based materials. *Applied Physics A, 72*(2), 143-146.

Moghim, M. H., & Zebarjad, S. M. (2015). Fabrication and structural characterization of multi-walled carbon nanotube/fe$_3$o$_4$ nanocomposite. *Journal of Inorganic and Organometallic Polymers and Materials, 25*(5), 1260-1266.

Moro, F., Tang, S. V. Y., Tuna, F., & Lester, E. (2013). Magnetic properties of cobalt oxide nanoparticles synthesised by a continuous hydrothermal method. *Journal of Magnetism and Magnetic Materials, 348*, 1-7.

Mu, J., Zhang, L., Zhao, M., & Wang, Y. (2013). Co$_3$o$_4$ nanoparticles as an efficient catalase mimic: Properties, mechanism and its electrocatalytic sensing application for hydrogen peroxide. *Journal of Molecular Catalysis A: Chemical, 378*, 30-37.

Naumenko, D., Snitka, V., Snopok, B., Arpiainen, S., & Lipsanen, H. (2012). Graphene-enhanced raman imaging of tio$_2$ nanoparticles. *Nanotechnology, 23*(46), 465703.

Nazemi, Z., Shams, E., & Amini, M. K. (2010). Covalent modification of glassy carbon electrode by nile blue: Preparation, electrochemistry and electrocatalysis. *Electrochimica Acta, 55*(24), 7246-7253.

Noguera, C. (1996). *Physics and chemistry at oxide surfaces*: Cambridge University Press.

Numan, A., Duraisamy, N., Omar, F. S., Mahipal, Y., Ramesh, K., & Ramesh, S. (2016). Enhanced electrochemical performance of cobalt oxide nanocube intercalated reduced graphene oxide for supercapacitor application. *RSC Advances, 6*(41), 34894-34902.

Numan, A., Shahid, M. M., Omar, F. S., Rafique, S., Bashir, S., Ramesh, K., & Ramesh, S. (2017). Binary nanocomposite based on co_3o_4 nanocubes and multiwalled carbon nanotubes as an ultrasensitive platform for amperometric determination of dopamine. *Microchimica Acta*, 1-10.

Numan, A., Shahid, M. M., Omar, F. S., Ramesh, K., & Ramesh, S. (2017). Facile fabrication of cobalt oxide nanograin-decorated reduced graphene oxide composite as ultrasensitive platform for dopamine detection. *Sensors and Actuators B: Chemical, 238*, 1043-1051. doi: 10.1016/j.snb.2016.07.111

Nurzulaikha, R., Lim, H., Harrison, I., Lim, S., Pandikumar, A., Huang, N., Lim, S., Thien, G., Yusoff, N., & Ibrahim, I. (2015). Graphene/sno_2 nanocomposite-modified electrode for electrochemical detection of dopamine. *Sensing and Bio-Sensing Research, 5*, 42-49.

O'connell, M. J. (2006). *Carbon nanotubes: Properties and applications*: CRC press.

Obata, T. (2002). Dopamine efflux by mptp and hydroxyl radical generation. *Journal of Neural Transmission, 109*(9), 1159-1180.

Omar, F. S., Numan, A., Duraisamy, N., Bashir, S., Ramesh, K., & Ramesh, S. (2017). A promising binary nanocomposite of zinc cobaltite intercalated with polyaniline for supercapacitor and hydrazine sensor. *Journal of Alloys and Compounds, 716*, 96-105.

Omar, F. S., Numan, A., Duraisamy, N., Ramly, M. M., Ramesh, K., & Ramesh, S. (2017). Binary composite of polyaniline/copper cobaltite for high performance asymmetric supercapacitor application. *Electrochimica Acta, 227*, 41-48.

Palanisamy, S., Ku, S., & Chen, S.-M. (2013). Dopamine sensor based on a glassy carbon electrode modified with a reduced graphene oxide and palladium nanoparticles composite. *Microchimica Acta, 180*(11-12), 1037-1042.

Palanisamy, S., Sakthinathan, S., Chen, S.-M., Thirumalraj, B., Wu, T.-H., Lou, B.-S., & Liu, X. (2016). Preparation of β-cyclodextrin entrapped graphite composite for sensitive detection of dopamine. *Carbohydrate Polymers, 135*, 267-273.

Pandikumar, A., How, G. T. S., See, T. P., Omar, F. S., Jayabal, S., Kamali, K. Z., Yusoff, N., Jamil, A., Ramaraj, R., & John, S. A. (2014). Graphene and its nanocomposite material based electrochemical sensor platform for dopamine. *RSC Advances, 4*(108), 63296-63323.

Panwar, V., Al-Nafiey, A., Addad, A., Sieber, B., Roussel, P., Boukherroub, R., & Jain, S. L. (2015). Magnetic co_3o_4/reduced graphene oxide nanocomposite as a superior heterogeneous catalyst for one-pot oxidative esterification of aldehydes to methyl esters. *RSC Advances, 5*(108), 88567-88573.

Park, S., An, J., Jung, I., Piner, R. D., An, S. J., Li, X., Velamakanni, A., & Ruoff, R. S. (2009). Colloidal suspensions of highly reduced graphene oxide in a wide variety of organic solvents. *Nano Letters, 9*(4), 1593-1597.

Paul, P. (2009). Value added products from gasification activated carbon. *Combustion Gasification and Propulsion Laboratory Department of Aerospace Engineering Indian Institute of Science, Bangalore*.

Pendashteh, A., Mousavi, M. F., & Rahmanifar, M. S. (2013). Fabrication of anchored copper oxide nanoparticles on graphene oxide nanosheets via an electrostatic coprecipitation and its application as supercapacitor. *Electrochimica Acta, 88*, 347-357.

Rajput, N. (2015). Methods of preparation of nanoparticles-a review. *International Journal Of Advances In Engineering & Technology, 7*(6), 1806.

Ramadoss, A., & Kim, S. J. (2013). Vertically aligned tio_2 nanorod arrays for electrochemical supercapacitor. *Journal of Alloys and Compounds, 561*, 262-267.

Ramakrishnan, S., Pradeep, K., Raghul, A., Senthilkumar, R., Rangarajan, M., & Kothurkar, N. K. (2015). One-step synthesis of pt-decorated graphene–carbon nanotubes for the electrochemical sensing of dopamine, uric acid and ascorbic acid. *Analytical Methods, 7*(2), 779-786.

Raymundo-Pinero, E., Kierzek, K., Machnikowski, J., & Béguin, F. (2006). Relationship between the nanoporous texture of activated carbons and their capacitance properties in different electrolytes. *Carbon, 44*(12), 2498-2507.

Rodriguez, J. A., & Fernández-García, M. (2007). *Synthesis, properties, and applications of oxide nanomaterials*: John Wiley & Sons.

Roy-Mayhew, J. D., & Aksay, I. A. (2014). Graphene materials and their use in dye-sensitized solar cells. *Chemical Reviews, 114*(12), 6323-6348.

Sadegh, H., & Shahryari-ghoshekandi, R. (2015). Functionalization of carbon nanotubes and its application in nanomedicine: A review. *Nanomedicine Journal, 2*(4), 231-248.

Sahu, V., Goel, S., Sharma, R. K., & Singh, G. (2015). Zinc oxide nanoring embedded lacey graphene nanoribbons in symmetric/asymmetric electrochemical capacitive energy storage. *Nanoscale, 7*(48), 20642-20651.

Salunkhe, R. R., Jang, K., Yu, H., Yu, S., Ganesh, T., Han, S.-H., & Ahn, H. (2011). Chemical synthesis and electrochemical analysis of nickel cobaltite nanostructures for supercapacitor applications. *Journal of Alloys and Compounds, 509*(23), 6677-6682.

Sanders, I. J., & Peeten, T. L. (2011). *Carbon black: Production, properties, and uses*: Nova Science Publishers.

Sankapal, B. R., Gajare, H. B., Karade, S. S., & Dubal, D. P. (2015). Anchoring cobalt oxide nanoparticles on to the surface multiwalled carbon nanotubes for improved supercapacitive performances. *RSC Advances, 5*(60), 48426-48432.

Savvatimskiy, A. (2005). Measurements of the melting point of graphite and the properties of liquid carbon (a review for 1963–2003). *Carbon, 43*(6), 1115-1142.

Scott, B. J., Wirnsberger, G., & Stucky, G. D. (2001). Mesoporous and mesostructured materials for optical applications. *Chemistry of Materials, 13*(10), 3140-3150.

Shah, H. U., Wang, F., Toufiq, A. M., Khattak, A. M., Iqbal, A., Ghazi, Z. A., Ali, S., Li, X., & Wang, Z. (2016). Electrochemical properties of single-crystalline mn$_3$o$_4$ nanostructures and their capacitive performance in basic electrolyte. *International Journal of Electrochemical Science, 11*, 8155-8162.

Shahid, M. M., Pandikumar, A., Golsheikh, A. M., Huang, N. M., & Lim, H. N. (2014). Enhanced electrocatalytic performance of cobalt oxide nanocubes incorporating reduced graphene oxide as a modified platinum electrode for methanol oxidation. *RSC Advances, 4*(107), 62793-62801.

Shahid, M. M., Rameshkumar, P., & Huang, N. M. (2015). Morphology dependent electrocatalytic properties of hydrothermally synthesized cobalt oxide nanostructures. *Ceramics International, 41*(10), 13210-13217.

Shahid, M. M., Rameshkumar, P., Pandikumar, A., Lim, H. N., Ng, Y. H., & Huang, N. M. (2015). An electrochemical sensing platform based on a reduced graphene oxide–cobalt oxide nanocube@ platinum nanocomposite for nitric oxide detection. *Journal of Materials Chemistry A, 3*(27), 14458-14468.

Shan, H., Zhao, Y., Li, X., Xiong, D., Dong, L., Yan, B., Li, D., & Sun, X. (2016). Carbon nanotubes cross-linked zn$_2$. *Journal of Applied Electrochemistry, 46*(8), 851-860.

Shao, Y., Yin, G., Zhang, J., & Gao, Y. (2006). Comparative investigation of the resistance to electrochemical oxidation of carbon black and carbon nanotubes in aqueous sulfuric acid solution. *Electrochimica Acta, 51*(26), 5853-5857.

Sherman, A. (1987). Chemical vapor deposition for microelectronics: Principles, technology, and applications.

Smiljanic, O., Stansfield, B., Dodelet, J.-P., Serventi, A., & Désilets, S. (2002). Gas-phase synthesis of swnt by an atmospheric pressure plasma jet. *Chemical Physics Letters, 356*(3), 189-193.

Smith, T. (1983). A review of carbon black pigments. *Pigment & Resin Technology, 12*(4), 14-16.

Su, D., Dou, S., & Wang, G. (2014). Single crystalline co_3o_4 nanocrystals exposed with different crystal planes for li-o_2 batteries. *Scientific Reports, 4*, 5767.

Subramanian, V., Zhu, H., Vajtai, R., Ajayan, P., & Wei, B. (2005). Hydrothermal synthesis and pseudocapacitance properties of mno_2 nanostructures. *The Journal of Physical Chemistry B, 109*(43), 20207-20214.

Suresh, R., Giribabu, K., Manigandan, R., Kumar, S. P., Munusamy, S., Muthamizh, S., & Narayanan, V. (2014). Characterization and dopamine sensing property of v_2o_5@ polyailine nanohybrid. *Synthetic Metals, 196*, 151-157.

Suryanarayana, C. (2001). Mechanical alloying and milling. *Progress in Materials Science, 46*(1), 1-184.

Tan, Y., Gao, Q., Li, Z., Tian, W., Qian, W., Yang, C., & Zhang, H. (2016). Unique 1d co_3o_4 crystallized nanofibers with (220) oriented facets as high-performance lithium ion battery anode material. *Scientific Reports, 6*, 26460.

Tan, Y., Gao, Q., Yang, C., Yang, K., Tian, W., & Zhu, L. (2015). One-dimensional porous nanofibers of co_3o_4 on the carbon matrix from human hair with superior lithium ion storage performance. *Scientific Reports, 5*, 12382.

Thévenot, D. R., Toth, K., Durst, R. A., & Wilson, G. S. (2001). Electrochemical biosensors: Recommended definitions and classification. *Biosensors and Bioelectronics, 16*(1), 121-131.

Usković, V., & Drofenik, M. (2005). Synthesis of materials within reverse micelles. *Surface Review and Letters, 12*(02), 239-277.

Walker Jr, P., Rakszawski, J., & Imperial, G. (1959). Carbon formation from carbon monoxide-hydrogen mixtures over iron catalysts. I. Properties of carbon formed. *The Journal of Physical Chemistry, 63*(2), 133-140.

Wang, H.-W., Hu, Z.-A., Chang, Y.-Q., Chen, Y.-L., Zhang, Z.-Y., Yang, Y.-Y., & Wu, H.-Y. (2011). Preparation of reduced graphene oxide/cobalt oxide composites and their enhanced capacitive behaviors by homogeneous incorporation of reduced graphene oxide sheets in cobalt oxide matrix. *Materials Chemistry and Physics, 130*(1), 672-679.

Wang, H., Casalongue, H. S., Liang, Y., & Dai, H. (2010). Ni $(oh)_2$ nanoplates grown on graphene as advanced electrochemical pseudocapacitor materials. *Journal of the American Chemical Society, 132*(21), 7472-7477.

Wang, H., Robinson, J. T., Diankov, G., & Dai, H. (2010). Nanocrystal growth on graphene with various degrees of oxidation. *Journal of the American Chemical Society, 132*(10), 3270-3271.

Wang, Q., Han, X., Sommers, A., Park, Y., T'Joen, C., & Jacobi, A. (2012). A review on application of carbonaceous materials and carbon matrix composites for heat exchangers and heat sinks. *International Journal of Refrigeration, 35*(1), 7-26.

Wang, X., Li, Q., Xie, J., Jin, Z., Wang, J., Li, Y., Jiang, K., & Fan, S. (2009). Fabrication of ultralong and electrically uniform single-walled carbon nanotubes on clean substrates. *Nano Letters, 9*(9), 3137-3141.

Wang, X., Liu, W. S., Lu, X., & Lee, P. S. (2012). Dodecyl sulfate-induced fast faradic process in nickel cobalt oxide–reduced graphite oxide composite material and its application for asymmetric supercapacitor device. *Journal of Materials Chemistry, 22*(43), 23114-23119.

Wang, Y.-g., & Xia, Y.-y. (2006). Electrochemical capacitance characterization of nio with ordered mesoporous structure synthesized by template sba-15. *Electrochimica Acta, 51*(16), 3223-3227.

Wang, Y., Xu, H., Zhang, J., & Li, G. (2008). Electrochemical sensors for clinic analysis. *Sensors, 8*(4), 2043-2081.

Watson, C. J., Venton, B. J., & Kennedy, R. T. (2006). In vivo measurements of neurotransmitters by microdialysis sampling: ACS Publications.

Wissler, M. (2006). Graphite and carbon powders for electrochemical applications. *Journal of Power Sources, 156*(2), 142-150.

Wu, Z.-S., Ren, W., Wen, L., Gao, L., Zhao, J., Chen, Z., Zhou, G., Li, F., & Cheng, H.-M. (2010). Graphene anchored with co_3o_4 nanoparticles as anode of lithium ion batteries with enhanced reversible capacity and cyclic performance. *ACS Nano, 4*(6), 3187-3194.

Wu, Z.-S., Sun, Y., Tan, Y.-Z., Yang, S., Feng, X., & Müllen, K. (2012). Three-dimensional graphene-based macro-and mesoporous frameworks for high-performance electrochemical capacitive energy storage. *Journal of the American Chemical Society, 134*(48), 19532-19535.

Xia, J., Chen, F., Li, J., & Tao, N. (2009). Measurement of the quantum capacitance of graphene. *Nature Nanotechnology, 4*(8), 505-509.

Xie, X., Li, Y., Liu, Z.-Q., Haruta, M., & Shen, W. (2009). Low-temperature oxidation of co catalysed by co_3o_4 nanorods. *Nature, 458*(7239), 746-749.

Xiong, S., Chen, J. S., Lou, X. W., & Zeng, H. C. (2012). Mesoporous co_3o_4 and coo@ c topotactically transformed from chrysanthemum-like $co(co_3)$ 0.5 (oh)· 0.11 h_2o and their lithium-storage properties. *Advanced Functional Materials, 22*(4), 861-871.

Xu, C., De, S., Balu, A. M., Ojeda, M., & Luque, R. (2015). Mechanochemical synthesis of advanced nanomaterials for catalytic applications. *Chemical Communications, 51*(31), 6698-6713.

Xu, C., Li, B., Du, H., Kang, F., & Zeng, Y. (2008). Electrochemical properties of nanosized hydrous manganese dioxide synthesized by a self-reacting microemulsion method. *Journal of Power Sources, 180*(1), 664-670.

Xu, J., Gao, L., Cao, J., Wang, W., & Chen, Z. (2010). Preparation and electrochemical capacitance of cobalt oxide (co$_3$o$_4$) nanotubes as supercapacitor material. *Electrochimica Acta, 56*(2), 732-736.

Xu, X., Ray, R., Gu, Y., Ploehn, H. J., Gearheart, L., Raker, K., & Scrivens, W. A. (2004). Electrophoretic analysis and purification of fluorescent single-walled carbon nanotube fragments. *Journal of the American Chemical Society, 126*(40), 12736-12737.

Yang, L., Liu, D., Huang, J., & You, T. (2014). Simultaneous determination of dopamine, ascorbic acid and uric acid at electrochemically reduced graphene oxide modified electrode. *Sensors and Actuators B: Chemical, 193*, 166-172.

Yu, M.-F., Lourie, O., Dyer, M. J., Moloni, K., Kelly, T. F., & Ruoff, R. S. (2000). Strength and breaking mechanism of multiwalled carbon nanotubes under tensile load. *Science, 287*(5453), 637-640.

Zhang, L. L., & Zhao, X. (2009). Carbon-based materials as supercapacitor electrodes. *Chemical Society Reviews, 38*(9), 2520-2531.

Zhao, Y., Chen, Z., Xiong, D.-B., Qiao, Y., Tang, Y., & Gao, F. (2016). Hybridized phosphate with ultrathin nanoslices and single crystal microplatelets for high performance supercapacitors. *Scientific Reports, 6*, 17613.

Zheng, Y., Huang, Z., Zhao, C., Weng, S., Zheng, W., & Lin, X. (2013). A gold electrode with a flower-like gold nanostructure for simultaneous determination of dopamine and ascorbic acid. *Microchimica Acta, 180*(7-8), 537-544.

Zhong, C., Deng, Y., Hu, W., Qiao, J., Zhang, L., & Zhang, J. (2015). A review of electrolyte materials and compositions for electrochemical supercapacitors. *Chemical Society Reviews, 44*(21), 7484-7539.

Zhou, Y., Yan, H., Xie, Q., Huang, S., Liu, J., Li, Z., Ma, M., & Yao, S. (2013). Simultaneous analysis of dopamine and homovanillic acid by high-performance liquid chromatography with wall-jet/thin-layer electrochemical detection. *Analyst, 138*(23), 7246-7253.

LIST OF PUBLICATIONS

Numan, A., Duraisamy, N., Omar, F. S., Mahipal, Y. K., Ramesh, K., & Ramesh, S. (2016). Enhanced electrochemical performance of cobalt oxide nanocube intercalated reduced graphene oxide for supercapacitor application. *RSC Advances*, *6*, 34894–34902.

Numan, A., Shahid, M. M., Omar, F. S., Rafique, S., Bashir, S., Ramesh, K., & Ramesh, S. (2017). Binary nanocomposite based on Co_3O_4 nanocubes and multiwalled carbon nanotubes as an ultrasensitive platform for amperometric determination of dopamine. *Microchimica Acta*, 1-10.

Numan, A., Shahid, M. M., Omar, F. S., Ramesh, K., & Ramesh, S. (2017). Facile fabrication of cobalt oxide nanograin-decorated reduced graphene oxide composite as ultrasensitive platform for dopamine detection. *Sensors and Actuators B: Chemical*, *238*, 1043-1051.

Other Publications

Nady, A., Latiff, M. H. M. A., Ahmed. A., Numan, A., Ooi, C. H. R., & Harun, S. W., (2017). Nickel oxide nanoparticles as a saturable absorber for an all-fiber passively Q-switched erbium-doped fiber laser. *Laser Physics*, 65105-65110.

Liew, C.-W., Ng, H., Numan, A., & Ramesh, S. (2016). Poly(Acrylic acid)–based hybrid inorganic–organic electrolytes membrane for electrical double layer capacitors application. *Polymers*, *8*, 179.

Omar, F. S., Numan, A., Duraisamy, N., Bashir, S., Ramesh, K., Ramesh, S. (2017). A promising binary nanocomposite of zinc cobaltite intercalated with polyaniline for supercapacitor and hydrazine sensor. *Journal of Alloys and Compounds*, *716*, 96-105.

Fattah, N., Ng, H., Mahipal, Y., Numan, A., Ramesh, S., & Ramesh, K. (2016). An Approach to solid-state electrical double layer capacitors fabricated with graphene oxide-doped, ionic liquid-based solid copolymer electrolytes. *Materials*, *9*(6), 450.

Lee, C. C., Omar, F. S., Numan, A., Duraisamy, N., Ramesh, K., & Ramesh, S. (2017). An enhanced performance of hybrid supercapacitor based on polyaniline-manganese phosphate binary composite. *Journal of Solid State Electrochemistry*, 1-9.

Chong, M. Y., Numan, A., Liew, C.-W., Ramesh, K., Ramesh, S. (2016). Comparison of the performance of copper oxide and yttrium oxide nanoparticle based hydroxylethyl cellulose electrolytes for supercapacitors. *Journal of Applied Polymer Science, 134*(13), 44636(1-11).

Chong, M. Y., Liew, C.-W., Numan, A., Yugal, K., Ramesh, K., Ng, H. M., Chong, T. V., Ramesh, S. (2016). Effects of ionic liquid on the hydroxylpropylmethyl cellulose (HPMC) solid polymer electrolyte. *Ionics, 22*(12), 2421-2430.

Nadiah, N. S., Mahipal, Y. K., Numan, A., Ramesh, S., Ramesh, K. (2015). Efficiency of supercapacitor using EC/DMC-based liquid electrolytes with methyl methacrylate (MMA) monomer. *Ionics*, *22*(1), 107-114.

Nadiah, N., Omar, F. S., Numan, A., Mahipal, Y., Ramesh, S., & Ramesh, K. (2017). Influence of acrylic acid on ethylene carbonate/dimethyl carbonate based liquid electrolyte and its supercapacitor application. *International Journal of Hydrogen Energy*, *42*(52), 30683-30690.

Nady, A., Ahmed, M., Numan, A., Ramesh, S., Latiff, A., Ooi, C., Harun, S. (2017). Passively Q-switched erbium-doped fibre laser using cobalt oxide nanocubes as a saturable absorber. *Journal of Modern Optics*, 1-6.

Duraisamy, N., N, A., Omar F. S., Ramesh, K., Ramesh, S. (2016). Facile sonochemical synthesis of nanostructured NiO with different particle sizes and its electrochemical properties for supercapacitor application. *Journal of Colloid and Interface Science*, *471*, 136–144.

Duraisamy, N., N, A., Ramesh, K., Choi, K.-H., Ramesh, S. (2015). Investigation on structural and electrochemical properties of binder free nanostructured nickel oxide thin film. *Materials Letters*, *161*, 694-697.

Numan, A., Duraisamy, N., Omar, F. S., Gopi, D., Ramesh, K., & Ramesh, S. (2017). Sonochemical synthesis of nanostructured nickel hydroxide as an electrode material for improved electrochemical energy storage application. *Progress in Natural Science: Materials International*, *27*(4), 416-423.

Omar, F. S., Numan, A., Duraisamy, N., Bashir, S., Ramesh, K., & Ramesh, S. (2016). Ultrahigh capacitance of amorphous nickel phosphate for asymmetric supercapacitor applications. *RSC Advances*, *6*(80), 76298-76306.

Omar, F. S., Numan, A., Duraisamy, N., Ramly, M. M., Ramesh, K., & Ramesh, S. (2017). Binary composite of polyaniline/copper cobaltite for high performance asymmetric supercapacitor application. *Electrochimica Acta*, *227*, 41-48.

Shahid, M. M., Ismail, A. H., AL-Mokaram, A. M. A. A., Vikneswaran, R., Ahmad, S., Hamza, A., & Numan, A. (2017). A single-step synthesis of nitrogen-doped graphene sheets decorated with cobalt hydroxide nanoflakes for the determination of dopamine. *Progress in Natural Science: Materials International*, *27*(5), 582-587.

RSC Advances

PAPER

View Article Online
View Journal | View Issue

CrossMark
click for updates

Cite this: *RSC Adv.*, 2016, **6**, 34894

Enhanced electrochemical performance of cobalt oxide nanocube intercalated reduced graphene oxide for supercapacitor application†

Arshid Numan, Navaneethan Duraisamy,* Fatin Saiha Omar, Y. K. Mahipal, K. Ramesh and S. Ramesh*

We investigated different molar concentrations of cobalt precursor intercalated reduced graphene oxide (rGO) as possible electrode materials for supercapacitors. Cobalt oxide (Co_3O_4) nanocubes intercalated reduced graphene oxides (rGO) were synthesized *via* a facile hydrothermal method. It has been found that the Co_3O_4 particles with a cubical shape are decorated on rGO matrix with an average size of ~45 nm. The structural crystallinity of rGO–Co_3O_4 composites was examined by X-ray diffraction (XRD). Raman spectroscopy confirmed the successful reduction of GO to rGO and effective interaction between Co_3O_4 and the rGO matrix. The electrochemical performances of rGO–Co_3O_4 electrodes were examined using cyclic voltammetry and charge–discharge techniques. The maximum specific capacitance (278 F g^{-1}) is observed at current density of 200 mA g^{-1} in the C2 electrode resulting from effective ion transfer and less particle aggregation of Co_3O_4 on the rGO matrix than in the other electrodes. C2 exhibits good rate capability and excellent long-term cyclic stability of 91.6% for 2000 cycles. The enhanced electrochemical performance may result from uniform intercalation of cobalt oxide over the rGO. These results suggest that the Co_3O_4 intercalated rGO matrix could play a role in improved energy storage capability.

Received 4th January 2016
Accepted 23rd March 2016

DOI: 10.1039/c6ra00160b

www.rsc.org/advances

1. Introduction

The imminent depletion of fossil fuels and undesirable consequences of air pollution are alarming significant environmental concerns. These issues have motivated researchers to develop green, sustainable, and highly efficient alternative energy resources (solar energy, wind energy, *etc.*) and energy storages (batteries, supercapacitors).[1] Among the various types of energy devices, the supercapacitor (SC, also known as an electrochemical capacitor) has emerged as an attractive energy storage device because of its extremely high power density, rapid dynamics of charge propagation, excellent cyclic retention, good energy density, and minimum charge separation compared with conventional capacitors and batteries.[2,3]

Generally, SCs can be classified into three different types according to the charge storage phenomenon: the electric double layer capacitor (EDLC), the pseudocapacitor, and the hybrid supercapacitor. In EDLC, the charges are stored in the electrode and electrolyte interfaces, whereas in the pseudocapacitor, charges are stored electrostatically *via* reversible adsorption of ions from the electrolyte into the electrode surface, resulting in higher specific capacitance than that of EDLC.[4–6] Hybrid supercapacitors consist of asymmetric EDLC and pseudo (battery)-type electrode materials, hybridizing the advantages of EDLC and pseudocapacitors.

Usually, pseudocapacitors employ noble/transition metal oxides or conducting polymers as electrode materials.[7] From the library of possible transition metal oxides, cobalt oxide (Co_3O_4) has emerged as a leader. It has high surface to volume ratio, simple preparation method, outstanding chemical durability, a promising ratio of surface atoms, and diverse morphology.[8] However, the practical applications of such metal oxide-based pseudocapacitors may still be limited because of sluggish electron kinetics and rapid capacity decay arising from highly corrosive electrolyte and easily damaged morphologies of the materials during the faradic reactions.[9]

Many approaches have been explored for obtaining desirable electrode materials with different structures, to obtain high power and energy density.[10–13] Incorporation of transition metal oxides with carbon materials can enhance electrochemical performance because of the enormous surface area and high electrical conductivity. Herein, graphene (as a two-dimensional (2D) monolayer of carbon atoms with hexagonal honeycomb lattice structure) has attracted tremendous attention because of its unique physicochemical properties, especially high surface

---

Centre for Ionics University of Malaya, Department of Physics, Faculty of Science, University of Malaya, Lembah Pantai, 50603 Kuala Lumpur, Malaysia. E-mail: rameshtsubra@gmail.com; naveennanoenergy@gmail.com; Fax: +60-3-7967-4146; Tel: +60-3-7967-4391

† Electronic supplementary information (ESI) available. See DOI: 10.1039/c6ra00160b

Sensors and Actuators B 238 (2017) 1043–1051

Contents lists available at ScienceDirect

Sensors and Actuators B: Chemical

journal homepage: www.elsevier.com/locate/snb

Facile fabrication of cobalt oxide nanograin-decorated reduced graphene oxide composite as ultrasensitive platform for dopamine detection

Arshid Numan, Muhammad Mehmood Shahid, Fatin Saiha Omar, K. Ramesh, S. Ramesh*

Centre for Ionics University of Malaya, Department of Physics, Faculty of Science, University of Malaya, 50603 Kuala Lumpur, Malaysia

ARTICLE INFO

Article history:
Received 28 April 2016
Received in revised form 1 July 2016
Accepted 21 July 2016
Available online 22 July 2016

Keywords:
Cobalt oxide
Nanograins
Dopamine
Electrochemical study
Amperometric detection

ABSTRACT

A sensitive and selective detection of dopamine (DA) by a sensor based on cobalt oxide (Co_3O_4) nanograin-decorated reduced graphene oxide (rGO) composite modified glassy carbon electrode (GCE) is reported. The rGO-Co_3O_4 nanograin composites are synthesized by a facile hydrothermal route and optimized by varying the contents of rGO (5.7, 7.4, 9.1 and 10.7 wt%, denoted as C1, C2, C3 and C4 respectively). The crystallinity of the composite is examined by X-ray diffraction (XRD). Raman spectrum revealed the successful reduction of graphene oxide (GO) into rGO. The surface morphology through field emission scanning electron microscopy (FESEM) revealed that the granular-shaped Co_3O_4 are decorated on rGO matrix with an average particle size of ~35 nm. For electrochemical oxidation of DA, glassy carbon electrode (GCE) is modified with nanocomposites. Cyclic voltammetric results show that C3 modified GCE exhibit enhanced electrocatalytic performance in terms of oxidation potential and peak current in comparison to those of bare GCE, Co_3O_4 nanograins, C1, C2 and C4 modified GCE. The choronoamperometric studies indicate that C3 modified GCE exhibit a low detection limit of (S/N = 3) 0.277 μM in the linear range of 1–30 μM. In addition, C3 demonstrates good selectivity towards the detection of DA in the presence of a 100-fold higher concentration of ascorbic acid, glucose and uric acid as the interfering species. The electrochemical sensing studies suggest that 3D rGO-Co_3O_4 nanograins endow excellent catalytic activity, high selectivity and sensitivity towards DA.

1. Introduction

In recent years, neurotransmitters have received considerable attention owing to their vital role in cardiovascular, renal, hormonal and central nervous system [1]. Among various neurotransmitters, dopamine (DA) belongs to the catecholamine and phenethylamine families, which is a naturally occurring hormone present in the human brain. It influences the motivated behaviors such as attention span, neuroplasticity and regulates cognition as well as emotions in our body. In the nervous system, neurotransmitters are the agents for transition of messages between neurons, hence, a disturbance in dopaminergic neurotransmission leads to neurological disorder which results in parkinson disease [2,3] and schizophrenia [4–8]. Therefore, detection and accurate quantification of DA in biological fluids are the subjects of great importance. Several analytical detection approaches; high performance liquid chromatography (HPLC) [9], fluorometry [10], spectrophotometry [11], chemiluminescence capillary electrophoresis and electrochemical methods [12] have been employed for the sensitive detection of DA. However electrochemical sensing methods have drawn considerable interest due to their prominent advantages such as simplicity, high sensitivity, reproducibility, cost effectiveness and non-destructive quantitative detection [13–15]. Moreover DA is highly electroactive and easily gets oxidised, so electrochemical methods are highly preferred for its quantitative determination [16]. The major challenge in electrochemical detection of DA is the presence of main interfering molecules, such as uric acid (UA) and ascorbic acid (AA) in high concentration in biological tissues [17,18]. Conventional unmodified electrodes are incapable of selectively detecting DA owing to the sluggish electron transfer rate. In addition to this, fouling effect of electrode surface by the formation of oxidation products affects the selectivity and reproducibility of the electrode. To resolve these problems, the surface of electrode is required to be modified with a material having excellent electrocatalytic activity so that it can oxidise DA selectively without interacting with other coexisting

---

* Corresponding author.
E-mail addresses: numan.arshed@yahoo.com (A. Numan), rameshtsubra@gmail.com (S. Ramesh).

http://dx.doi.org/10.1016/j.snb.2016.07.111
0925-4005/© 2016 Elsevier B.V. All rights reserved.

Microchim Acta
DOI 10.1007/s00604-017-2269-1

ORIGINAL PAPER

Binary nanocomposite based on Co_3O_4 nanocubes and multiwalled carbon nanotubes as an ultrasensitive platform for amperometric determination of dopamine

Arshid Numan [1] · **Muhammad Mehmood Shahid** [2] · **Fatin Saiha Omar** [1] ·
Saqib Rafique [2] · **Shahid Bashir** [3] · **K. Ramesh** [1] · **S. Ramesh** [1]

Received: 29 November 2016 / Accepted: 13 April 2017

Abstract Composites containing cobalt oxide (Co_3O_4) nanocubes integrated with multiwall carbon nanotubes (MWCNT) were synthesized by a hydrothermal route. The fractions of MWCNTs in the composite were varied from 4, 8, 12, 16 and 20 wt.%, and the resulting materials are denoted as C1, C2, C3, C4 and C5, respectively. The formation of products with high structural crystallinity was confirmed by X-ray photoelectron spectroscopy, Raman spectroscopy and X-ray diffraction. A morphological study by field emission scanning electron microscopy and high resolution transmission electron microscopy showed the successful integration of Co_3O_4 nanocubes to the MWCNTs with an average particle size of ~32 nm. The surface of a glassy carbon electrode (GCE) was modified with the nanocomposites in order to evaluate the electrochemical performance of the nanocomposites. Cyclic voltammetry showed that the C4-modified GCE displays best performance in terms of oxidation potential and peak current in comparison to that of a bare GCE, Co_3O_4 nanocubes, or GCEs modified with C1, C2, C3 or C5. The detection limit (at an S/N ratio of 3) is 0.176 nM by using chronoamperometry, and the linear range is between 1 and 20 µM.

Keywords Electrochemical sensing · Amperometric detection · XPS · Urine analysis · HRTEM · Neurotransmitter · Electrocatalysis · XRD · FESEM · Raman spectroscopy

Introduction

Dopamine is a key neurotransmitter that is present in the mammalian central nervous system and participates significantly in the activity of the hormonal, renal, cardiovascular and central nervous systems. It is responsible for communication of electrical signals between substantia nigra and various brain tissues. Additionally, it also helps to control hormonal balance and emotions. However, the abnormality in dopaminergic neurotransmission system results in various neurological diseases like schizophrenia, [1], Parkinson's disease [2], human immunodeficiency virus (HIV) infection [3] and Huntington's disease [4]. Consequently, quantitative determination of DA is very important. But various physiological biomolecules coexist with DA in a very high concentration in a biological system. Therefore, quantitative determination with good selectivity of DA is extremely important for the diagnosis and pathological understanding of several neurological diseases. For ex-vivo determination of DA, several techniques have been developed that includes: mass spectrometry [5], flow injection chemiluminescence fluorescence [6], surface enhanced Raman scattering [7], chromatography [8] optical absorption spectrophotometry [9] and micro dialysis [10]. But these analytical techniques suffer from the limitations of expensive instrumentation, large sample volumes, time consuming analysis and use of non-green solvents. On the other hand,

---

Electronic supplementary material The online version of this article (doi:10.1007/s00604-017-2269-1) contains supplementary material, which is available to authorized users.

✉ Arshid Numan
numan.arshed@yahoo.com

✉ S. Ramesh
rameshtsubra@gmail.com

[1] Centre for Ionics University of Malaya, Department of Physics, Faculty of Science, University of Malaya, 50603 Kuala Lumpur, Malaysia

[2] Department of Physics, Faculty of Science, University of Malaya, 50603 Kuala Lumpur, Malaysia

[3] Department of Chemistry, Faculty of Science, University of Malaya, 50603 Kuala Lumpur, Malaysia